

UNIVERSITÀ DEGLI STUDI DI CATANIA

in convenzione con

UNIVERSITÀ DEGLI STUDI DI PALERMO

Dottorato di Ricerca in
Scienza dei Materiali e Nanotecnologie- XXIX ciclo

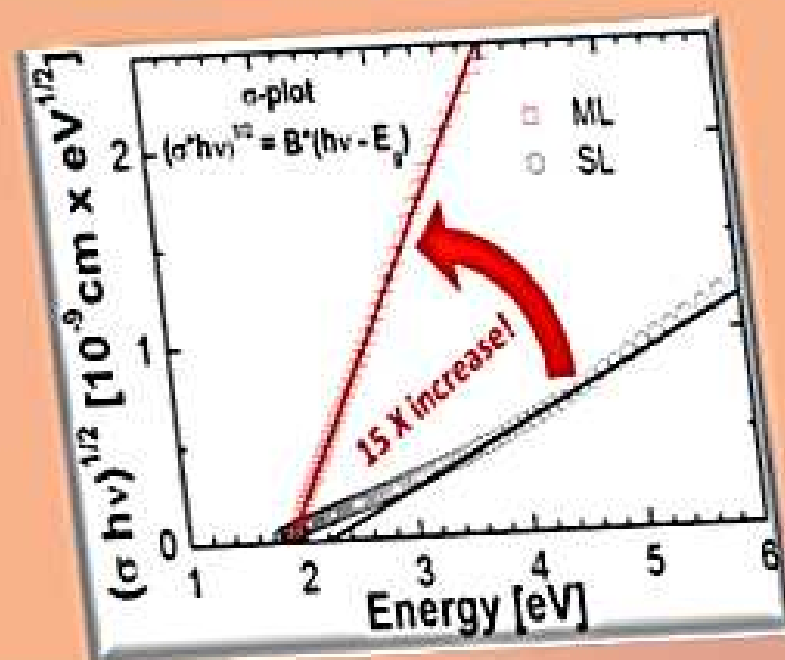
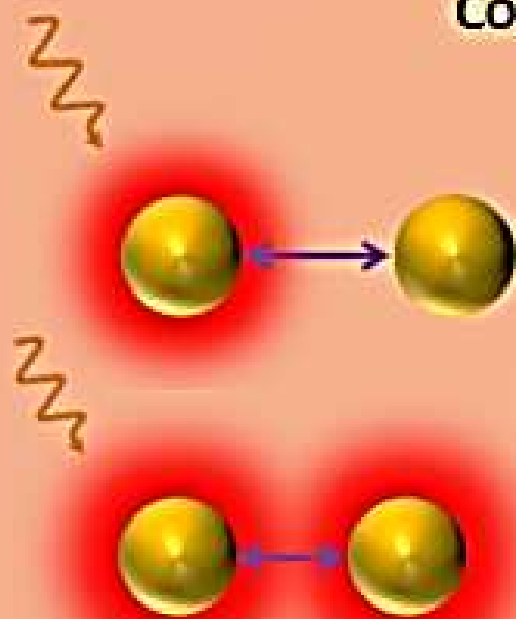
Rosario Raciti

**Quantum confinement effects on
light absorption in Germanium for
solar energy conversion**

TUTOR: Prof. A. Terrasi

CO-TUTOR: Prof. S. Mirabella

COORDINATORE: Prof.ssa M. G. Grimaldi



Tesi per il conseguimento del titolo di Dottore di Ricerca



UNIVERSITÀ DEGLI STUDI DI CATANIA

IN CONVENZIONE CON



UNIVERSITÀ DEGLI STUDI DI PALERMO

DOTTORATO DI RICERCA IN

SCIENZA DEI MATERIALI E NANOTECNOLOGIE - XXIX CICLO

Rosario Raciti

**Quantum confinement effects on light absorption
in Germanium for solar energy conversion**

TUTOR: Prof. A. Terrasi

CO-TUTOR: Prof. S. Mirabella

COORDINATORE: Prof.ssa M. G. Grimaldi

Tesi per il conseguimento del titolo di Dottore di Ricerca

To my Family

COVER

LEFT: Schematic representation of the different strength interaction with light for single layer and multilayers samples. The shorter distance between QDs observed in ML samples is responsible for light absorption enhancement. More details can be found within this thesis in chapter 4.

RIGHT: Tauc plot (symbols) and corresponding linear fits (lines) for Ge QDs arranged in multilayers (ML) and single layer (SL) configurations. The higher slope of linear fit observed in ML samples is related to an enhanced light absorption. More details can be found within this thesis in section 4.3.

Quantum confinement effects on light absorption in Germanium for solar energy conversion

Rosario Raciti

Ph.D. Thesis, University of Catania

Printed in Catania, January 2017

Index

Abstract	I
Chapter 1	1
Quantum structures and light absorption	1
1.1 Sunlight Conversion	1
1.1.1 Energy need and solar potential	1
1.1.2 Light-energy conversion	6
1.1.3 Research perspectives	8
1.2 Quantum confinement effect.....	14
1.3 Light absorption in quantum structures	21
1.3.1 Light Absorption in semiconductors: dielectric function	21
1.3.2 Light Absorption in semiconductors: absorption coefficient.....	24
1.3.3 Light Absorption in semiconductor NS	30
Chapter 2	39
Light absorption in Ge QW: methods for experimental data analysis ..	39
2.1 Ge QW: synthesis and experimental data.....	40
2.2 Methods of E_g extraction: overview	43
2.3 Determination of optical band gap.....	48
2.3.1 JTL approach	48
2.3.2 DPA approach.....	52
2.3.3 SPA approach	55
2.3.4 Models comparison	57
2.4 Conclusions.....	65

Chapter 3.....	67
Light absorption in Ge QDs randomly distributed in SiO₂	67
3.1 Introduction.....	68
3.2 Synthesis and structural properties of Ge QDs	69
3.3 QD/matrix investigation: the role of growth method	75
3.4 Interface effects on light absorption in Ge QDs	82
3.5 Conclusion	90
 Chapter 4.....	 93
Enhancement of light absorption in Ge QDs orderly distributed in SiO₂...	93
4.1 Introduction.....	94
4.2 Synthesis and structural properties of multilayer of Ge QDs	94
4.3 Light absorption in Ge QDs multilayer structure.....	101
4.4 Optical fitting.....	108
4.5 Conclusions.....	113
 Conclusions.....	 115
 Appendix 1.....	 119
 Appendix 2.....	 125
 References.....	 129
 Curriculum vitae.....	 139
 List of Publications	 141
 Acknowledgments	 Errore. Il segnalibro non è definito.

Abstract

The world demand for energy is continuously increasing with a rate that will soon become unsustainable given the current exploitation of energy sources (such as fossil fuels). In addition, it should be figured out that most of commonly used energy resource are limited and that humankind has liberated a quantity of carbon (as CO_2) in the past 250 years that it took our planet about 250 million of years to sequester. In this context, a wide and exciting range of possible solutions to provide enough and cleaner energy is represented by nanotechnologies offering innovative materials with interesting effects exploitable for energy production, distribution and saving. Among other materials, Group-IV semiconductors have been deeply investigated since they allow the fabrication of abundant, non-toxic, mono-elemental nanostructures (as Si quantum dots, C nanotubes, Ge nanowires, et al.) thanks to high purity and mature technology. Moreover, fascinating effects due to quantum confinement in this nanostructures can be effectively exploited for energy production in photovoltaics devices. Among them, Ge reveals interesting optical properties due to its quasi-direct bandgap, higher absorption coefficient and larger exciton Bohr radius with respect to Si, giving the chance to easily tune the optical properties by exploiting quantum confinement effect (QCE). However, the properties of Ge quantum dots (QDs) depends not only on the size as many other parameters can concur in controlling their optical behavior, especially for what concerns the optical bandgap. For this reason, the aim of this thesis is devoted to a detailed investigation of the optical properties of Ge QD, with particular emphasis on the light absorption properties and its modulation by QCE.

This thesis, after a general overview of photovoltaics field, an exhaustive introduction about the interesting optical properties of semiconductor NS and on the methodology to extract them (chapter 1), is divided into the following parts:

- In the second chapter, the main goal will be to establish an effective methodology for the extraction of optical band-gap in semiconductor NS. To do this, we will use the Ge QWs as they join the simplest confining structure (QW) and a semiconductor material (Ge) with large QCE. Ge quantum wells (QWs) have been deposited by plasma enhanced chemical vapor deposition (PECVD). The light absorption of the latter has been characterized by UV-Vis/NIR spectrophotometry which allows us to extract the reflectance (R) and transmittance (T) spectra. In this chapter, we will try to show pro and cons in terms of complexity and accuracy of two approximated methods (double pass approximation (DPA) and single pass approximation (SPA) models) based on R and T spectra (measured by spectrophotometry) to get the absorption coefficient spectra. To do this, we will compare the absorption coefficient extracted through the DPA and SPA models with that extracted through a more accurate method based on generalized transfer matrix method (GTM). Moreover, by comparing the optical band-gaps obtained by Tauc and Cody models (applied to absorption coefficient extracted by DPA and SPA models) with the values extracted through a more accurate parametrization method based on GTM approach (JTL model), we will show which of these two approximated models

(Tauc or Cody models respectively) gives more reliable results on the extraction of optical band-gap in confined systems.

- In the third chapter we present a detailed investigation on the interface of Ge QDs randomly distributed in SiO_2 and their interplay in the confinement effects occurring in the light absorption process. Quantum confinement (QC) typically assumes a sharp interface between a nanostructure and its environment, leading to an abrupt change in the potential for confined electrons and holes. When the interface is not ideally sharp, significant variations from the QC rule appear and other structural parameters beyond the nanostructure size play a considerable role. To experimentally observe such deviations we will investigate the structural and chemical properties of Ge QD interfaces embedded in a SiO_2 and synthesized through thermal annealing of Ge-rich films deposited by plasma enhanced chemical vapor deposition or co-sputtering deposition. We will demonstrate that the different chemical interface observed on sputter and PECVD grown Ge QDs largely influences the size-dependent tuning of the bandgap and oscillator strength. A spatially dependent effective mass (SPDEM) model will be employed to account for the interface difference between Ge QDs, pointing out a larger reduction of exciton effective mass in the sharper interface case. The results of this study provide a new understanding of the role of interfaces on the quantum confinement effects in nanostructures. Moreover, our results indicate a further direction for an optimized exploitation of confinement effects in future nanostructure-based devices: not only

by exploiting size effects, but also taking advantage of interface engineering.

- The fourth chapter is devoted to an experimental investigation of light absorption in small Ge QDs (2-3 nm in diameter) grown by PECVD in a multilayer configuration (3-6 nm thick film with Ge QDs, separated by 20 nm thick SiO₂ barrier). In order to investigate the main features of QCE by controlling the QD diameter, multilayers of Ge QDs embedded in SiO₂, separated by an SiO₂ barrier layers (20 nm thick) were synthesized by plasma enhanced chemical vapor deposition and annealing at 800°C. The multilayer approach allows a narrower size distribution in comparison to single layer of QDs (where no SiO₂ barrier layers are involved). During the discussion, we will compare the light efficiency of Ge QDs in multilayer (ML) and single layer configuration (SL). The optical results will show an unprecedented high light absorption efficiency in ML systems, 15 times larger than in the bulk. These results add new insights into the role of QD packaging on confined systems, and open the route for reliable exploitation of QC effect

Chapter 1

Quantum structures and light absorption

1.1 Sunlight Conversion

1.1.1 Energy need and solar potential

Energy is one of the most important needs in our life. In fact, we need energy for everything, to power houses and cars, to use technology and to feed and clothe us. For this reason, today, is even more evident that energy plays a key role in the economy and development of the human society. In particular, the Country's energy consumption is directly related to both its economic output and the living conditions and number of its citizens. Population growth and the desire to maintain or to raise the current standards of living generate an increasing energy consumption. Nowadays, the World population is about 7 billion, whereas the annual energy consumption has reached a value of 14 TW·year, with an yearly growth rate of about 3% that will led to double this value in the next twenty years, as reported in **figure 1.1** [1], [2], [3].

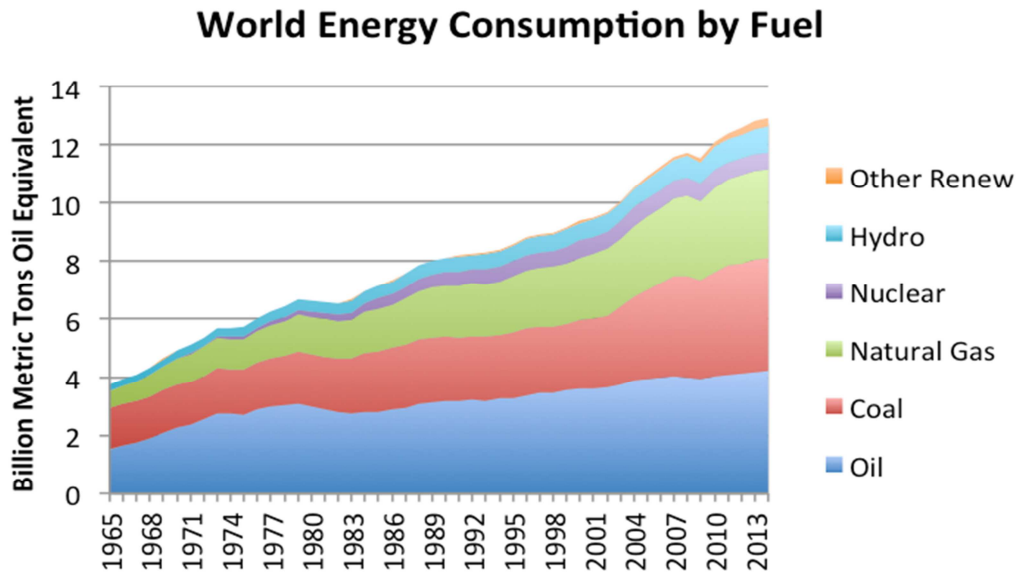


Figure 1.1 Energy consumption by part of the World, based on BP Statistical Review of World Energy 2015. [3].

Several studies also show that the required energy grows much more faster than World population. The explanation of this trend is related to changes that transform the daily lives of many people, such as the increased manufacturing, the labor-saving devices and more recently, computers, cell phone and other power requirements. Currently, fossil fuels such as oil, coal and natural gas provide almost 80% of World energy supply [2], [3], [4]. We know, however, that these traditional sources have been rapidly depleted and so they will not last for a long time. Moreover, the emission of carbon dioxide into the Earth's atmosphere, primarily due to the burning of fossil fuels for energy, are the cause of rising global temperatures. Thus, the future global economy is likely to consume even more energy, especially with the rising energy demand from developing Countries such as China and India.

At the same time, the tremendous risk of climate change associated with the use of fossil fuels makes the supply of this energy increasingly difficult. Last but not the least, oil and gas reserves are in the hands of a small group of Nations, several of which are considered political unstable or have strained diplomatic relationships with large Countries with a high demand of energy. In fact, about 80% of the World's gas and oil reserves are located in just five regions of the Earth: Africa, Russia, Iran, Qatar, and the Persian Gulf, respectively [1], [3]. For all these reasons, the most important scientific and technological challenge of the twenty-first century is to supply secure, clean, and sustainable energy to all citizens of the World in order to ensure an adequate and appropriate quality of the life. In this scenario, the renewable energy sources could be a viable and environmentally friendly solution to the growing global energy demand. Among of all renewable energy sources, the solar is the most clean, efficient and abundant one.

Solar energy, in active and passive form, is the source of nearly all energy on the Earth. Humans, like all other animals and plants, rely on the sun for warmth and food. In **figure 1.2**, we report a comparison between the potential of renewable and conventional planetary energy reserves. While for the former the yearly potential is shown in terawatts (TW), conventional sources, such as oil and coal, display their total recoverable reserves in terawatt-years (TW-yr). The volume of the spheres is proportional to the amount of energy they represent. Global solar power of 23000 TW refers to the Earth's total land mass with atmospheric losses taken into account, and corresponds to 200 million TWh per year [5]. As clearly shown in **figure 1.2**, the solar resource is several order magnitude larger than the others combined.

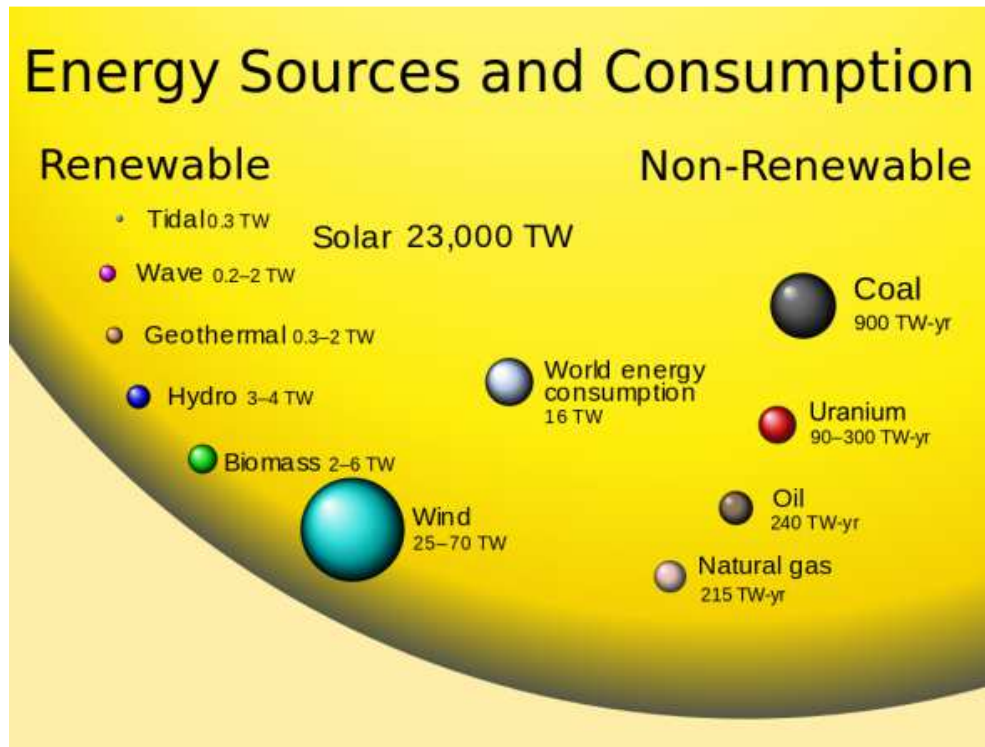


Figure 1.2: Global energy potential. Comparison between renewable and non-renewable energy sources by their potential.[6]

In reality, however, only a tiny amount of solar power, approximately 1368 Wm^{-2} , reaches the outer boundary of the atmosphere that protects the Earth. This value is called solar constant. As observed in **figure 1.3**, the quantity and quality of solar radiation reaching the Earth's surface are rather different from extraterrestrial flux.

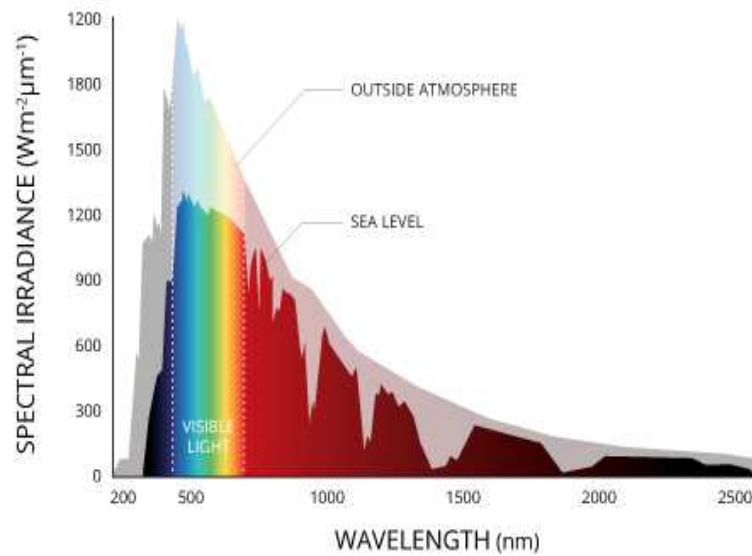


Figure 1.3: Solar irradiance spectrum outside atmosphere (transparent area) and at sea level (rainbow area) [7]

This is due to several effects, including the reflectivity of clouds, the absorption and scattering by atmospheric gases and particles. These combined effects reduce the average density of the solar radiation to about one-eighth of the solar constant, that is, 170Wm^{-2} for ocean and 180Wm^{-2} for continents. Given that the atmosphere plays a relevant role on attenuating the Earth's incoming electromagnetic flux, we need to introduce a convenient way to define solar radiation which reaches the Earth's surface. The air mass (AM) generally indicates the optical path-length of light through the atmosphere and is defined as the secant between the Sun and the zenith ($\text{AM} = 1/\cos(\theta)$). AM0 indicates solar radiation just outside the Earth's atmosphere, while AM 1.5 corresponds to a solar zenith angle 48.5° . Commonly the AM 1.5 is used as standard reference to measure the

efficiency of any solar cell. Obviously, even a small part of this enormous value could easily satisfy the global demand (16 TW). For this reason, sunlight-electricity conversion devices exploiting photovoltaic (PV) effect have experienced a rapid development in the past decades.

1.1.2 Light-energy conversion

The creation of an electric current within a material upon exposure to electromagnetic radiation is termed photovoltaic (PV) effect. Although many people consider the PV effect related to the photoelectric effect, the two processes are slightly different. In fact, while in the photoelectric effect electrons are ejected from the material surface upon exposure to radiation with sufficient energy, in the PV effect electrons are transferred to the conduction band of the material so becoming available to produce an electrical current if moved by an internal electrical field. The beginning of photovoltaics dates back to 1839 when the French scientist Edmond Becquerel observed that a voltage and a current were produced when a silver chloride electrode, immersed in an electrolytic solution and connected to a metal counter electrode, was illuminated with white light [2]. In 1876 Adams and Day published the first scientific paper based on the photovoltaic effect and the first true cell was fabricated around 1883 by Charles Fritts. The basic principle of a PV device is relatively straightforward and based on two steps: photon absorption and photo-carrier collection. Basically, to make a solar cell, a slice of n-type semiconductor must be placed in physical contact with a slice of p-type semiconductor. The junction formation allows to create an electric potential inside two materials, which will force the electrons to move in the same direction creating electrical current. When the incoming photon

has an energy higher than the optical band-gap of the semiconductor material, it is absorbed by creating an electron-hole pair, as reported in **figure 1.4a**.

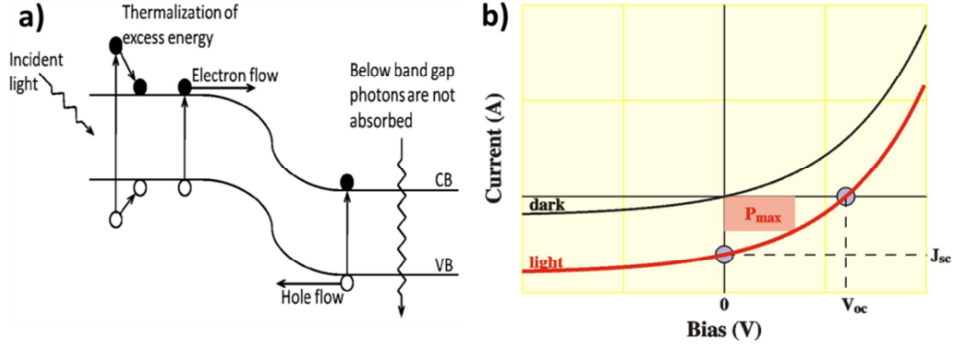


Figure 1.4: a) Schematic representation of a p-n solar cell. Photons with energies greater than the band-gap produces carriers, electrons and holes. Most important loss processes are: non-absorption of below-band-gap photons, heat losses, and radiative recombination. [8] b) The I-V curves in the dark (black) and under illumination (red) in logarithmic scale and in linear scale.

This electron-hole pair is separated and collected at the contacts of the device through the action of the internal electric field generated within the depletion region of the p-n junction. In dark condition, the I-V characteristic of a conventional p-n junction solar cell is identical to that of an ideal diode (black line in **figure 1.4b**). Under illumination, the I-V characteristic can be written as a summation of the dark diode current and the photocurrent I_L due to generated electron-hole pairs.

$$I = I_s \left[\exp\left(\frac{qV}{kT}\right) - 1 \right] - I_L \quad (1.2)$$

where I_s is the diode saturation current [9]. From equation 1.2, we obtain the open-circuit voltage by setting $I=0$, while the short-circuit current I_{sc}

represents the photocurrent extracted at $V = 0$. As can be observed in **figure 1.4b**, the I-V characteristic under illumination passes through the fourth quadrant (red line) and, therefore, power can be extracted from the device to a load. We can define the quantities I_m and V_m that correspond to the current and the voltage that maximize the power output $P_m = I_m V_m$. In this regard, the ideal conversion efficiency of a solar cell is defined as the ratio of the maximum power output over the incident light power P_{in} : $\eta = P_m / P_{in}$.

The sunlight-electricity conversion process in *p-n* junction solar cells suffers of some intrinsic losses, reported in **figure 1.4a**, that strongly limit the efficiency in these systems. The first loss is due to photons with energy below the band-gap which cannot be absorbed (*sub-band-gap losses*). On the other hand, for high energy photons the loss is due to the thermalization of high energy carriers in the conduction and valence bands. Considering these limitations, the maximum theoretical efficiency for a solar cell made from a single p-n junction is about 31% for the optimum band-gap of 1.35-1.45 eV at one sun concentration according to the detailed balance limit calculated by Shockley–Queisser (SQ) [10].

1.1.3 Research perspectives

In **figure 1.5** the evolution of efficiency for different technologies over the last 40 years are reported. All research areas have recently obtained an increase of conversion efficiency.

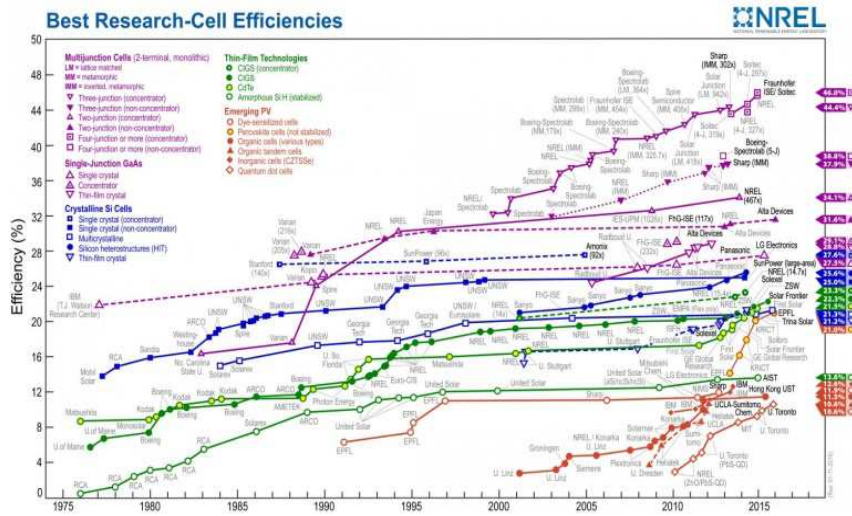


Figure 1.5: Annual growth of solar cells record efficiency. Different generations are marked with different colors [11].

Up to now the highest 1-sun efficiency of a single crystal silicon solar cell is 25.6% while that of polycrystalline silicon is 21.3%. The record efficiencies of thin film solar cells decrease further, ranging between 20% and 12%. So far, the highest efficiency of 34.1% for a single junction cell was achieved with gallium arsenide due to its direct band-gap (allowing higher absorption). Besides Si wafer, several thin-film solar cell technologies have been commercialized, including Si in either amorphous (a-Si) or microcrystalline (μ c-Si) form and metal chalcogenides (CdTe and $\text{CuIn}_x\text{Ga}_{1-x}\text{Se}_2$ (CIGS)). Their record efficiencies range in between 12% and 20%. As described in the previous paragraph, one of the main limitation of the current PV technology is related to the capability of the material to absorb the incident light. To optimize the performances we need to focus on the optimization of photon absorption and photo-carrier extraction mechanisms. In this regard, the exploitation of “*new materials*”, as perovskite, could meet

the requirements of optimized light-conversion efficiency and low cost production costs. In the **figure 1.5** is shown the meteoric rise of power conversion efficiencies of the perovskite compared to most other technologies over a relatively short period of time. Perovskite refers to any material sharing the crystal structure of calcium titanate (CaTiO_3), based on the general formula ABX_3 . When used in solar cells, A is typically a small carbon-based (organic) molecular cation, B is a metal ion such as lead, and X is a halide such as iodide, bromide or chloride. These “organo-metal halide” perovskites were studied extensively throughout the 1990s but were overlooked for solar cells until 2009, when these materials were used in liquid electrolyte dye-sensitized solar cells (DSSC). Unfortunately, the electrolyte solution dissolved the perovskite, making the solar cell highly unstable. In order to overcome this problem, in 2012 several groups replaced the liquid electrolyte with a stable solid-state version. From that moment on, the efficiency of perovskite solar cells began to grow exponentially with time. The current research cell record efficiency for perovskite was achieved by researchers at Korea University of Science and Technology with 20.1% [12].]. Organo-metal halide perovskites have many distinct advantages over traditional solar cell materials. Firstly, these perovskites can be processed using very simple, low-cost methods. The wafer processing and cell fabrication associated with silicon require expensive equipment and facilities. In comparison, perovskite cell fabrication has been accomplished with simpler methods like solution spin coating. [13]. Moreover, it is also possible to process them on flexible substrates, such as plastic or fabric, opening up a number of portable electronics applications. Secondly, the constituent elements in the ABX_3 crystal structure can be widely tuned to give a range of desired optical and electrical properties. Additionally,

perovskite cells have a higher band-gap than traditional silicon or thin film cells. Therefore, they are transparent to typical solar absorption wavelengths and can be placed on top of lower band-gap cells. This combined "tandem" photovoltaic system is able to absorb a great part of the solar spectrum and achieves a higher efficiency than each type of cell individually.

Currently, other strategies have been suggested in order to reduce the cell fabrication costs and push the efficiencies above Shockley and Queisser limit. This would make the electricity production cost by solar cells commercially competitive with respect to others conventional energy sources. The developments have taken many directions, which can be categorized in different forms. In this regard, three different approaches in the light absorption management and in the optimization of the photocarriers extraction are presented below and in figure 1.6:

- The first approach is represented by *multi-junction solar cells (MJSC)* in which the use of several different cells material (figure 1.6a), each one with different band-gap, allows the absorption in a broader range of the solar spectrum, increasing the output power of system. A generalized theory based on 2-4 and beyond number of band-gaps demonstrate that maximum efficiency, at a concentration of 1 sun, is 31%. At a concentration of 1000 suns with the cell at 300°K, the maximum efficiencies are 37, 50, 56, and 72% for cells with 1, 2, 3, and 36 energy gaps, respectively [14]. The highest efficiency, experimentally reached by MJSC, is 46% under 508 suns [15]. This cell stacks four p-n junctions made of $\text{Ga}_x\text{In}_{1-x}\text{As}$ or $\text{Ga}_y\text{In}_{1-y}\text{P}$ with different compositions. Each junction has a different band-gap and is responsible for the light absorption in a certain

portion of the solar spectrum. However, the disadvantages of this approach relies on the complexity and the high cost of the structure that limits its applicability on large scale.

- Another leading concept for increasing the efficiency of solar cell is the *intermediate band (IB) solar cell* (figure 1.6b). The idea is to increase the light absorption of the solar spectrum by introducing states within the band-gap of semiconductor materials. In this way, low energy photons can be absorbed in a two photon process. One of these structures, such as ZnCdTe system implanted with high energy oxygen ions, would have a limiting efficiency of 60%. Moreover, the use of quantum dot superlattices to form an effective intermediate band structure has been studied by Luque et al [16], [17] who showed promising results. However, the main issue of this approach is the achievement of strong light absorption from IB without increasing non-radiative recombination processes. Furthermore, IB must be electronically separated from valence and conduction bands, otherwise the photo-voltage would be reduced.
- A third approach for high efficiency solar cells is the concept of *carrier multiplication* (figure 1.6c). This implies that for a single absorbed photon, more than one electron-hole pair is generated, mainly by an avalanche-type process. Such effect is usually called *multiple exciton generation* (MEG) and has been observed in bulk semiconductors (such as Si-Ge alloys) as well as in quantum dots (PbSe, CdTe, CdSe, Si) [18], [19]. Recently, photoluminescence experiments on PbSe and PbS nanocrystals have shown that is possible to get up to 7 excitons for a single absorbed photon [20]

However, multi-excitons tend to recombine very fast (ps time scale), limiting the carrier extraction process in a future device.

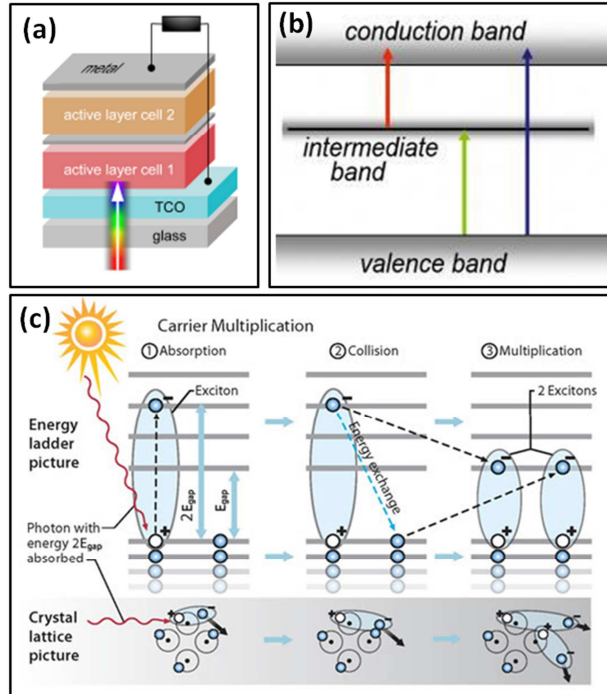


Figure 1.6: Main approaches for new generation PV cells: **(a)** Multi-junction; **(b)** intermediate-band solar cell; **(c)** Carrier multiplication process (called impact ionization in bulk semiconductor).

The field of nano-photovoltaics is relatively new and there are many exciting perspectives to apply nanostructures and nanotechnology to PV. However, although the future of nanostructures for photovoltaics is promising, many technological challenges remain and fundamental and technological works are needed in this field.

1.2 Quantum confinement effect

Nanotechnology is defined as the study and use of structures whose size is between 1 nm and 100 nm. The birth of Nanotechnology concept is attributable to Feynman's famous lecture in 1959, called "There is plenty of room at the bottom". From then on, nanostructures have received an increasingly interest in all disciplines of science. There are various reasons why nanoscience and nanotechnologies are so promising in materials, engineering and related sciences. First of all, at the nanometer scale, some physical properties of the matter drastically change, such as melting point, color and so on. These changes are a direct consequence of the small size of nanomaterials, physically explained as quantum confinement effects. In particular, when the size of any material (metal or semiconductor) is reduced to the nanometer scale, the physical properties are very different from those observed in a bulk form. For instance, bulk gold is yellow, whereas gold nanoparticles have different color depending on the size. Another important characteristic of nanomaterials is an increased surface-to-volume ratio compared to bulk materials. This aspect is very important for all those processes where the surface of a material plays a key role, such as catalysis and detection processes. For these reason the nanotechnology opened the way to a new era in many fields, most of which have a huge impact on our daily life, from nano-optoelectronic [21], nano-biology [22]-[23], chemical sensors [24]-[25], nanomedicine [26]-[27], and to new concepts for high efficient light harvesters and solar cells [28].

One of the most important feature in nanostructures is the quantum confinement effect, which is essentially due to changes in the electronic energy configuration [29]-[30]. In the quantum confinement regime, carriers

“feel” the presence of the particle boundaries and respond to changes in particle size by adjusting their energy. This effect happens through the use of a confining potential due to band-gap differences with a surrounding matrix material. Quantization effects become most important when the particle dimension of a semiconductor is near to and below the bulk semiconductor Bohr exciton radius ($r_B = \frac{a_0 \epsilon}{m^*}$ where ϵ is the dielectric function, a_0 is Bohr radius and m^* is the reduced mass of carriers) which makes material properties size-dependent. The Bohr radius in a semiconductor is of the order of a few to tens nanometers. A quantum confined structure will be classified on the base of its confinement dimensions, as reported in **figure 1.7a**. In QDs, the charge carriers are confined in all dimensions, quantum wires are formed when two dimensions of the system are confined while in quantum well charge carriers (electrons and holes) are confined to move in a plane and are free to move in a two dimensional space.

Many differences between electronic behavior of bulk and quantum confined semiconductor systems are related to their density of electronic states. **Figure 1.7b** illustrates how the expected density of states varies with the dimensionality, passing from continuous dependence for bulk system to a step-like dependence in confined systems. This variation is due to collapse of energy states of the system from continuous energy bands, typical of bulk semiconductor, to the discrete distribution of confined systems (**figure.1.7c**).

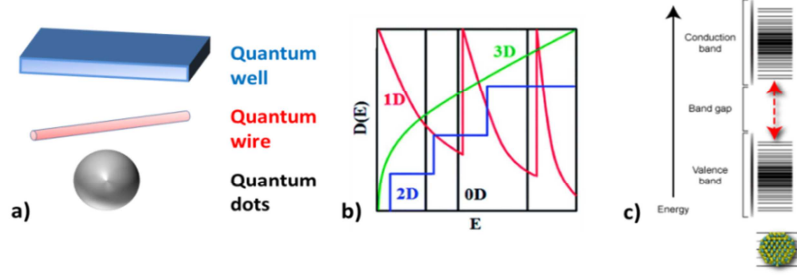


Figure 1.7: a) Schematic representation of quantum well quantum wire and quantum dot; b) density of electron states for bulk (green line), quantum well (blue line), wire (red line) and dot (black line); c) schematic of the discrete energy levels in conduction and valence band for semiconductor NS.

The quantum confinement effect can be estimated via a simple *effective-mass approximation model* (EMA). Thanks to this model we are able to predict the confined energy levels of nanostructures by solving Schrödinger equation assuming the barriers have an infinite confining potential. The eigenvalues and eigenfunctions of the Schrödinger equation for electrons confined in a QD, quantum wire and quantum well are reported in **table 1.1**:

Confinement	Eigenvalues	Eigenfunctions
3D (quantum dot)	$E_{n,m,l} = \frac{\hbar^2 \pi^2}{2m^*} \left(\frac{n^2}{L_z^2} + \frac{m^2}{L_y^2} + \frac{l^2}{L_x^2} \right)$	$\psi = \phi(z)\phi(y)\phi(x)$
2D(quantum wire)	$E_{n,m}(k_x) = \frac{\hbar^2 \pi^2}{2m^*} \left(\frac{n^2}{L_z^2} + \frac{m^2}{L_y^2} \right) + \frac{\hbar^2 k_x^2}{2m^*}$	$\psi = \phi(z)\phi(y)e^{ik_x x}$
1D(quantum well)	$E_n(k_x, k_y) = \frac{\hbar^2 \pi^2 n^2}{2m^*} + \frac{\hbar^2 (k_x^2 + k_y^2)}{2m^*}$	$\psi = \phi(z)e^{ik_x x}e^{ik_y y}$

Table 1.1: Eigenvalues and eigenfunctions of the Schrodinger equation for electrons confined in quantum dot, quantum wire and quantum well

where n , l and m are the quantum confinement numbers, m^* is the effective mass, L_x , L_y and L_z are the confining dimensions, and $e^{i(k_x x + k_y y)}$ is the wave function describing the electronic motion in x and y direction which is similar to free electron wave function. Also, the band-gap energy (defined as the energy distance between the top of valence band and the bottom of conduction band) along the confinement direction of nanostructure can be modeled within EMA by the following equation:

$$E_g(QD) = E_g^{bulk} + \frac{\pi^2 \hbar^2}{2m^* L^2} \quad (1.4)$$

The second term of the previous equation is the additional energy related to quantum confinement where E_g^{bulk} represents the band-gap of unconfined system and $A = \frac{\pi^2 \hbar^2}{2m^*}$ is a confinement parameter. Equation (1.4) shows that the band-gap of a NS is increased with respect to the bulk material by a quantity which is inversely proportional to the square of its size L and to the effective mass of the electron-hole pair m^* . In particular, the A parameter appears to be inversely proportional to the effective mass ($A \propto \frac{1}{m^*}$). Clearly, a reduction of effective mass, due for example to better quality of NS interface, gives rise an increase of A parameter and consequently of the quantum confinement, allowing a stronger and easier modulation of optical band-gap. Moreover, given its dependence on effective mass, the A parameter changes depending on the material of which the NS is composed. As an example in **table 1.2**, the A parameter values carry out for Si and Ge and for confinement 1D, 2D and 3D are reported. The higher values of A observed in Ge NS (1D, 2D or 3D) suggest, together with higher exciton Bohr radius (r_B , ~5 nm in Si and ~24 nm in Ge [31]), that the E_g modulation in Ge NS is much easier with respect to Si NS.

Confinement	A [eV*nm ²]	
	Si	Ge
3D (Quantum dot)	3.57	7.88
2D (Quantum wire)	2.09	4.62
1D (Quantum well)	0.89	1.97

Table 1.2: A parameter for 3D,2D, 1D confinement for Si and Ge [32].

For this reason, the Ge NS have recently received a renewed attention over Si NS for several light harvesting application.

Other two terms should be taken into account in equation 1.4 which is a simplified formula. These two terms are: a) the coulomb interaction between electron and hole and b) the energy splitting caused by the spin-orbit interaction. However, these two terms, which have an overall L^{-1} dependence, produce little variations (~ 50 meV) with respect to values obtained from equation 1.4 and so they are negligible. In particular, the energy coulomb interaction for the excitons is often neglected due to the high dielectric constant of the semiconductor material. The equation 1.4 is valid in the case of an infinite confining potential. As drawn in **figure 1.8**, a significant deviation from equation 1.4 occurs when NS are embedded in a real matrix, where confining potential (V_0) is finite. The E_g values of NS in this condition is reduced by factor $\left[1 + \frac{\hbar}{r\sqrt{2m^*V_0}}\right]^2$ from values obtained by equation 1.4 [33]-[34]-[35]. Hence, the reduction of the barrier height reduces the effectiveness of quantum confinement. The variation of optical band-gap with NS size represents one of the most important and useful properties of nanostructures. This effect can be used for the light

management and to improve the light harvesting in solar cells and photodetectors. The most important example of light absorption based on the gap tailoring in QCE is represented by the *all Silicon quantum dot tandem solar cell*. This idea, proposed by Green et al [36], consists in a MJSC composed by a multiple stack of Si QD where the size of QDs in each sub cell is varied in order to tune E_g . This kind of band-gap engineering allows the absorption of a larger portion of the solar spectrum using only one type of material and therefore reducing the production costs of the MJSC.

Up to now, several experimental and theoretical studies have highlighted how the band-gap variation can be performed not only by changing the size, but also playing with other parameters, such as: the nanostructure shape [37], the QD crystalline structure [38]-[39], or the potential barriers surrounding the QD [34]-[40]-[41]. Recent works focused on the role of the interface with respect to the quantum confinement effects [42]-[43]-[44]. In this regard, it is fair to point out that EMA model is usually used to describe carrier confinement in sharp and square-shaped potential barrier systems, considering bulk values of EM and neglecting any effect caused by a spatially-graded confinement potential, typical in the case of an interface shell between QD and matrix. Thus, in order to describe the effects of the interface and the variation of EM in nanostructured systems on QCE, the theoretical correction to the EMA model was developed through a spatially dependent effective mass (SPDEM) formalism which is directly related to the potential $V_c(x)$ for confined carriers [45]. The SPDEM describes the effect of the confinement potential V_c on the EM, by considering a particle confined in nonadditive space. The confinement potential is chosen basing on the properties of nonadditive space (breaking of translational symmetry)

and lead to analytic solutions for the confinement Hamiltonian. This implies the following dispersion relationship [46]:

$$E_g(D) = E_g^{bulk} + \frac{3\hbar}{\mu(D)\sqrt{2} \cdot D} \left[\sqrt{\frac{V_{c,e}}{m_{c,e}^*}} + \sqrt{\frac{V_{c,h}}{m_{c,h}^*}} \right] \quad (1.5)$$

where $\mu(D)$ is the renormalized SPDEM of excitons, while $V_{c,e}$ and $V_{c,h}$ are the confinement potential for an electron and hole, respectively[44]-[47]-[48]. Thus, the variation of EM with NS size strongly affects the band-gap tailoring due to QCE, as reported with blue symbol and line in **figure 1.8**.

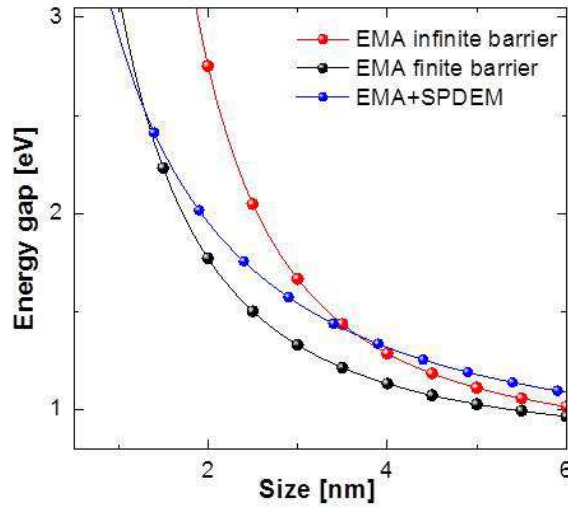


Figure 1.8: Theoretical size dependent of optical band-gap for Ge NS calculated by using the EMA finite barrier, EMA infinite barrier and EMA+SPDEM relationships

Besides the band-gap tailoring, the increase of the oscillator strength is usually reported, both experimentally and theoretically, in highly confined systems. This effect is strictly related to the reduction system dimensions. The reduction of system leads to the breaking of the k-conservation rule for optical transitions, which is in turn related to the Heisenberg uncertainty

principle. Moreover, the confinement of carriers in the real space generates a spread out of their electronic wavefunctions in the momentum space. So, the increase of dispersion in momentum space, due to the reduction of confinement dimensions, results in a larger overlap of electron-hole wavefunctions which leads to an increase of the probability of optical transitions between valence and conduction band states. In the next paragraphs and chapters, we'll show how the interfaces can strongly influence the optical properties of confined systems.

It is clear that a deeper understanding of the mechanisms that modify the QCE is needed in order to have a reliable control of the optical properties of nanostructures. In this way, the optimization of the light absorption processes in new materials containing NS can be achieved, allowing them to be exploited in photovoltaic applications. For this reason, in the next paragraph, we will give a brief overview about the theory of the light absorption, starting with bulk semiconductors until describing NS materials.

1.3 Light absorption in quantum structures

1.3.1 Light Absorption in semiconductors: dielectric function

Optical emission and absorption are fundamental processes which are exploited to describe the interaction of light with matter. In previous paragraph, we have shown that the electronic properties of NS are particularly sensitive to the NS/matrix interface, presence of defects and impurities that can reduce the quantum confinement effect occurring in confined systems. For this reason, a modeling of the light-matter interaction is needed, especially for the optical absorption mechanism.

The optical properties of semiconductor are defined in the 1-10 eV energy range due to the inter-band transitions and can be modeled within the semi classical theory. We consider a transverse electromagnetic wave propagating in a medium and having a corresponding vector potential:

$$A(r, t) = A_0 e^{i(q \cdot r - \omega t)} \quad (1.6)$$

where A_0 and ω_0 are the amplitude and frequency of radiation while \mathbf{q} is the wave vector of photons. When a semiconductor is irradiated by light, electrons can be excited from valence band (VB) into the conduction band (CB) by the absorption of photons having energy greater than E_g .

The total rate of interband transitions per unit volume $W(\omega)$, induced by perturbation $A(r,t)$, is obtained by summing the transition probability over all the allowed \mathbf{k} in the Brillouin zone between valence and conduction band:

$$W(\omega) = \sum_{VB,CB} \int_{BZ} \frac{2 dk}{(2\pi)^3} P_{vK_i \rightarrow ck_f} \quad (1.7)$$

where $P_{vK_i \rightarrow ck_f}$ represents the transition probability of an electron from the initial state in the valence band to the final state in the conduction band, generated by the absorption of a photon with energy $\hbar\omega$ higher than optical band-gap of the material. The probability $P_{vK_i \rightarrow ck_f}$ term is obtained from the ‘‘Fermi Golden Rule’’ [49]-[50]:

$$P_{vK_i \rightarrow ck_f} = \frac{2\pi}{\hbar} \left(\frac{eA_0}{mc} \right)^2 \cdot \left| \left\langle \phi_{ck_f} \left| e^{iqr} e_0 \cdot p \right| \phi_{vK_i} \right\rangle \right|^2 \delta(E_f - E_i - \hbar\omega) \quad (1.8)$$

The absorption coefficient of electromagnetic waves is defined as the ratio between the energy absorbed per unit of time and the volume and average energy flow given by the following expression $u \left(\frac{c}{n} \right) = \frac{n^2 A_0^2 \omega^2}{2\pi c^2}$. So, the

absorption coefficient is related to the transition probability by the following relation:

$$\alpha(\omega) = \frac{W(\omega) \hbar \omega}{u\left(\frac{c}{n}\right)} \quad (1.9)$$

where n is the refractive index of the medium.

Substituting the equations (1.7) and (1.8) in the relation (1.9), the absorption coefficient of a semiconductor material can be expressed as:

$$a(\omega) = \frac{4\pi^2 e^2}{n c m^2 \omega} \sum_{VB,CB} \int_{BZ}^{\forall k} \frac{2dk}{(2\pi)^3} |M_{cv}(k)|^2 \delta(E_f - E_i - \hbar\omega) \quad (1.10)$$

where $|M_{cv}(k)| = \left\langle \varphi_{c,k_f} \left| e^{i\vec{q} \cdot \vec{r}} \vec{e}_0 \cdot \vec{p} \right| \varphi_{v,k_i} \right\rangle$ is the momentum matrix element which describes the real probability of the electronic transition.

For the calculation of the optical properties of crystals it is sometimes convenient to express the absorption in terms of the imaginary part of the dielectric function ε_2 :

$$\varepsilon_2 = \frac{\alpha n c}{\omega} \quad (1.11)$$

which from equation (1.10) becomes:

$$\varepsilon_2(\omega) = \frac{4\pi^2 e^2}{m^2 \omega^2} \sum_{VB,CB} \int_{BZ}^{\forall k} \frac{2dk}{(2\pi)^3} |M_{cv}(k)|^2 \delta(E_f - E_i - \hbar\omega) \quad (1.12)$$

Clearly, starting from the ε_2 expression, the real part ε_1 of dielectric function is derived by using the Kramers and Kronig integration.

Sometimes, it is convenient to use the matrix element of dipole electric as an alternative of matrix element of momentum. So, by exploiting the relation between two matrix elements given by the Heisenberg relation:

$$M_{cv}(k) = \left\langle \varphi_{c,k_f} \left| \vec{p} \right| \varphi_{v,k_i} \right\rangle = \frac{im}{\hbar} (E_f - E_0) \left\langle \varphi_{c,k_f} \left| \vec{r} \right| \varphi_{v,k_i} \right\rangle \quad (1.13)$$

So, the relation 1.13 can be equivalently re-written as:

$$\varepsilon_2(\omega) = \frac{4\pi^2 e^2}{\hbar\omega} \sum_{VB,CB} \int_{BZ}^{\forall k} \frac{2dk}{(2\pi)^3} (E_f - E_0) |R_{cv}(k)|^2 \delta(E_f - E_i - \hbar\omega) \quad (1.14)$$

where in the $M_{cv}(k)$ expression, we have considered $e^{i\vec{q} \cdot \vec{r}} \cong 1$ given that the distance over which the electronic wavefunctions vary is smaller with respect to $\frac{1}{q} = \frac{\lambda}{2\pi} = 10^3 \text{Å}$.

1.3.2 Light Absorption in semiconductors: absorption coefficient

In the previous paragraph we have focused on the dielectric function (DF) of semiconductor. Once the DF is expressed, the absorption coefficient α of system can be obtained using the relation (1.11). The optical absorption coefficient is the most important parameter to study the optical behavior of a material and it determines the penetration depth $1/\alpha$ of the light in a material according to Lambert-Beer's Law:

$$I = I_0 e^{-\alpha x} \quad (1.15)$$

Under assumptions of parabolic band edge, starting from the relation 1.10 and introducing the concept of reduced mass for electron-hole pair ($m_r^{-1} = m_c^{-1} + m_v^{-1}$), J. Bardeen, F. J. Blatt and L. H. Hall predicted that the absorption coefficient for direct band to band transitions in the absence of exciton effects for crystalline bulk semiconductor can be expressed as follows [51]:

$$\alpha(\omega) = \frac{C}{\hbar\omega} (\hbar\omega - E_g)^{1/2} \quad (1.16)$$

where E_g is the direct optical band-gap value of the semiconductor material while C is a constant, related to absorption efficiency of under investigation system.

The equation 1.16 is not valid to obtain the α spectra in amorphous semiconductors. In fact, in crystalline semiconductors the distributions of states in VB and CB clearly terminate at their respective band edges, as reported in **figure 1.9a**. This leads to a well-defined band-gap for this materials. The situation changes when we consider the amorphous semiconductors materials. In fact, in these materials the presence of disorder, often associated with variations in the bond lengths, bond angles, defect intrinsic, dangling bonds and vacancies, leads to changes in the density of states (DOS) in VB and CB. In particular, the DOS in amorphous materials does not terminate at the band edges (both in VB and CB), spreading into the forbidden region (**figure 1.9b**). This is due to the formation of localized states in which the electronic wave-functions are more spatially confined with respect to the crystalline case. In this regard, the \mathbf{k} conservation selection rule is relaxed at least at the band edges and \mathbf{k} is not a good quantum number anymore. This breakdown of the momentum selection rules leads to an increase of the absorption efficiency in amorphous samples with respect to the crystalline one, especially below the band-gap region. Under this circumstances, the equations 1.16 is not able to describe correctly the energy-dependence of the absorption coefficient and the empirical equation is needed.

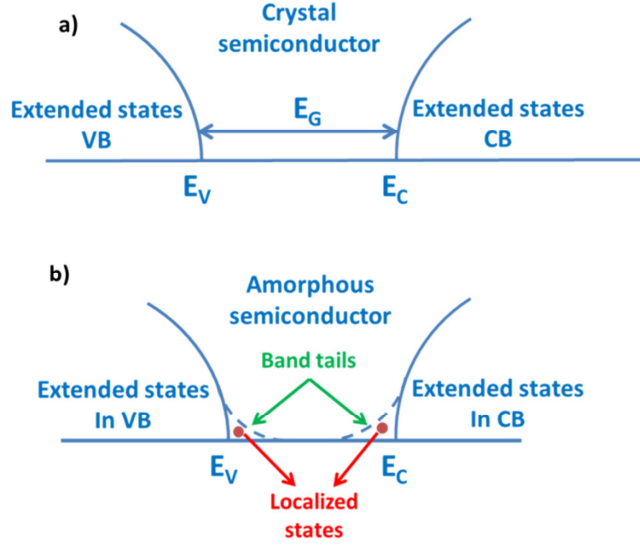


Figure 1.9: Schematic density of states as a function of energy for a crystalline (a) and amorphous semiconductor (b).

So, in this case, it is possible to use models based on experimental observations. The two major models used to describe the optical absorption features in the high absorption region ($\alpha \geq 10^4 \text{ cm}^{-1}$) for amorphous semiconductors are Tauc and Cody models. These two models are based on two different assumptions:

- $M_{cv}(k)$ varies slowly with k for Tauc model,
- $R_{cv}(k)$ varies slowly with k for Cody model.

By imposing the condition (a) in the equation 1.12 (containing the dipole matrix element $M_{cv}(k)$), it is possible to neglect the k dependence of $M_{cv}(k)$ and to take it out of the summation. In this way, the absorption coefficient can be re-written in a simplified form as:

$$\alpha(\omega) = \frac{4\pi^2 e^2}{n c m^2 \omega} \cdot J_{vc} \cdot |M_{cv}|^2 \quad (1.17)$$

where $J_{vc} = \int_{BZ} \frac{2dk}{(2\pi)^3} \delta(E_f - E_i - \hbar\omega)$ is the joint density of states (JDOS) between valence and conduction bands involved in the absorption process of one photon with energy $\hbar\omega$. The term $O_S = \frac{2|M_{cv}|^2}{m\hbar\omega}$ in equation 1.13, is known as the oscillator strength of the optical transition and gives an estimation of the coupling intensity between states in valence and conduction bands which participate in the light absorption process. Finally, assuming the parabolic band-edges of valence and conduction band and the optical transitions between extended states from VB toward CB (for values of $\alpha > 10^4 \text{ cm}^{-1}$), one gets $JDOS \propto (h\nu - E_g)^2$. Thus α can be re-written as [52]-[53]:

$$\alpha = \frac{B_{Tauc}}{\hbar\omega} (\hbar\omega - E_g)^2 \quad (1.18)$$

where E_g is the optical band-gap of the material. The relation 1.18 is known as Tauc's law and is successfully used to describe the higher part of α in amorphous semiconductors [53]-[54]. The Tauc coefficient B_{Tauc} is proportional, through the momentum matrix element $|M_{cv}|^2$, to the oscillator strength which it measures the intensity of coupling between states in valence and conduction band [52]. Finally, the equation 1.18 can be linearized by plotting $\sqrt{\alpha\hbar\omega}$ and the values of E_g and B can be extracted as the energy axis intercept and slope of linear fit. The Tauc model was successfully used for the first time to describe the absorption behavior of an amorphous Ge thin film [53]. In **figure 1.10**, we reported an example of Tauc plot performed on 120 nm thick amorphous Ge film⁵³. For larger values of α (typically $> 10^4 \text{ cm}^{-1}$) the trend is linear and gives an optical band-gap for a-Ge of $E_g = 0.88 \text{ eV}$. For low values of α the trend of Tauc plot

is not linear because of the contribution of transitions related to distorted (more or less localized) states near the band edges (Urbach region).

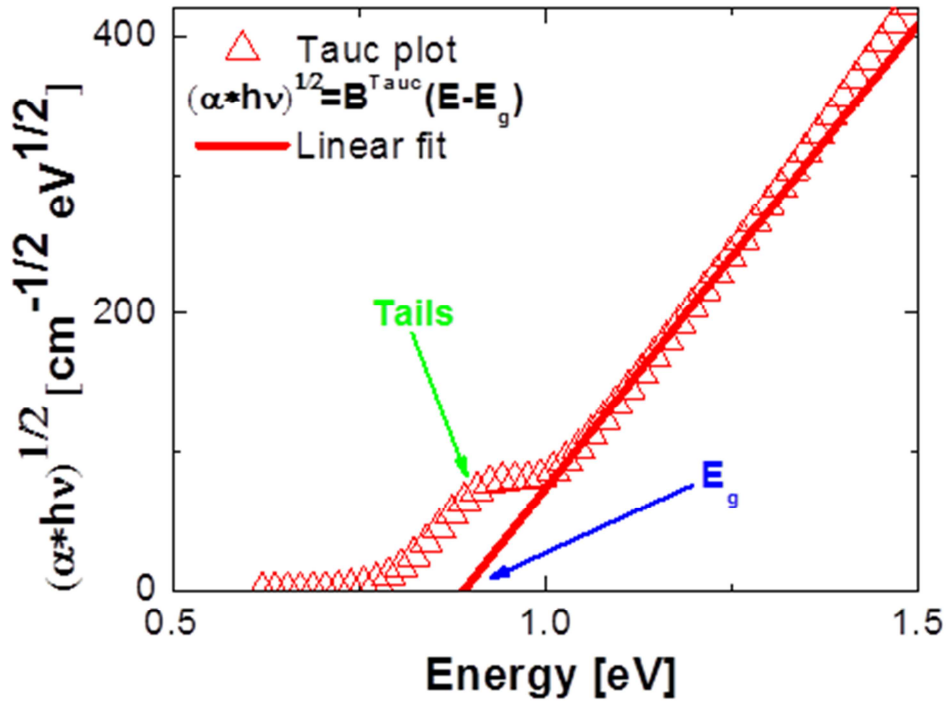


Figure 12.10 Example of Tauc plot and corresponding linear fit performed on amorphous Ge film.

For most amorphous semiconductors, especially as regards a-Si and a-Si:H films, the Tauc optical gap shows a good agreement with other methods employing electrical conductivity measurements. In this regard, the Tauc plot had been considered for a long time the best method to determine the energy gap of amorphous semiconductors. Later studies, performed on a-Si:H films, showed the presence of a significant curvature in the spectral dependence of Tauc plot which is more visible as the thickness of film increases [54]. This curvature was demonstrated that plays a significant role

in influencing the determination of the Tauc optical band-gap. In this regard, Cody et al proposed an alternative model, based on constant dipole matrix approximation. In fact, by imposing the condition **(b)** in the equation 1.14 (containing the dipole matrix element $R_{cv}(k)$), Cody et al demonstrated, for parabolic band edges of valence and conduction band and for sufficiently large values of energy photon, that the absorption coefficient can be written as [55]:

$$\alpha = B_{Cody} \hbar\omega (\hbar\omega - E_g)^2 \quad (1.19)$$

Also this model allows to obtain the optical band-gap of amorphous materials by linear extrapolation of the spectral dependence of $\sqrt{\alpha/\hbar\omega}$. The so extracted band-gap is sometimes referred to as the Cody optical band-gap [55].

To date, a heated debate is underway about the range of applicability of these two models in order to extract the optical band-gap of amorphous semiconductors. Recently, a strong thickness film dependence of the Cody plot, was also observed in a-Si:H films, proving the existence of limitations also for the application of Cody model. Moreover, different behavior of Cody and Tauc plot may be observed depending on the material under investigation.

1.3.3 Light Absorption in semiconductor NS

In the previous paragraph, we have observed that when the size of material is reduced the main observable effect is the shift of the absorption edge towards higher energies related to QCE, according to equation 1.4. In reality, other two effects are attributable to a reduction of dimensionality in nanostructured systems. The first is the modification of the features in absorption spectra related to the discretization of states in VB and CB which in turn affects the JDOS. In addition, as a consequence of the reduced dimensionality occurring in confined system, electron-hole pair become confined in a tight space, giving rise to larger overlap of their wave-functions. This overlap of wave-functions leads to an increase of the oscillator strength, which in turn produces an increase of the optical transition rate. This leads to a significant increase of the absorption efficiency of the system with respect to bulk condition. Such effect can be exploited for boosting the efficiency of novel devices, such as solar cells, lasers or photodetectors. The increase of the oscillator strength with the reduction of NS size is confirmed by a recent study presented by Kuo et al. In this work, they showed the increase of radiative optical transition rate due to exciton coupling and larger oscillator strength in crystalline Ge QWs [56]. **Figure 1.11** shows the exciton radius and optical strength of the direct band edge transition for c-Ge QW as function of QW thickness and extracted through the variational calculations [56]. It is clear that as thickness is reduced, the exciton radius decrease due to the strong confinement while the oscillator strength doubles.

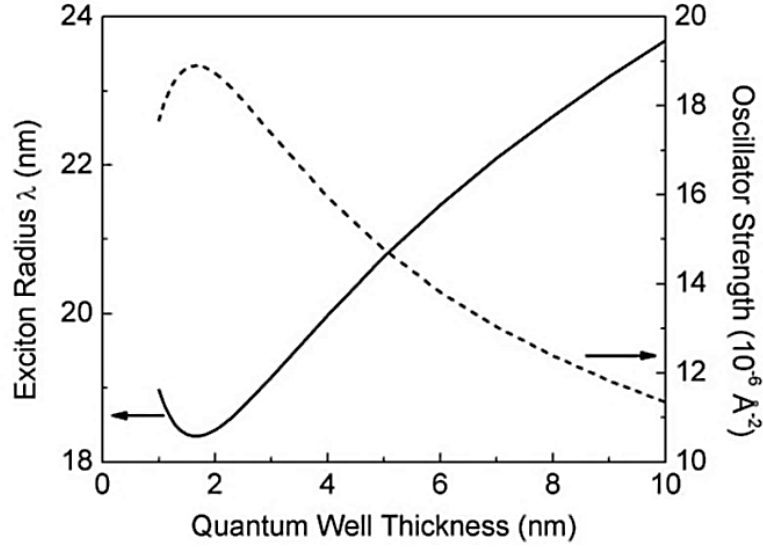


Figure 1.11: The oscillator strength and exciton radius versus thickness of Ge/SiGe quantum well. The values of oscillator strength and exciton radius were extracted by using the variational method. [56]

Still, the size seems to be not the only parameter driving QCE. Recent studies have demonstrated how the optical properties of semiconductor NS can be strongly influenced by other structural parameters as: QD-QD distance, presence of chemical states at interface and physical effects at interface [57]-[58]-[59]. For instance, a recent theoretical study demonstrated that the relaxation of momentum conservation rule observed in Si NCs is not only due to the Heisenberg uncertainty principle. They claim that “*the relaxation of the momentum conservation rule in Si NCs are joint effects of both the Heisenberg uncertainty principle and interface scattering induced $-X$ coupling*”. The scattering at the interface of NCs gives rise to mixing of X- and Γ - character of conduction band states, enabling an increase of zero phonon quasi-direct transitions. This helps explain the experimentally observed enhanced absorption for Si/Ge superlattices and Si

NC samples [58]. Moreover, this mechanism of scattering-induced states mixing could provide a new way to treat the NC surface to enhance the optical absorption of semiconductor NCs.

Another evidence of interface effects on optical properties in semiconductor NSs is suggested by the recent work by Talochkin et al. In this work ,they observed an enhancement of light absorption in Si/Ge(GeSn)/Si structures. In this work, the ultra-thin Ge (1.2 nm and 2.3 nm) or GeSn layers (1nm) were grown by low temperature molecular beam epitaxy (LT-MBE) on Si substrate, determining the formation of Ge islands pseudomorphic to Si, as reported in **figure 1.12**.

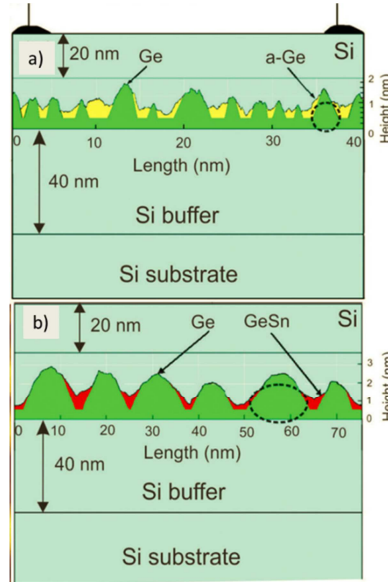


Figure 1.12: Schematic representation of Ge and GeSn layers with thicknesses of 1.0 and 2.0nm, respectively. **(a)** and **(b)** [60].

In both types of samples, the absorption coefficient, extracted through the photoconductivity measures and by using the simple diffusion model, was 100 times higher ($\sim 10^5 \text{ cm}^{-1}$) than that observed of a single Ge QD layer (10^3

cm^{-1}). The anomalous high value of absorption coefficient was explained by the presence of high concentration of dangling bonds located at interfaces of Ge islands which produce the electron-hole states originated from band edge states [60]. In particular, the observed electron-hole states are localized at the Ge/a-Ge (red and yellow area in figure 1.12) and a-Ge/Si interfaces. The high magnitudes of α , determined in this work, agree well with the results of previous theoretical calculations performed by Knief and von Niessen [54]. However, not only surface effects can strongly influence and enhance the absorption of semiconductor NS. A very recent study was focused on the variation of joint local density of states as function of distance between colloidal semiconductor QDs. To this purpose, PbS QDs capped with various organic ligands self-assembled in close-packed arrays with hexagonal symmetry were synthesized. Spacing control of QDs control was achieved by exchanging the as-synthesized oleic acid ligands (denoted C18) with three alkylamine ligands of variable lengths, namely, dodecylamine (C12), octylamine (C8), and butylamine (C4). The average dot size was 5.0 nm, and dots capped with C4, C8, C12, and C18 show spacings of 0.6, 1.0, 1.5, and 2.0 nm, respectively (STEM images in figure 1.13(a-d)). The synthesis of PbS quantum dots was performed using a colloidal procedure and STEM-EELS was used on the prepared samples to measure variations in the availability of low-energy electron transitions in the space between neighboring QDs as a function of interparticle spacing. The figure 1.13 shows 2D maps of integrated EELS signal intensity of PbSe QDs for different kind of ligands [57]. In this work, as can be observed in figure 1.10 (a-d), they revealed the nonzero EELS signal in the area between the closely spaced dots, which gradually increase as the QD spacing decreases. A brief reflection on the physical origin of the EELS signal suggests that the

increased signal observed between the more proximal QDs is a result of their electronic coupling. Moreover, the intensity of EELS signal in the low loss energy range can be approximated using the Fermi's golden rule for overlapping electron and hole states near the semiconductor band edges [62]. So, we can consider the EELS signal as proportional to the joint local density of states (JLDOS), which is point-localized analogue to the joint density of states (JDOS). In this way an increase of EELS corresponds to an increase of the JDOS. This increase of the JDOS indicates a growing electronic coupling between QDs [57].

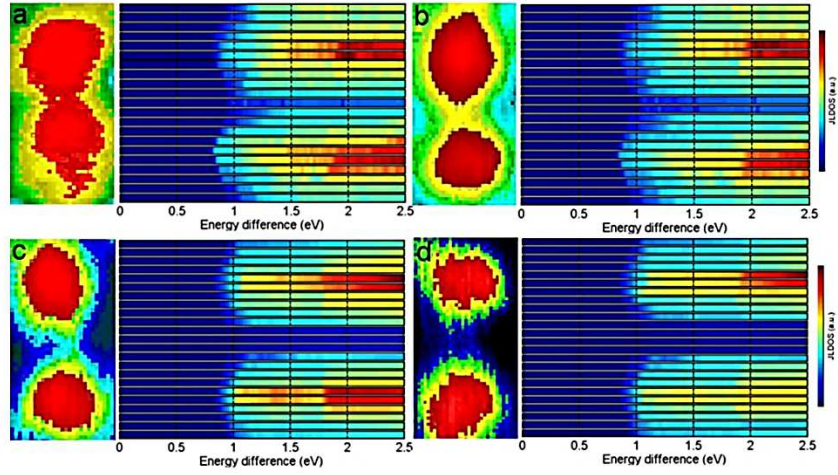


Figure 1.13: 2D maps of integrated EELS signal intensity in the energy range spans 0.9-2 eV for different QD spacing: 0.6 nm (a), 1 nm (b), 1.5 nm (c) and 2 nm (d) [57]

The enhancement of the JDOS could lead to an increase of the optical absorption of the system, given that the absorption coefficient is proportional to JDOS (as reported in equation 1.13). In this way, we would be able, playing with the distance between the QDs, to maximize the light absorption in an ensemble of QDs. This distance dependence of optical properties in an

ensemble of nanostructures can be exploited to improve the efficiency of new devices for light harvesting applications.

On the basis of evidences shown so far, the extraction of fundamental information about the optical properties of NS is needed in order to get a deeper understanding of the interaction between light and confined structures. To this aim is essential to know and to extract the energy-dependence of the absorption coefficient for nanostructured systems. The formalism used until now to describe the optical absorption in semiconductor is valid for bulk materials. Several papers in the literature utilize the Tauc and Cody models to describe the absorption process in confined systems [34]-[63]-[64], although the applicability of both methods to semiconductor NS is still one open question. In fact, as already discussed in the previous paragraph, Tauc and Cody models are based on two fundamental initial assumptions: i) parabolic band edges in VB and CB and ii) optical inter-band transitions between extended states in which the \mathbf{k} vector is not conserved [53]-[55]. The fundamental question about the validity of both methods are therefore related to the validity of the above assumptions. As regard to the relaxation of the \mathbf{k} vector, this assumption is still valid for confined structures given their reduced dimension. In addition a band diagram dispersion similar to the bulk case could be still retained also in NS, especially for QDs which size is not too small. In fact, a recent theoretical study demonstrated, using the density functional theory calculations, that the band structure concept is still valid for Si nanocrystals with a diameter larger than 2 nm. In **figure 1.14** the projected \mathbf{k} -space density is shown along the Γ -X direction in Brillouin zone and calculated for H-passivated Si NCs [65].

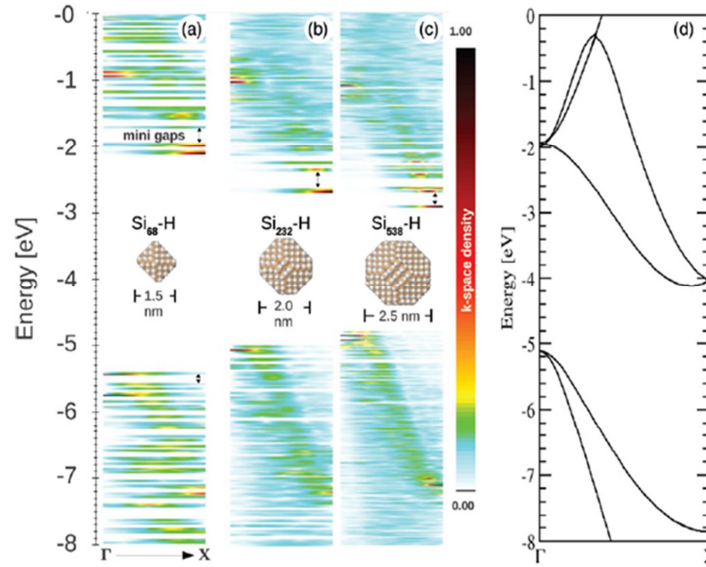


Figure 1.14: Band structure for H-passivated Si NCs of different sizes (a-c). for comparison the band structure of bulk Si is reported [65]

It is clear how for NCs larger than 2 nm [figure 1.14b-c] the dispersion of electronic states near the band edges of VB and CB well mimics that of the bulk (figure 1.14d) while for the smallest NCs (<2 nm) it is difficult to clearly recognize a band structure. Given the similarities between Ge and Si bulk, it is reasonable to assume that the same mechanism holds also for Ge NS having relatively large size. In this case, it would still be possible to speak about an electronic band structure resembling that of bulk Ge and Tauc's hypothesis would be still respected also for this confined system.

At this point, it would be legitimate to consider the electronic band structure in nanostructures similar to that of bulk, and thus Tauc and Cody assumptions can still be considered valid also in confined structures. So, the equations (1.18)-(1.19) provide an interesting way to extract the optical parameters in confined systems.

A lot of efforts in the scientific community have regarded the investigation of the structural and optoelectronic properties of group IV materials (such as Si, Ge, C). While a lot of research exists on Si NS, the Ge NS have often been under-rated because of the lower abundance, higher costs and poor quality of the Ge oxide. However, Ge evidences even better potentiality than Si at the nanoscale. In particular Ge nanostructures gained a renewed interest because of their larger absorption, stronger quantum confinement effect (QCE) due to the larger Bohr radius ($r_B=24$ nm) and lower synthesis temperature in comparison with Si nanostructures. These features bring benefits for what concern the band-gap tuning and the capability to absorb light (in the **appendix 1**, the main properties of Ge are shown). Because of this, Ge NSs could become very attractive as active absorbers for the fabrication of efficient light harvester devices. Up to now, the study of optical absorption properties for Si nanostructures have been extensively investigated while an even more puzzling scenario appears for the optical properties of Ge nanostructures. Thus, a thorough study of the optical properties of Ge NS opens the way for a reliable control of QCE and their exploitation for future nanostructure based devices.

For this reason, a detailed investigation of the light absorption process in Ge NS based films is of essential importance for the knowledge and control of the fundamental physical processes occurring in these systems at the nanoscale.

Chapter 2

Light absorption in Ge QW: methods for experimental data analysis

In this chapter, the main purpose is to establish an effective methodology for the extraction of the optical band-gap in semiconductor NS. In this way, it will be possible to have a deeper understanding of the main mechanisms of light absorption in these confined systems. To this aim we will use Ge QWs, as they join the simplest confining structure (QW) and a semiconductor material (Ge) with large Borh radius (i.e. QCE). Ge QW, with thickness from 4 to 8 nm, were deposited on fused silica substrate by plasma enhanced chemical vapor deposition (PECVD). The light absorption of Ge QWs will be characterized by UV-Vis/NIR spectrophotometry which allow us to extract the R and T spectra. Once the R and T spectra are extracted, two approximated methods (based on double pass (DPA) and single pass (SPA) approximation) will be employed to extract the absorption coefficient spectra. In this chapter, we will try to show pros and cons in terms of complexity and accuracy of each approximated method presented in this work. To do this, we will compare the absorption coefficients extracted through the DPA and SPA models with that extracted through a more accurate method based on generalized transfer matrix method (GTM). Moreover, by comparing the optical band-gaps obtained by Tauc and Cody models (applied to absorption coefficients extracted by DPA and SPA models) with the values extracted through a more accurate parametrization method based on the GTM approach (JTL model), we will be able to understand which of these two approximated models (Tauc or Cody) gives more reliable results about the calculation of the optical band-gap.

2.1 Ge QW: synthesis and experimental data

Thin films of amorphous Ge have been deposited by plasma enhanced chemical vapor deposition (PECVD) on Si wafers or on fused silica quartz kept at 250°C. Top and bottom SiO₂ films (approximately 20 nm thick each one) were used to preserve the Ge QW from the atmosphere oxidation and to isolate it from the substrate, respectively. The schematic in **figure 2.1** shows the structure of our samples. Different thicknesses (from 4 to 8 nm) of Ge films have been obtained by varying the time of the deposition and keeping constant the flux of GeH₄, used as precursor for the growth of Ge film.

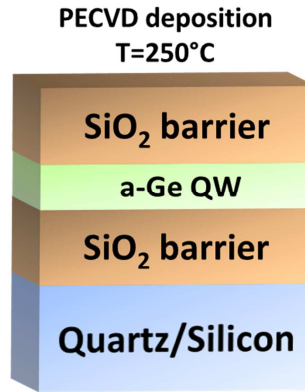


Figure 2.1: Schematic representation of Ge QWs deposited by PECVD at 250°C and embedded by SiO₂ barrier layers

The content of atomic germanium and thickness of the films were evaluated by Rutherford backscattering spectrometry (RBS), using a 2.0 MeV He⁺ beam in glancing detection configuration (backscattering angle of 105°). The glancing detection mode was used to enhance the depth resolution. The RBS analysis was also employed to verify the proper stoichiometry of SiO₂ barrier layers. **Figure 2.2** reports the RBS data in the 1.68 to 1.78 MeV energy range regarding the He⁺ backscattered from Ge atoms. The peak area

is proportional to the Ge dose incorporated in each QW. The Ge content and thickness of each Ge QW were extracted through SIMNRA simulation of experimental data [66]. The extracted Ge dose of our samples ranged from 1.7×10^{16} at/cm² (green area in **figure 2.2**) for the thinnest sample to 3.6×10^{16} at/cm² (red area in **figure 2.2**). Once extracted the Ge dose, by assuming for the deposited material the same density as for monocrystalline Ge, the thickness of samples can be easily estimated as ratio between the so-measured Ge dose and the atomic density of Ge (4.4×10^{22} at/cm³) [63]. The thickness values of Ge QWs obtained in this way were 3.9, 5.5 and 8.2 nm (hereafter named 4, 6 and 8 nm, respectively). The overall error on thickness, including the error on Ge dose, is estimated at 5%.

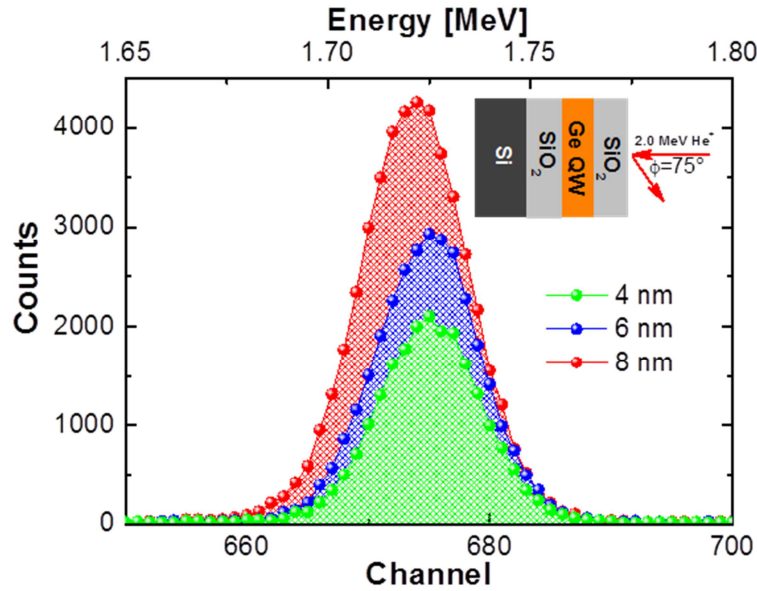


Figure 2.2: RBS spectra of a-Ge QWs. The filled areas are proportional to the Ge content of each QW. The inset in the figure shows the schematic of experimental setup used for RBS measurements.

Once evaluated the structural composition of Ge QW, the light absorption analysis was performed on samples deposited onto fused silica substrates. Transmittance and reflectance spectra were acquired at room temperature using a Varian Cary 500 double beam scanning UV-Vis/NIR spectrophotometer [35]-[38]. In **figure 2.3** the reflectance (R) and transmittance (T) spectra of Ge QWs are displayed as function of incident wavelength, together with the transmittance of quartz substrate (T_Q). The presence of Ge film determines a clear decrease of T in the UV-Vis region with respect to T_Q for all investigated Ge QWs. The decrease of T is not accompanied by an increase of R. In fact, while in the IR region $R+T=1$, in UV-Vis region $T+R<1$ showing that part of incident light is absorbed by the Ge QW.

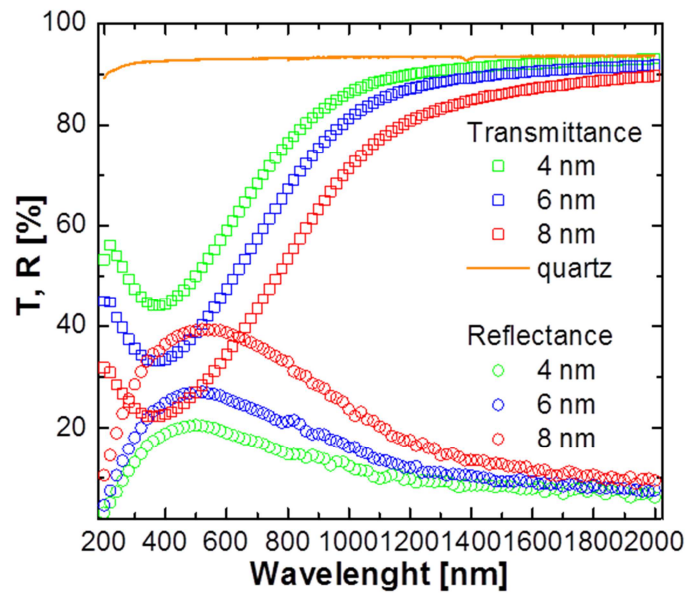


Figure 2.3: Experimental transmittance and reflectance of Ge QWs having different thickness (from 4 to 8 nm). For comparison, The transmittance of the bare quartz substrate is reported.

In the following paragraphs, we will present three different methods to extract the optical bandgap (E_g) of our films, starting from the experimental R-T spectra of our samples and a comparison will be then discussed.

2.2 Methods of E_g extraction: overview

Up to now, a strong debate is underway on how to extract the optical bandgap from experimental R and T spectra. Among different technique, UV-Vis/NIR is certainly the most widely adopted to measure T and R spectra. Basing on these values, two steps are generally followed to extract the optical bandgap of thin films:

- i. Determination of the absorption coefficient α
- ii. Evaluation of the optical bandgap E_g by means of linear extrapolation in Tauc and Cody plots [53]-[55].

For what concerns the first step, some approaches exist, as the single pass one (SPA). Within this model, the incident light beam is assumed to be exponentially absorbed as it propagates through the film, totally neglecting the multiple reflections and interference effects. In particular, in the SPA model even the first reflection at interface between absorbing layer and substrate is neglected, as schematically depicted in **figure 2.4a**. Under this assumption, the transmittance of the film under investigation, following the Beer Lambert law, can be written as:

$$T_S = (1 - R_S) * e^{-\alpha d} \quad (2.1)$$

where d , T_S , R_S , and α are thickness, transmittance, reflectance and absorption coefficient of sample, respectively. Given the equation (2.1), the

absorption coefficient, can be easily extracted by using the following equation:

$$\alpha = \frac{1}{d} \ln \frac{(1 - R_S)}{T_S} \quad (2.2)$$

A more reliable method is certainly the double pass approximation model. In this case the first reflection between the absorbing film and the substrate, as well as the absorption process in the substrate are taken in account, as shown in **figure 2.4b**. In this case, the transmittance of the sample is expressed by the equation (see appendix 2):

$$T_S = T_{sub}(1 - R_S) * e^{-\alpha d} \quad (2.3)$$

where T_{sub} is the transmittance of substrate. So, the absorption coefficient spectra of our film can be calculated by the following expression [38]:

$$\alpha = \frac{1}{d} \ln \frac{T_{sub}(1 - R_S)}{T_S} \quad (2.4)$$

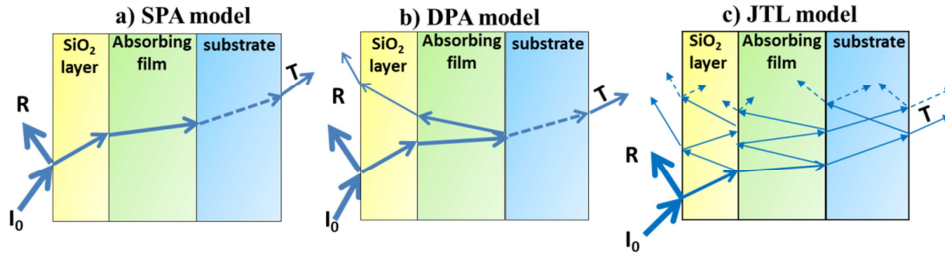


Figure 2.4: Drawing of light paths in SPA (a), DPA (b), and JTL (c) models.

In SPA and DPA models, once the absorption coefficient spectra is calculated, the extraction of optical bandgap comes out through a linear fit of the Tauc and Cody models. As already observed in chapter 1, while the Tauc model is based on the constant momentum matrix approximation, in the Cody model the dipole matrix element is considered as a constant. Recently,

Liu et al. compared these two models (Cody and Tauc) in sputtered Ge QW and showed that the Cody plot can provide a more unambiguous determination of optical bandgap compared to the Tauc one [64]. Actually, since the models use different approximations and the linear fits to extract E_g have been done in different energy ranges (from 0.3 to 2 eV), special care must be taken to compare results from the literature. During this work, we will compare Tauc and Cody models, trying to understand the applicability ranges of both models for amorphous Ge nanostructures. In this way, a complete picture on the use of the two models for the extraction of fundamental optical parameters can be provided. Once the ranges of applicability of Tauc and Cody models are defined, we will be able to understand which of these two models gives more reliable results. The results will be analyzed into detail to get a deeper understanding on light absorption processes in Ge NS.

A more accurate way to extract the optical parameters and thus to better describe the optical properties of various types of materials, e.g. amorphous and crystalline semiconductors, is the fitting of reflectance and transmittance or using the ellipsometry spectra. In particular, R-T spectra are fitted by using the transfer matrix method and a parametrization models. In the past, one of the most popular optical parametrization method was developed by Forouhi and Bloomer (FB model) for amorphous semiconductor and insulators. They obtained an expression for the extinction coefficient k , given by [67]:

$$\alpha(E) = \frac{1}{E} \frac{A(E-E_g)^2}{E^2 - BE + C} \quad (2.5)$$

where A , B , C and E_g are treated as fitting parameters. Clearly the real part of refractive index $n(E)$ was obtained from $k(E)$ using the Kramers and Kronig

integration. Although the FB model fits satisfactory certain materials, in many cases it provides good results only in a very limited spectral range [68] or even produces results without a real physical meaning [69]-[70]-[71]. In particular, although FB formulation appeared to fit several n and k spectra, there are several fundamental problems: a) $k(E) > 0$ for $E < E_g$ (absorption below bandgap), b) $k(E) \rightarrow \text{const}$ for $E \rightarrow \infty$ while both experimental and theoretical results indicate that $k(E) \rightarrow 0$ as $1/E^3$. So, in order to correct the two errors listed above, a new parametrization of the optical functions of amorphous materials was introduced by Jellison and Modine in 1996 [72]-[73]. The JTL model is based on the simulation of the R&T spectra by means of the Generalized Transfer Matrix method (GTM) [74] which takes into account the reflection and transmission at all interfaces (as reported in **figure 2.4c**), and makes use of the spectral complex refractive index the involved materials (film and substrate). The spectral complex refractive index of the unknown film is modeled by means of the Tauc-Lorentz approximation. In this new parametrization model, known as Jellison-Tauc-Lorentz model (JTL model), the imaginary part of the dielectric function (ϵ_2) is determined by combining a single classical Lorentz oscillator with the absorption decay deriving from the Tauc joint density of state. On the basis of this model the imaginary part of dielectric function ϵ_2 is given by the following expression [68]-[71]-[72]-[75]:

$$\begin{cases} \epsilon_2 = \frac{1}{E} \frac{AE_0 C (E - E_g)^2}{(E^2 - E_0^2)^2 + C^2 E^2} & \text{for } E > E_g \\ \epsilon_2 = 0 & \text{for } E < E_g \end{cases} \quad (2.6)$$

where E_g is the band-gap of the material, A is the oscillator amplitude, E_0 is the energy position of the Lorentz peak, and C is the broadening parameter. The real part ε_1 of dielectric function is derived from the expression of ε_2 using the Kramers and Kronig integration, as follows [68]-[71]-[72]-[75]:

$$\varepsilon_1 = \varepsilon_1(\infty) + \frac{2}{\pi} \cdot P \cdot \int_{E_g}^{\infty} \frac{\xi \cdot \varepsilon_2(\xi)}{\xi^2 - E^2} d\xi \quad (2.7)$$

where the P stands for the Cauchy principal part of the integral and an additional fitting parameter $\varepsilon_1(\infty)$ has been included. There are five fitting parameters in this model (E_g , E_0 , A , C and $\varepsilon_1(\infty)$) leading to the (n,k) spectra which are then compared with experimental data through the general transfer method where the sample structure is considered [74]. Iterative fitting cycles are then used to find good agreement among simulated and experimental R and T spectra through minimization. E_g comes out as a fitting parameter of the R and T spectra. In our case the fitting was performed using the GTB-fit computer programme [75], which is based on the Optical code [74]. Both programs are open source and available online [74]. The material under investigation can be inserted in any of the layers, and can also be a component of an effective medium. The code accepts as input the experimental reflectance and transmittance data, sample structure, the five JTL parameters can be changed in order to get n and k spectra which allow us to obtain a good fitting between experimental and simulated R and T spectra. The fitting is based on the χ^2 minimization which was used to test the goodness of fit where a good fit to the data is indicate to $\chi^2 \sim 1$.

In the schematic diagram of **figure 2.5**, we show the three models used to extract the optical bandgap in our work. While in the JTL approach we extract directly the optical bandgap without passing through the absorption

coefficient, in the approximated methods (DPA and SPA approach) we must first calculate the absorption coefficient and then we extract the optical bandgap through the application of Tauc or Cody model.

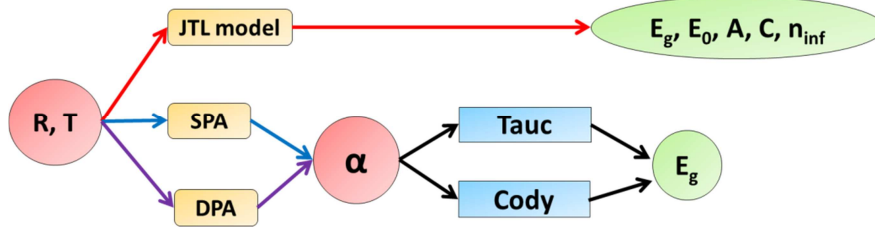


Figure 2.5: Schematic diagram of methods used to extract the optical bandgap E_g of amorphous thin film

In this work, we compare the two approximated method results (based on coupling of SPA or DPA and Cody or Tauc model) with that extracted by JTL methods. In this way, benefits and limits of each approximated methods can be fully understood, providing a more complete scenario for their application about the E_g extraction.

2.3 Determination of optical band gap

2.3.1 JTL approach

Once measured the R-T spectra through the spectrophotometry analysis, the JTL approach was the first analysis used to extract the optical bandgap of our samples. To launch the inversion software GTB-fit [75], the structure “SiO₂ (20 nm) / unknown film / SiO₂ substrate” was used. The interfacial SiO₂ layer is neglected, as it is optical indistinguishable from the substrate. For the unknown films, the thickness was fixed at the value determined as described in Section 3.1. The optical constants of the SiO₂ layer and

substrate were taken from ref. [76]. In order to set the initial values of the five JTL parameters, we started our analysis with a reference bulk Ge sample. In this case, given the absence of a cap layer, the structure “unknown film/ SiO₂ substrate” was inserted. This sample has a thickness of 120 nm so that QCE can be truly considered absent. As reported in **figure 2.6d**, a very good matching between the experimental and computed R-T spectra is achieved. It is also worth emphasizing that relative variation of 2-3% in the values of A , E_g , E_0 and C does not significantly worsen the relative fit ensuring a well lower than 1.

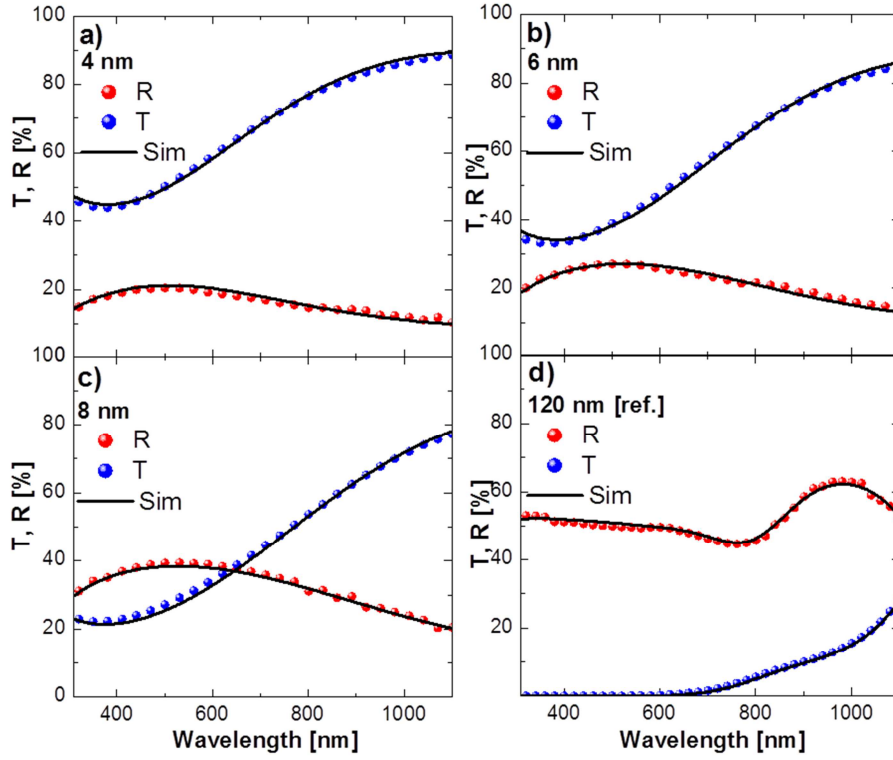


Figure 2.6: Experimental (symbols) and computed (black lines) T and R spectra of a-Ge QW with different thickness (a-c). For comparison, the experimental and computed R-T spectra of a reference sample (120 nm Ge film) are reported.

The parameters values providing the best fit are reported in table 2.1.

JTL parameters

Sample	E_g [eV]	E_0 [eV]	A	C [eV]	n_{inf}	χ^2
4 nm	1.14	2.8	206	4.10	1.3	0.89
6 nm	1.05	2.8	201	3.96	1.3	0.59
8 nm	0.98	2.9	185	3.79	1.3	0.79
120 nm	0.88	2.6	175	3.34	1.3	0.32

Table 2.1: The five JTL fit parameters and the values of χ^2 test are reported

The real and imaginary part of the refractive index for the amorphous bulk Ge sample, obtained by using the JTL parameters, are reported in **figure 2.7**. The maximum of n was peaked at 2.6 eV, a value which is near to the lower direct transition energy of c-Ge (~ 2.5 eV) [77]. For what concerns the Ge QWs simulations, we set the five JTL parameters to initial values found in reference Ge sample. Then, through iterative cycles, one parameter at time was left free to vary, then two parameters and so on, iteratively up to find the best agreement between the experimental and computed R-T spectra, as shown in **figure 2.6 (a-c)**. For all samples, the set of the best parameters is reported in the table 2.1. As shown in table 2.1, the optical bandgap E_g increases as the thickness of Ge QW is reduced. This effect is related to QCE, in agreement with what observed in literature [63]. Another effect attributable to QCE can be observed in our simulation parameters as the increase broadening parameter (C) and oscillator amplitude (A) of Lorentz oscillator with the reduction of the QW thickness. This reflects the fact that as the QW thickness is reduced the area under the Lorentz oscillator peak in the ϵ_2 function changes (**figure 5a**), as if the QCE modifies the interaction

between the incoming electromagnetic field and the confined electrons. This evidence is in agreement with what previously observed for Ge QWs [63]. The broadening of oscillator peak can also be linked to a larger roughness of the QW as it shrinks. The **Figure 2.7** reports the n - k spectra obtained within the JTL model. As can be seen from these spectra, the QCE induced a clear blue-shift of k spectra, linked to the bandgaps widening and a slight modification of n which indicates how the propagation of the electromagnetic field changes in confined Ge QW.

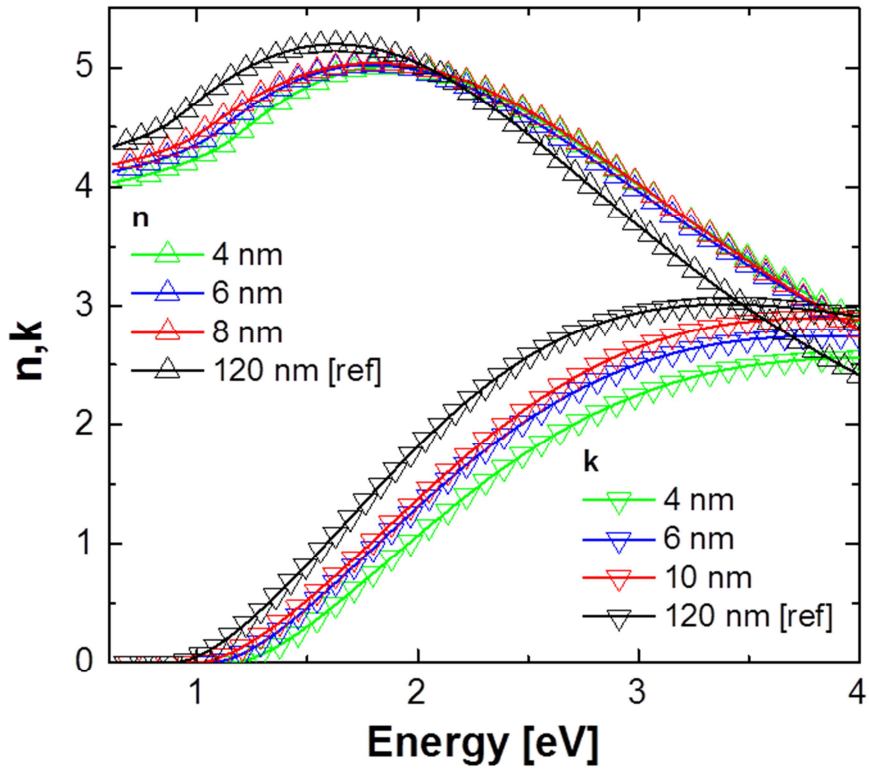


Figure 2.7: n and k spectra of Ge QWs (thick 4, 6 and 10 nm) and reference Ge sample (120 nm thick Ge film) obtained by iterative fitting within JTL model.

2.3.2 DPA approach

In this sub-paragraph, we show the results achieved by applying the DPA model. First of all, the absorption coefficient spectra of our samples were obtained by substituting the R and T spectra, measured by spectrophotometry, in the **equation 2.4**. The so-obtained α spectra of a-Ge QWs and of a reference sample are reported in **figure 2.8**. The saturation of α at higher energy than 3.4 eV in the reference sample is an artifact due to the sensitivity limit of our experimental setup. The most evident effect in **figure 2.8** is the blue-shift occurring close to the onset of the absorption spectra by decreasing the thickness of the Ge film from 120 nm to 4 nm. This evidence can be thought as an effect of quantum confinement which induces a decrease of the optical bandgap of our materials. Moreover, in the range from 1.8 eV to 2.5 eV, the intensity of absorption coefficient in Ge QW exceeds that of 120 nm Ge film indicating an enhanced interaction of electromagnetic field with confined carriers. This result is in contrast with the decrease of k with thickness observed in the fitting results (figure 2.7) and is to put in relation with the increasing error for thinner films deriving from the approximation. In fact, for thinner film, less light is absorbed in each pass and thus the multiple reflections, negligible in the DPA approach, play an increasingly important role on the absorption process.

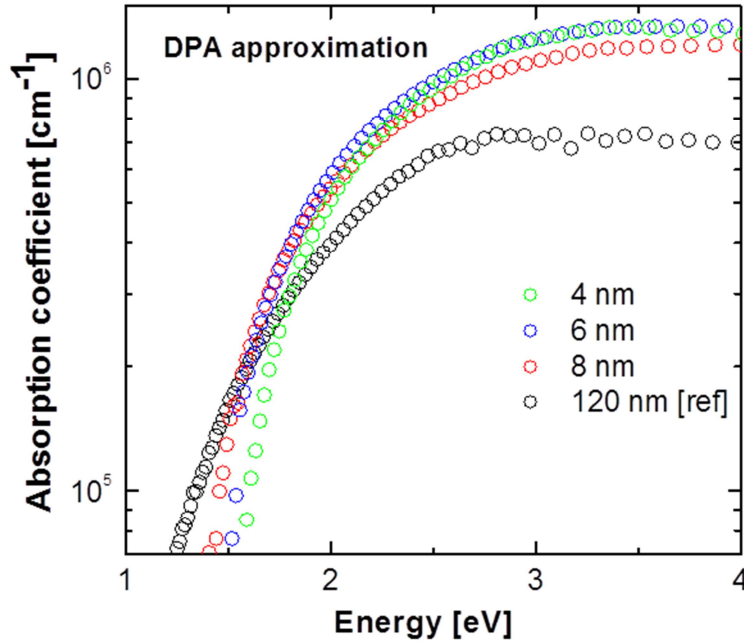


Figure 2.8: Absorption spectra of a-Ge QWs and of a reference sample extracted by using DPA approach.

As already explained in the paragraph 2.2 of this chapter, once the α spectra is calculated, the optical bandgap is extracted by linear fitting performed on Tauc and Cody plots. In **figure 2.9**, the Tauc plots of all Ge QWs and reference sample and the table with the extracted values of optical bandgaps are reported. The linear fit of Tauc plot were performed in an energy range determined by the empirical rule which only considers data points with energy values such that the condition for $\alpha > 10^4 \text{ cm}^{-1}$ is satisfied [53]. In agreement with the prediction from QCE, in the Tauc plot we observe an increase of the optical bandgap as Ge film thickness is reduced. In fact, the optical bandgap value increases from 0.88 eV for a reference bulk sample

(120 nm thick) up to a value of 1.12 eV for the thinnest film (4 nm thick of Ge QW).

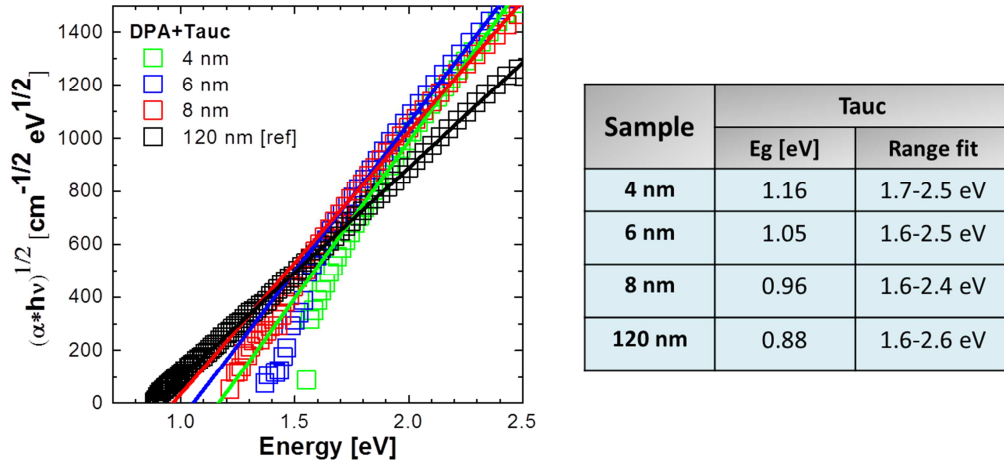


Figure 2.9: Tauc plot and corresponding linear fit derived from data in figure 2.8. In the table the extracted bandgaps and energy ranges for the linear fit to Tauc plot are reported

At the same time, a linear fit of the Cody plot was performed, as reported in **figure 2.10**. Given the very thin film used, the rule of $3 < \alpha l < 10$ cannot be applied for the Cody plot [78]. Also in this case, the optical bandgap values increase with the reduction of film thickness, going from 0.76 eV of thickest sample to 1.27 eV of thinnest one. It should be noted that by applying the Cody plot, one gets a stronger variation of E_g with QW thickness in comparison to the Tauc approach.

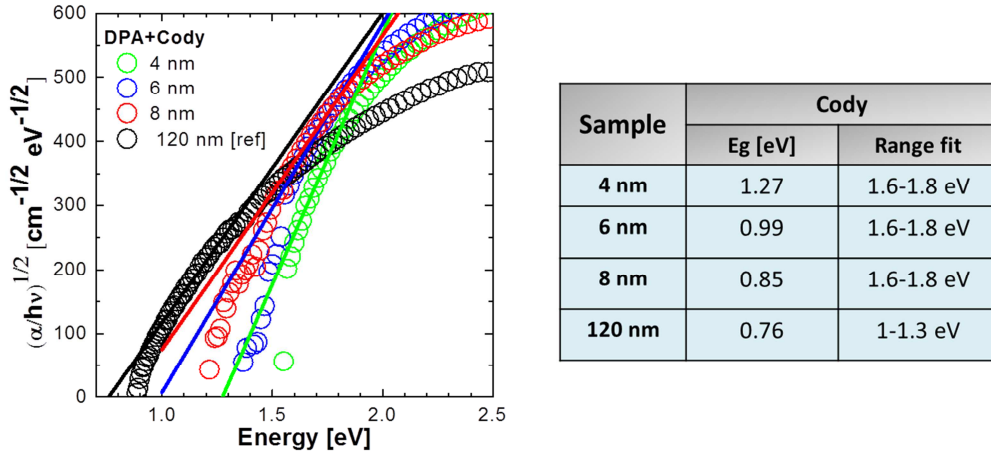


Figure 2.10: Cody plot and corresponding linear fit derived from data in figure 2.8. In the table the extracted bandgaps and energy ranges for the linear fit to Cody plot are reported

For the Tauc plot the linear region extends over a wider spectral range with respect to Cody plot, allowing to perform the linear fits to Tauc plot (1.6 eV-2.5 eV) in a much wider energy range than to Cody plot (1.6 eV-1.8 eV). This behavior of Tauc has been already observed in other works, leading to wider preference of Tauc plot over the scientific community [75]. However, choosing the right range of validity of both models is a major challenge.

2.3.3 SPA approach

In this paragraph, the results achieved by using the SPA approach are discussed. The α spectra of all Ge QWs and of reference a-Ge bulk film, obtained by substituting the R and T spectra in **equation 2.3**, are reported in **figure 2.11**. As already observed for the DPA approach, the absorption onset suffers a slight blue-shift with the reduction of Ge film thickness attributable to QCE.

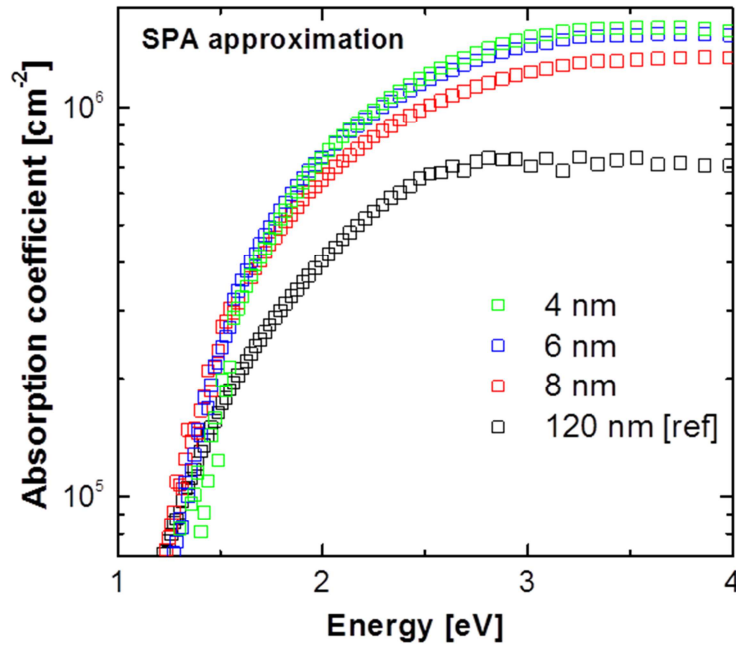


Figure 2.11: Absorption spectra of a-Ge QWs and of a reference sample extracted by using SPA approach.

In order to extract the optical bandgap E_g , Tauc and Cody plot are used, as shown in **figures (2.12)-(2.13)**. The same criteria reported in DPA section for linear fitting procedures were used here. The extracted values of E_g , reported in tables in **figure (2.12)-(2.13)**, show the expected increase with the reduction of Ge film thickness for the Tauc and Cody plots. As for the DPA approach, also in the SPA approach the use of Cody plot leads to a larger variation of E_g with QW thickness with respect to Tauc plot. Moreover, as already noted for the DPA approach, the linear region of Tauc plot is well wider than the Cody, demonstrating the superiority of the Tauc approach over the Cody one.

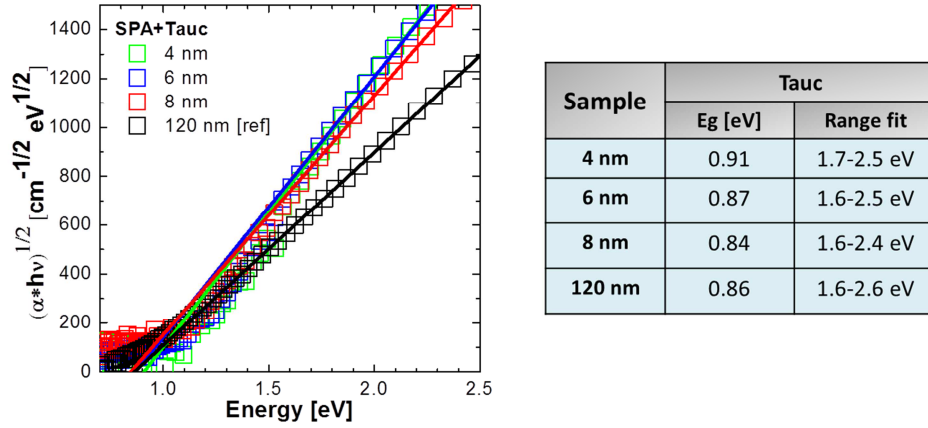


Figure 2.12: Tauc plot and corresponding linear fit derived from data in figure 2.12. In the table the extracted bandgaps and energy ranges for the linear fit to Tauc plot are reported.

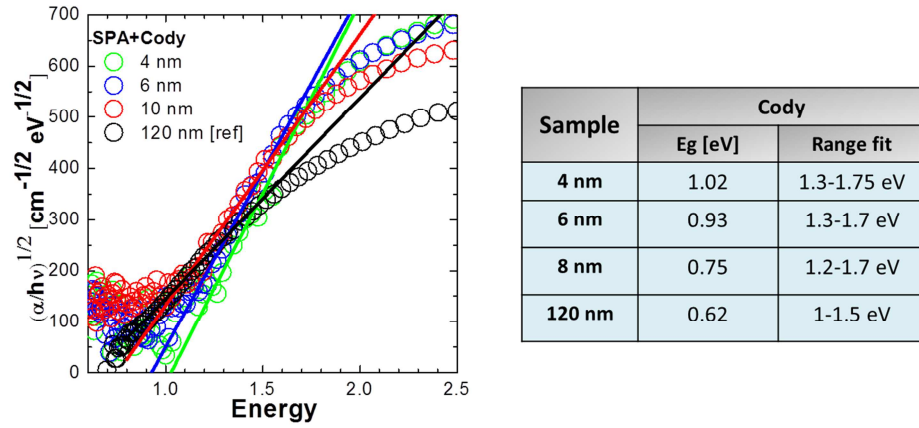


Figure 2.13: Cody plot and corresponding linear fit derived from data in figure 2.12. In the table the extracted bandgaps and energy ranges for the linear fit to Cody plot are reported.

2.3.4 Models comparison

In this section, the results of three methods are compared and discussed in order to understand limits and merits of each one. We start our investigation by comparing the absorption coefficient spectra extracted with the three different methods: SPA,

DPA and GTM approach (figure 2.14) for all samples under investigation. As already indicated in the paragraph 2.2, the GTM is the approach used to simulate the R and T spectra of samples (once fixed the n-k spectra) and to extract the α spectra within the JTL method. In figure 2.14, it is clear that in both approximated approaches the absorption coefficient is overestimated, especially for energy close to the absorption onset.

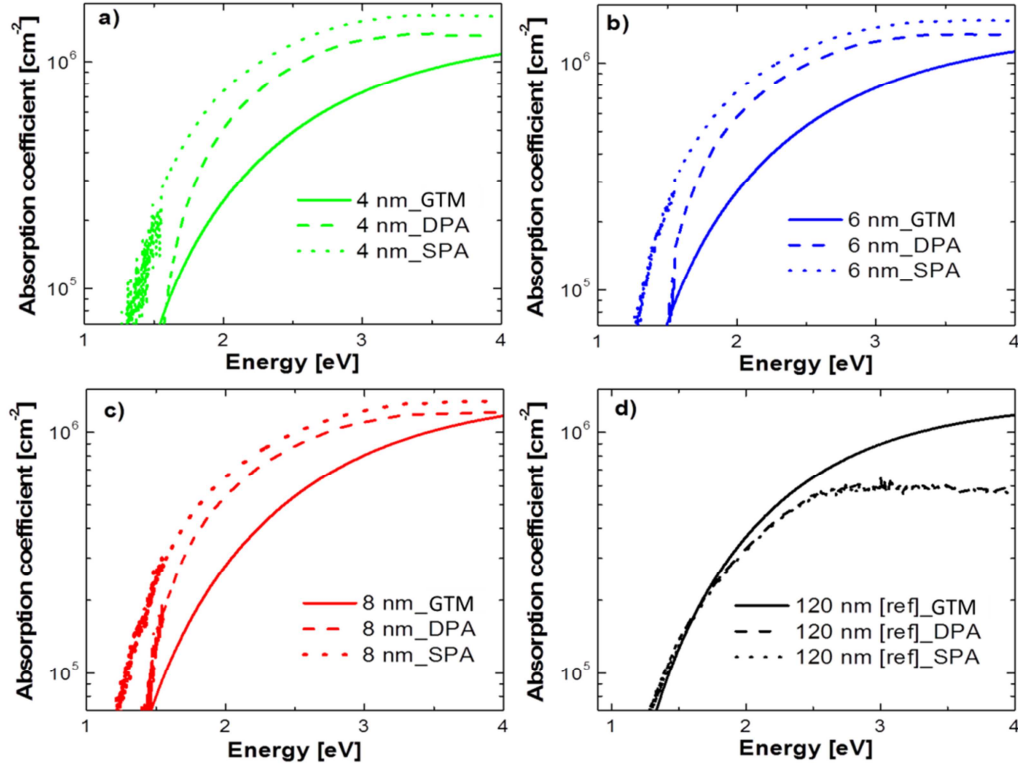


Figure 2.14: The absorption coefficient spectra of all Ge QWs (a-c) and reference sample (d) extracted with three different methods: JTL (solid line), DPA (dashed line) and SPA (dotted line)

This overestimation of α is due to the fact that the multiple reflections and interference effects are neglected, even of different extent, in approximated methods, especially for the SPA approach where the discrepancy is higher with respect to DPA approach. This evidence is due to the fact that in SPA approach the first reflection at interface between film and substrate is neglected. Moreover, as can be observed in figure **2.14(a-d)**, such discrepancy increases when Ge QW thickness is decreased. In fact, for thinner film, less light is absorbed in each pass and thus the multiple reflections play an increasingly important role on the absorption process. On the contrary, when the film is enough thick (as 120 nm Ge film), only a small fraction of the electromagnetic radiation reaches the film/substrate interface, reducing the interference and multiple reflection contributions on light absorption process. For this reason, no significant discrepancy between approximated method (DPA and SPA) and the GTM approach can be observed for the relative thick film (especially for the thickest Ge film reported in figure (**2.14d**)).

It is important to note that no significant differences were also found between three methods at high photon energy (**2.14a-c**). In particular, the high absorption coefficient of samples at high energy leads to a strong absorption in the first few nanometers of the film, not allowing the beam to reach the film/substrate interface. Also in this case, therefore, the interference and multiple reflection effects do not play a primary role in the absorption process, as demonstrated by similar absorption coefficient values at high energy extracted through the approximated approaches (DPA and SPA) and the non-approximated one (GTM).

Once noted such discrepancy of α depending on the used approach, thickness of samples and photon energy, we try to understand if such discrepancies

strongly influences the determination of the optical bandgap, especially in the case of very thin samples. For this reason, in **figure 2.15 (a-b)** the optical bandgaps extracted by JTL model (based on GTM and Tauc models) and approximated approaches by using the Tauc and Cody plots are reported. First of all, as reported in figure 2.16a, the JTL and DPA+Tauc methods give the same results, with a slight variation appearing when Ge QW thickness goes below 4 nm (<2%). Therefore, despite the significant mismatch of α spectra between JTL and DPA approaches (**figure 2.15**), the optical bandgap values extracted by both models are fairly converging. This demonstrates that DPA+Tauc approach can be successfully used for the extraction of optical bandgaps in a-Ge QW.

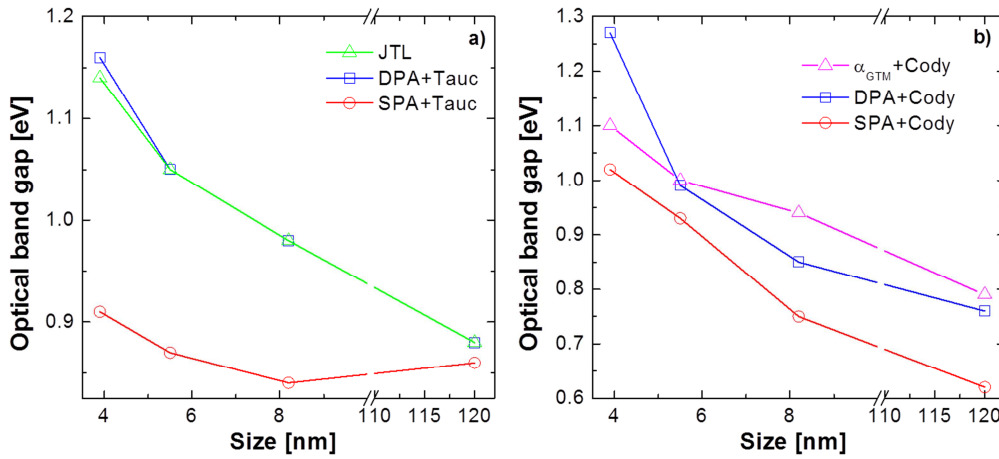


Figure 2.15: Optical bandgaps extracted within JTL model, and ones extracted combining the approximated model (DPA or SPA) and Tauc (a) or Cody (b) plot

A further confirmation of the reliability of DPA+Tauc approach is reported in **Figure 2.16** where the effect of quantum confinement on the optical bandgap of a-Ge QWs, extracted through DPA+Tauc model is reported. To ascertain if such a large size dependent blue-shift is well described by

quantum confinement of carriers, E_g data have been fitted (solid line) within the effective mass theory, assuming an infinite barrier, by equation $E_g = E_g^{bulk} + A/D^2$. In our case, A is the only fitting parameter, while E_g^{bulk} was fixed as the bandgap of bulk a-Ge (0.88 eV). The good fit agreement with experimental data confirms that the shift in the energy gap is ascribed to QCE and that SiO₂ layers act as infinite potential barrier, ensuring a strong confinement of electrical carriers within Ge QWs. Moreover, the experimental confinement parameter in a-Ge QWs results to be 4.42 eV·nm², which value is very close to 4.35 eV x nm², obtained for a-Ge QWs grown by sputter [63]. Furthermore, the experimental confinement parameter in a-Ge QWs resulted to be about double of the theoretical value of 1.97 eV·nm² reported by Barbagiovanni et al. for a strong quantum confinement in crystalline Ge QW [32]. As outlined in chapter 1, A is given by $A = \pi^2 \hbar^2 / 2m^*$, where m^* is the reduced effective mass of excitons, expected to be approximately $0.1 \times m_e$ in Ge (m_e is the free electron mass). The reason of the difference between our experimental value for a-Ge QW and the calculated one for c-Ge QW can be attributed, at first approximation, to the reduced effective mass of carriers in amorphous NS. This hypothesis agrees also with the experimental observations made by Robner et al. [79] on the effective masses of Ge/SiGe multi-QW (MQW). Therefore, as the result of the larger value of A , an increased confinement of carriers and a stronger shift of the optical bandgap is expected in amorphous NS than in crystalline ones.

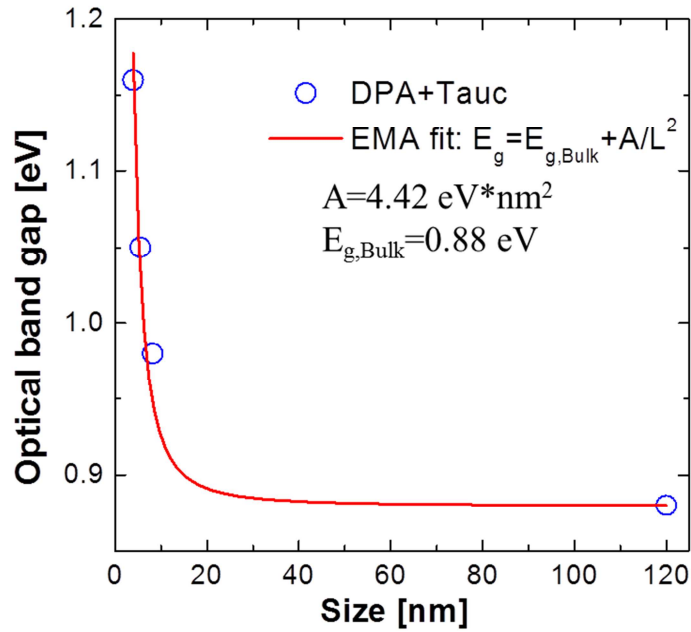


Figure 2.16: Experimental values (circle points) of energy gap in a-Ge QW (extracted by DPA+Tauc approach) versus thickness, fitted through effective mass theory formula of QC (solid line).

The results are different for the SPA model. In fact, SPA+Tauc approach gives much lower E_g values without any clear change with thickness reduction, as observed in **figure 2.15a**. It seems clear that the DPA coupled with Tauc model gives much more reliable results with respect to the use of SPA+Tauc approach.

With regards to results obtained through the Cody model, the situation appears to be more complicated than that found by Tauc model. In order to assess the reliability of approximated methods (SPA and DPA) and the application of Cody model to these latter, we decided to compare the E_g values extracted by approximated methods coupled with Cody plot (DPA+Cody and SPA+Cody) with the values extracted applying the Cody

plot to absorption coefficient spectra extracted through GTM approach (using the n-k spectra extracted within the JTL model through fitting of the R and T spectra of Ge films). The results of this comparison are shown in **figure 2.15b**. In particular, applying the Cody plot to the approximated methods (SPA and DPA) the extracted optical bandgap (E_g) did not result in some convergence with the values extracted within the GTM approach. Particularly interesting is the fact that the Cody plot gives lower values compared to those extracted by Tauc plot. Moreover, the reference sample analyzed with the Cody plot gives E_g lower than 0.8 eV. This result is dissimilar to what calculated by theoretical and experimental measures on a-Ge whose value is around 0.8 eV [53].

The different E_g values, obtained applying approximated methods coupled with Tauc and Cody plots, suggest that some care should be taken as the energy range for fitting is considered. For this purpose, the **figure 2.17** reports, as example, the ε_2 spectrum for 8 nm Ge QW as extracted by JTL model. In this graph, three different regions of application as function of the energy are reported, for the three discussed methods so far. The first range is the Cody model application region which spans from 1.3 eV to 1.8 eV (red arrow in **figure 2.17**). In fact, for energy values greater than 1.8 eV the loss of linearity in the Cody plot can be observed (**figure 2.10**). For the Tauc plot a wider linear region with respect to Cody plot is visible. In particular the energy range in the Tauc plot (blue arrow in **figure 2.17**) extends from 1.8 eV to 2.5 eV. This evidence, observed in Tauc plot, ensures a lower uncertainty in the determination of E_g through the linear fit. Finally, the last and wider application range is that of JTL model (green arrow in **figure 2.17**) which spreads from 1 eV to 4 eV. This region represents the full energy range in which R and T spectra have been successfully fitted.

The JTL approach is clearly the most powerful one, not only because it is able to fit the experimental optical data in the full energy range but also because it does not use any approximation on the R and T data to extract the optical bandgap. Moreover, both Tauc and Cody plots show instead a limited energy range where the linear fit can be performed, focusing on the light absorption close to the bandgap energy region. Still, Tauc approach is able to fit the approximated α over a larger range than the Cody approach, leading to smaller uncertainty in the E_g determination. Finally, Tauc model applied to α extracted through the DPA exhibited the best performance when compared to the JTL non approximated method. This is due to the larger range of linear fit of Tauc over Cody plot and the lower degree of approximation of DPA method in extraction α from experimental data.

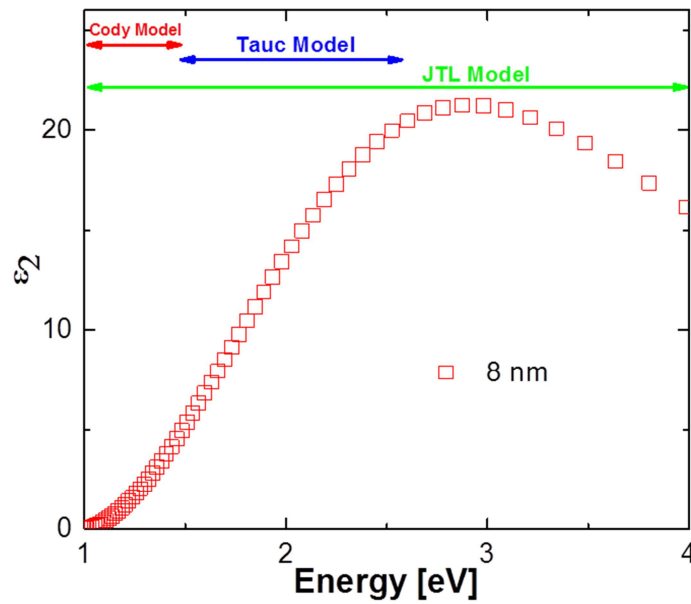


Figure 2.17: ϵ_2 spectra of 8 nm Ge QW. The figure shows three regions of applicability of Cody (red arrow), Tauc (blue arrow) , and JTL (green arrow) models.

2.4 Conclusions

In this chapter, we provided a general overview of three methods used to extract the optical parameters from R and T spectra of Ge QW. This may help to better understand the light absorption process in confined semiconductor nanostructures. Moreover, we gave arguments that the Tauc model, commonly used to describe the absorption of bulk amorphous semiconductor, is valid also for amorphous NS. To this purpose, three analytical methods have been compared to evaluate their degree of accuracy and complexity. To evaluate this point experimentally, we deposited single amorphous Ge ultrathin (2- to 120-nm thick) films embedded in SiO₂ barrier layers. These confined structures were grown by PECVD at room temperature. First of all, two approximated methods (based on double pass, DPA, or single pass, SPA, approximation) were employed to extract α from R and T spectra, and Tauc or Cody plots were then used to evaluate E_g by linear fitting. A third method, based on the Tauc Lorentz oscillator model (JTL model) was used as a comparison. In the JTL model, the E_g was estimated by direct fitting of R-T spectra by means of complex refractive index building. Both the approximated methods overestimate the absorption coefficient spectra with respect to ones extracted by the non-approximated method. This can strongly influence the extraction of optical bandgap through the Tauc or Cody plot. The optical band gap values obtained by combining the DPA and Tauc plot are fully converging with the values of E_g obtained by non-approximated method (JTL model) for Ge QWs. This evidence shows that the DPA coupled with the Tauc model is a reliable and easy method to extract E_g from R and T spectra. On the contrary, the overestimation of α leads to, as a consequence, a systematic underestimation

of E_g . On the other hand, the Tauc plot always shows a much wider range of linearity in comparison with Cody plot, leading to a better evaluation of E_g . The superiority of the Tauc approach over the Cody leads to conclude that the Tauc model can successfully be used to describe the light absorption process also in confined nanostructures. Therefore, the Tauc model represents a powerful approach to extract the optical bandgap of these systems. The reported methods have been largely used in literature to evaluate E_g in semiconductor nanostructures and the present comparison on Ge QWs shows limits and benefit of each, for their better use.

Chapter 3

Light absorption in Ge QDs randomly distributed in SiO₂

In this chapter, we focus on the interface of Ge QDs randomly distributed in SiO₂ and their interplay in the confinement effects occurring in the light absorption process. Quantum confinement (QC) typically assumes a sharp interface between a nanostructure and its environment, leading to an abrupt change in the potential for confined electrons and holes. When the interface is not ideally sharp and clean, significant deviations from the QC rules appear and other parameters beyond the nanostructure size play a considerable role. Through a detailed electron energy loss spectroscopy (EELS) during Transmission Electron Microscopy (TEM) analysis, we investigated the structural and chemical properties of Ge QD interfaces, by comparing Ge QDs grown by PECVD and sputter techniques. We demonstrate that a different interface can largely modify the size-dependent tuning of the bandgap and oscillator strength. We explain our results through the SPDEM-modified EMA model. These findings shed new light on the role of a QD–matrix interface, which in essence reveals its key role in building the confinement potential for excitons. The results of this study provide a new understanding of the role of interfaces on the quantum confinement effects in nanostructures. Moreover, our results indicate a further direction for an optimized exploitation of confinement effects in future nanostructure-based devices: not only by exploiting size effects, but also taking advantage of interface engineering.

3.1 Introduction

In chapter 1 we have already observed that one of the most interesting features in nanostructures is the quantum confinement effect (QCE), arising for dimensions smaller than the exciton Bohr radius (5 nm for Si, 24 nm for Ge [31]. In particular, QCE is expected to increase the optical bandgap and the oscillator strength with respect to the bulk values, allowing to tailor the light absorption spectrum and intensity [80]. However, the optical behavior and the band-gap of NSs does not only depend on their size, as a basic confinement effect rule predicts. Other effects have been demonstrated to have a strong role in the light absorption/emission process such as: nanostructure shape [37], the QD crystalline structure [38]-[39], or the potential barriers surrounding the QD [40]-[41]. These factors can hinder the QCE, not allowing to take full advantage of absorption modulation and enhancement in the nanostructures. In particular, as already indicated in chapter 1, a growing interest has been recently focused on the role of QD/matrix interface [57]-[59]-[60]. Thus, in order to have a reliable control of QC in semiconductor QDs, it is necessary to have a deeper investigation of the interface, in terms of bonds, stoichiometry and defects, and it is essential to disentangle the role of the size from the interface effects, if any, and identify the extent of each contribution.

To this purpose, in the following paragraphs we will investigate the role of the interfaces on the light absorption process of Ge QDs embedded in SiO₂ matrix. To do this, we present an exhaustive comparison of Ge/matrix interfaces for QDs synthesized by sputtering or by PECVD techniques. We demonstrate that the differences between sputter and PECVD grown QDs can largely influence the size-dependent tuning of the bandgap and oscillator

strength and we explain our results through a modified effective mass approximation (EMA) model.

3.2 Synthesis and structural properties of Ge QDs

In this experiment, as reported in **figure 3.1**, Ge rich SiO₂ thin films (hereafter named SiGeO) have been deposited by PECVD on fused silica quartz or p-type Si substrates kept at 250°C. Different Ge concentrations have been obtained by varying the flux of GeH₄ (going from 60 to 120 sccm) while the fluxes of SiH₄ and N₂O gases was kept constant. Each of these gases were used as precursors for the growth of SiGeO films. After the deposition, samples underwent thermal annealing at 800°C in N₂ atmosphere for 1h. During thermal annealing, Ge QDs undergo an Ostwald ripening mechanism, similar to the Si QD case [81], leading to a size increasing of precipitates

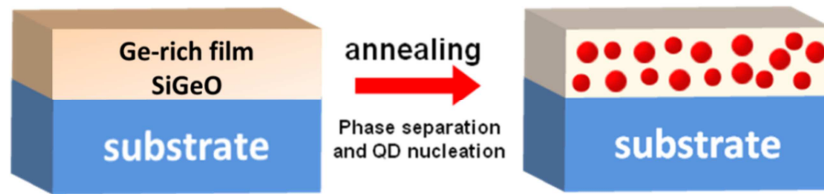


Figure 3.1: Schematic representation of Ge QD synthesis from annealing of Ge-rich films deposited by PECVD method.

The elemental composition of SiGeO films (as deposited or after thermal annealing) was determined by Rutherford backscattering spectrometry (RBS), using a 2.0 MeV He⁺ beam in random configuration and with a backscattered angle of 165°C. **Figure 3.2** shows a typical RBS spectrum of our SiGeO films deposited on silicon substrate. Arrows in **figure 3.2** indicate

the signals due to He⁺ ions backscattered by surface atoms of Si (1150 keV), Ge (1600 keV) and O (750 keV) in the SiGeO film. All samples exhibit an homogeneous depth distribution of Ge atoms. RBS spectra have been simulated using SIMNRA software to determine the Si, Ge, and O content and the stoichiometry of each film. Small amounts of nitrogen (~5%) have been found in as deposited SiGeO samples (due to the use of N₂O gas as precursor of O).

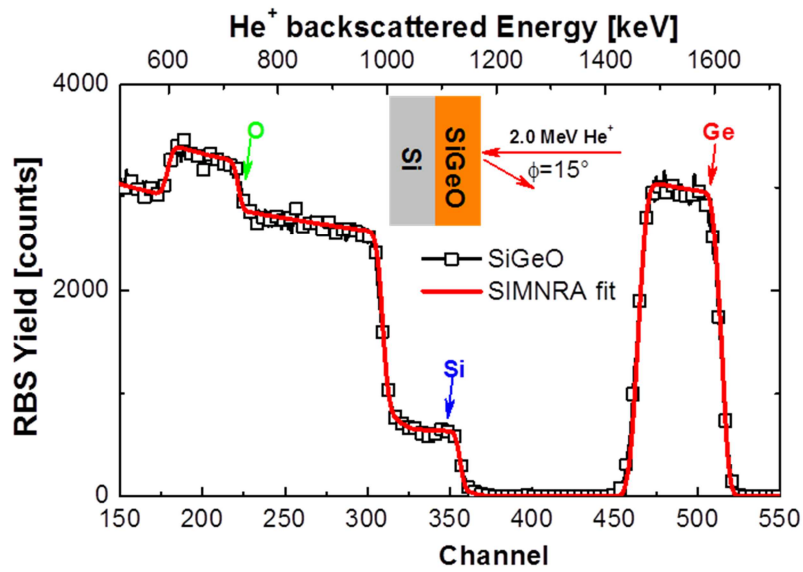


Figure 3.2: RBS spectrum and SIMNRA fitting of a representative SiGeO film deposited by PECVD on Si substrate. The experimental RBS setup is drawn in the figure.

Table 3.1 summarizes the values of thickness (from TEM) and Ge content (from RBS) of as deposited and SiGeO films annealed at 800°C. In the **table 3.1** the value of GeH₄ flux (in sccm) was used as a suffix number to name the different samples. The Ge content in the as deposited films increases

with the increasing of GeH₄ flux, going from 8% to 16%. while the film thickness is around 400 nm for all samples. As a result of the thermal annealing, part of the Ge atoms out-diffuse from the sample surface as volatile Ge-O compounds, as already reported in literature [82]-[83]. In our case, such an out-diffusion leads to a substantial thickness reduction (~100 nm). Moreover, the Ge content in the annealed samples increases from 10% to 17.5% with the GeH₄ flux, slightly increasing with respect to the corresponding values of as deposited films (which values span from 8% to 16%). This densification of film is also related to the preferential evaporation of N and H related species as result of the thermal annealing.

Samples	GeH ₄ flux [sccm]	Thickness [nm]		% Ge	
		As deposited	800°C	As deposited	800°C
SiGeO60	60	430	330	8	10
SiGeO90	90	365	280	12	15
SiGeO120	120	410	310	16	17.5

Table 3.1: Film thickness (extracted by TEM) and Ge content (extracted by RBS), before and after 800°C annealing, for SiGeO film deposited by PECVD

The presence and size distribution of Ge QDs, as well as the film thickness, were evaluated by cross sectional Transmission Electron Microscopy (TEM) analysis. For what concerns Ge QDs, we recognized them according to the degree of overlap between QDs either by automatic particle identification software or manually by locating their boundaries. In the case of automatic identification, the particles are automatically recognized by standard computer processing, taking into account their optical contrast in the gray scale. In the case of overlapping particles, this method does not produce

good results, therefore a manual recognition of the QDs was required. For each sample, about one hundred particles were analyzed. For each set of data, we finally calculated the average size and the standard deviation. TEM analyses have been performed on all samples, allowing to report the QD size versus Ge content trend, as shown in **figure 3.3**. Ge QDs in SiGeO films exhibit a mean size growing from about 3.5 ± 1 nm to 8.5 ± 2 nm with increasing the Ge concentration from 0.7×10^{22} at/cm³ (~8% Ge) to 1.3×10^{22} at/cm³ (~16% Ge). TEM image in the inset in **figure 3.3** (referred to the sample with the highest Ge concentration, ~16%) reveals the presence of Ge QDs as bright spots (high Z-contrast of QDs with respect to the SiO₂ matrix).

Once the mean size was evaluated for all samples, the packaging of QDs was investigated. In particular, we can give a rough estimation of the average QD concentration by considering the atomic Ge content (D) measured by RBS and the QD mean size ($2r$) extracted by TEM analysis, under the assumptions that after thermal annealing all the Ge in excess in the alloy is involved in the nucleation of spherical QDs and the atomic density (ρ_{Ge}) of QDs is equal to the bulk value. In this case, the number of Ge atoms in a spherical QD having size $2r$ is $N_{Ge} = (4/3)\pi r^3$, while the concentration of Ge QDs within a layer of thickness t_f is simply: $C_{QDs} = \frac{D}{N_{Ge} t_f}$. Assuming a random distribution of QDs within the layer, the mean surface-to-surface QD distance (S_2S) can be estimated as:

$$S_2S = \frac{1}{\sqrt[3]{C_{QD}}} - 2r \quad (3.1)$$

In our samples, QDs concentration ranges from 2.5×10^{18} QD/cm³, for the sample with 10% Ge, to a value of 3×10^{17} QD/cm³, for the sample having

17.5% Ge, as reported in **figure 3.3**. The corresponding values of S_2S calculated by the equation 3.1 ranges from 4 nm to 7 nm. The so-estimated Ge QD density and S_2S should be taken as upper values, since in CVD methods incomplete precipitation of excess Ge cannot be ruled out [84].

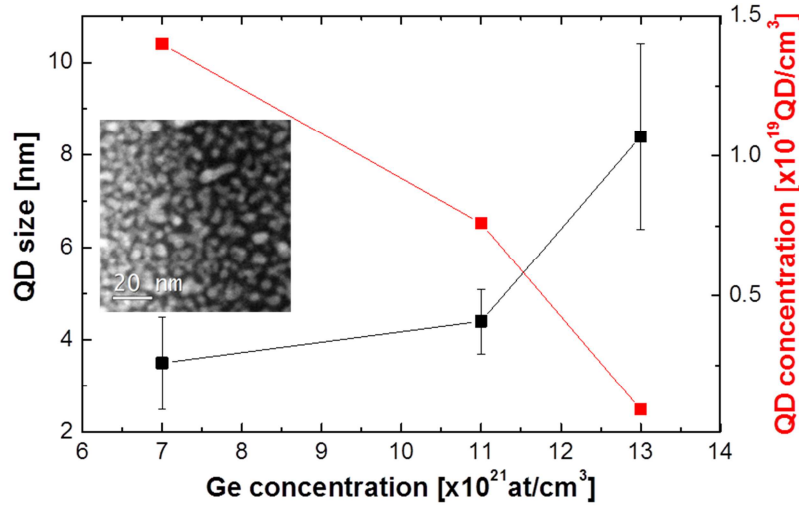


Figure 3.3: Mean QD size (black symbols) and QD concentration (red symbols) as a function of the Ge atomic concentration in SiGeO films annealed at 800°C. The inset shows a representative TEM images of Ge QDs in the SiGeO120 sample.

It is well known that thermal annealing also induces a concomitant transition from the amorphous to the crystalline phase of Ge QDs.[ChoiJAP99] In order to evaluate the extent of such transition for our samples, we performed Raman analysis on samples annealed and as deposited. The **figure 3.4** reports the Raman spectra of SiGeO90 sample before and after thermal annealing at 800°C. The broad band in the 240-290 cm⁻¹ range of the as deposited film corresponds to the convolution of the TO and LO phonon modes in amorphous (a-) Ge [86]. After thermal annealing at 800°C, the appearance of a narrow peak centered at around 300 cm⁻¹ (TO phonon mode in crystalline (c-)

Ge [86]) reveals partial transition to the crystalline phase of Ge in QDs. However, a substantial fraction of Ge QDs is still in the amorphous phase, as suggested by the presence of the broad shoulder at 280 cm⁻¹. Therefore, Raman analysis confirmed that most QDs remain amorphous.

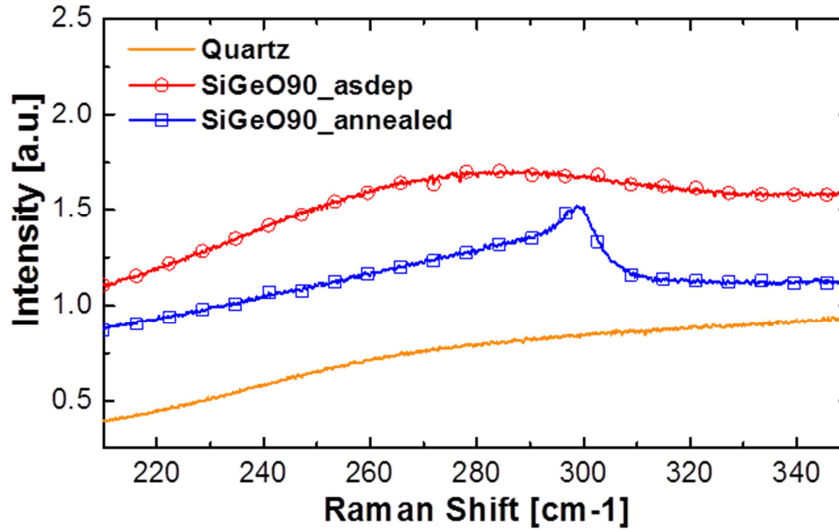


Figure 3.4: Raman spectra of as deposited SiGeO (red symbols+line) and evolution after thermal annealing at 800°C (red symbols+line). The spectra of the fused silica substrate are reported for comparison (orange line), Raman spectra of all samples are vertically offset for clarity. [35]

The Ge QDs were also synthesized by sputter technique. In order to do a suitable comparison between the two synthesis techniques, the sputter samples were chosen to have a Ge concentration similar to that of the PECVD ones. The main structural features (Ge concentration, QD mean size and QD concentration) of sputter samples can be found in **table 3.2**. Despite of similar values of Ge concentration, QDs synthesized by PECVD method are larger compared to the ones synthesized by sputtering deposition. This is probably due to the lower annealing temperature ($T=600^{\circ}\text{C}$) used in sputter samples.

Such a higher annealing temperature has been required in PECVD films to have a proper phase separation of the SiGeO alloy, in fact different kinetics for QD nucleation among PECVD or sputter matrices was observed [35]. Moreover, also the sputter samples allow the formation of a large amount of QDs after annealing, with typical concentrations of the order of 10^{18} – 10^{19} QD per cm³ (very similar to values obtained for PECVD samples). More details on the sputter samples are given in ref [87].

Synthesis Technique	Ge concentration, C_{Ge} [at/cm ³]	QD size, $2r$ [nm]	QD concentration [QD/cm ³]
Sputter 600°C annealing	5.5×10^{21}	2 ± 0.5	1.2×10^{19}
	6.0×10^{21}	2.5 ± 0.5	7.2×10^{18}
	1.15×10^{22}	3 ± 0.5	1.3×10^{19}
	1.25×10^{22}	4 ± 0.5	6.8×10^{18}

Table 3.2: Ge concentration of SiGeO films, mean size and concentration of Ge QDs obtained by sputter technique. The error bar in the QD size is referred to the size distribution

3.3 QD/matrix investigation: the role of growth method

In this paragraph we present an exhaustive comparison of the interface state of Ge QDs grown by PECVD or sputter techniques. In order to provide a comprehensive structural and chemical analysis of the QD interface, we performed a detailed investigation by electron energy loss spectroscopy technique (EELS), moving from the matrix to the core region of single QD for PECVD (**figure 3.5a-c**) and sputter (**figure 3.5d-f**) samples. The STEM images in the insets of **figures 3.5b-3.5e** reveal the three areas (core, interface and matrix) in which the EELS spectra were measured for PECVD and sputter samples, respectively.

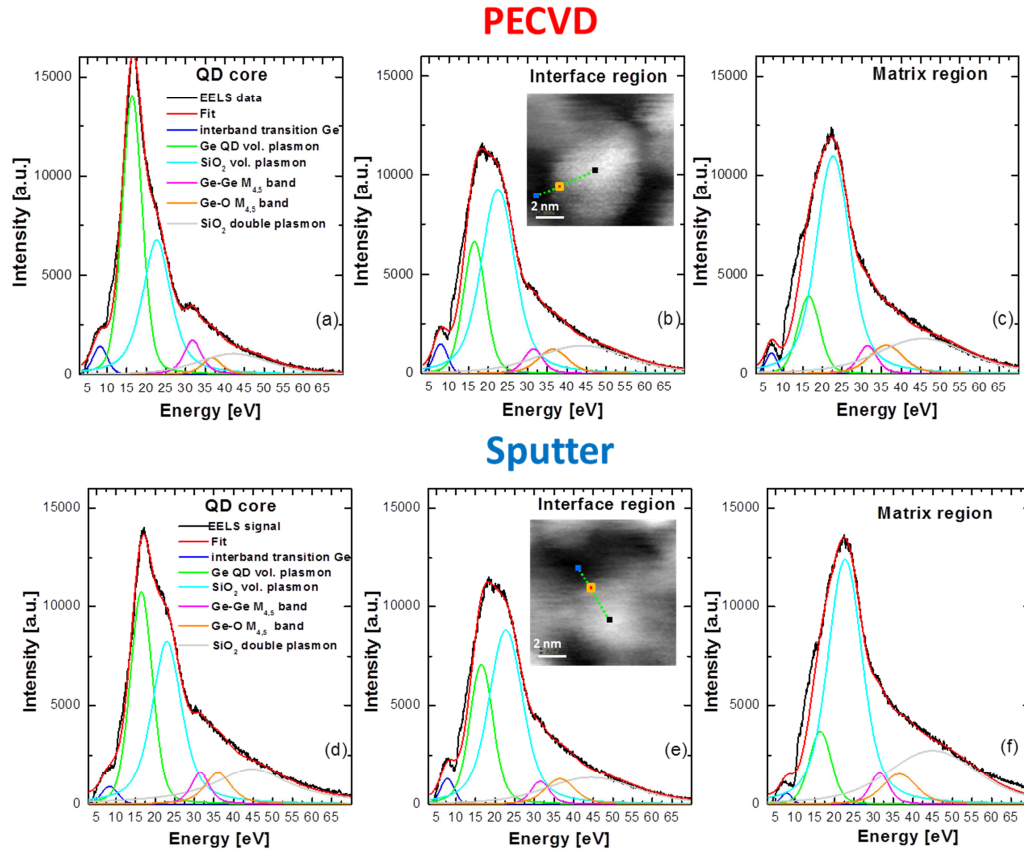


Figure 3.5: EELS spectra and the corresponding fits related to PECVD QD (core (a), interface (b) and matrix (c)) and sputter QD (core (d), interface (e) and matrix (f)) [47].

The electron energy-loss spectroscopy (EELS) is an analytical technique that measures the change in kinetic energy of electrons after they have interacted with a specimen. As electrons pass through a specimen, they interact with atoms of the solid, changing both its energy and momentum. This scattered incident electron can be detected by spectrophotometer, giving rise to the electron energy loss signal. An EELS spectrum is typically composed of a zero-loss peak, plasmon-loss peaks, and element-specific ionization edges, each superimposed on a background arising from the lower energy loss processes. The zero-loss peak consists mainly of

elastically scattered electrons and electrons that have excited phonons and thus lost very little energy. Plasmon-loss peaks are found in the range 10 eV to 50 eV, and are losses caused by excitations of collective oscillations of the conduction electrons (plasmon). For energy losses above the low-loss region, the features mainly depend on the ionization energies of the present elements. At the ionization energy for a specific element there is often a sharp edge, followed by a slow decay. The energy at which the edge appears is element-specific and can be used for element identification and quantification. This technique is used to determine the atomic structure and chemical properties of a specimen, including: the type and quantity of atoms present, chemical state of atoms and the collective interactions of atoms with their neighbors. The energy resolution is typically 1 eV but can approach 0.1 eV if an electron-beam monochromator is used.

All our STEM-EELS measurements were performed in the low-loss (5 – 70 eV region) electron energy loss region by using the Gatan STEM EELS spectrum imaging (SI) tool. Spectrum imaging (SI) is a technique that generates a spatially resolved distribution of electron energy loss spectroscopy (EELS) data. A typical experiment involves the creation of a data cube where two of the cube axes correspond to spatial information, while the third dimension represents the energy loss spectrum. To create this data cube, you can acquire a complete spectrum at each spatial pixel during scanning transmission electron microscope mode (STEM SI). During a STEM experiment, the electron beam focuses into a small probe, then scans over the sample to acquire spatial information (X,Y) in a serial manner. In the STEM SI mode, you can acquire a complete spectrum at each pixel position to build the spectrum image up on a spectrum-by-spectrum basis. Moreover, the analysis were performed in regions of the sample where the QDs do not overlap each other, in particular EELS line scan acquisitions were performed across the core, interface and matrix region of two individual QDs having a similar

dimension. The SI tool moves the probe systematically along the sample over a selected region of interest and the resulting EELS spectra are collected in a data box pixel-by-pixel, allowing advanced spectral post-processing to be performed for every pixel. Every single EELS spectrum has an energy resolution of 0.7 eV FWHM, 1.1 Å probe size, 50 pA of electron beam current, 20 ms of acquisition time, and the pixel size was $0.1 \times 0.1 \text{ nm}^2$. For our analysis, we accurately selected regions of the SiGeO films where QD size distribution was comparable and moreover, we chose QDs not smaller than 4–5 nm to minimize resolution deterioration due to plasmon delocalization, which usually is in the 1–2 nm range [88]. For both deposition techniques, moving from SiO₂ matrix to the QD core region a clear modification occurs in the spectra (**figure 3.5a-f**). This is a direct signature of the different chemical contributions around the QD that are probed by the electron beam. In fact, the overall EELS spectrum contains several contributions coming from the plasmonic excitation of Ge, the surrounding SiO₂ matrix and any Ge oxides states eventually present at the interface of QD [89]. The remaining components are related to the inter-band transitions of the Ge-SiO₂ hetero-structure (5-10 eV range) and to the broad M_{4,5} ionization edge of Ge QD, starting at around 29 eV. This latter contribution gives important information on the chemical arrangement at the interface of Ge QDs. In order to give a quantitative estimation of these features, the different components of the spectra were extracted through a Voigt function fitting. Since our EELS spectra contain several contributions, we chose fixed values of peak and FWHM of the different contributions, accordingly with the values reported in literature. Therefore, the only free fitting parameter is the area of the different peak contributions, while the overall fitting inaccuracy is <5%. The general trend, by scanning the beam from QD core to the matrix region for both sputter and PECVD QDs, is an increase of the SiO₂ plasmon intensity and a decrease of the contributions coming from Ge

plasmon. At the same time, Ge-O intensity slightly increases at the expenses of a reduction of Ge M_{4,5} edge intensity. This kind of behavior was expected. In fact, as reported in **figure 3.6**, by moving the electron beam from QD core (**figure 3.6a**) to the matrix region (**figure 3.6b**) a larger “effective thickness” of the interface is probed by the scanning electron beam and also a larger contribution of the SiO₂ signal coming from the matrix.

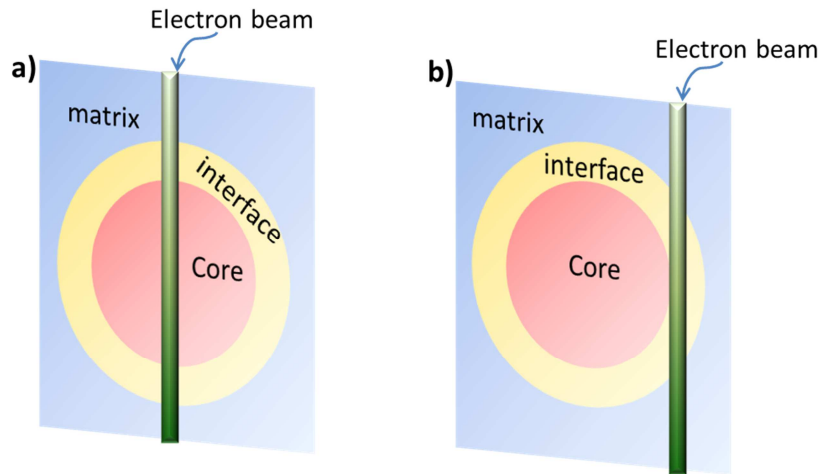


Figure 3.6: Schematic representation of QD regions probed by the electron beam: core region (a) and interface region (b)

From a closer comparison of the EELS spectra in the core region of sputter [**figure 3.5d**] and PECVD [**figure 3.5a**] samples, different features are clearly visible, as a lower contribution of SiO₂ volume plasmons appears for the latter. Moreover, both sputter and PECVD QD spectra show the presence of a broad peak centered at around 36 eV related to Ge-oxides (GeO_x, $x \leq 2$) species [91] Indeed, the sputter film seems affected by a larger fraction of GeO_x species with respect to the PECVD one. In fact, given the areas of Ge-O contribution (A_{Ge-O}), Ge-Ge M_{4,5} band (A_{Ge-Ge}) and Ge volume plasmon

peak (A_{Ge-pl}), the amount of Ge-oxide species (here quantified as: $F_{Ge-O} = A_{Ge-O} \cdot (A_{Ge-Ge} + A_{Ge-pl})^{-1}$) for the sputter sample ($F_{Ge-O}^{sputter} \sim 16 \pm 2\%$) appears to be twice that for the PECVD one ($F_{Ge-O}^{PECVD} \sim 8 \pm 1\%$). Such a result evidences a chemically different interfaces among PECVD and sputter QDs, with a relatively larger amount of Ge-oxide and sub-oxide states in the latter. In order to give more insights into the structural arrangement around the QD interface, we performed line-scan acquisitions of the Z-contrast signal of high resolution HAADF STEM micrographs on Ge QDs in SiO₂ with similar size for both techniques ($\sim 3 \div 4$ nm). The intensity of HAADF signal mainly depends on the atomic number, Z, of the observed atomic species. Therefore, by considering the intensity of the Z-contrast signal across the QD diameter, it is possible to get reliable results on the interface thickness of our Ge QDs in SiO₂. In **Figure 3.7** the typical profile of the Z-contrast signal taken over a segment from the matrix to the core region of sputter and PECVD Ge QDs (both of ~ 3.5 nm diameter) is reported. The intensity of the Z-contrast signal increases while moving from the matrix to the core region of the QD. This increase contains a “sphere-shape” contribution and the intrinsic thickness of the interface shell. The “sphere-shape” contribution comes from the shape-dependent SiO₂ thickness around the QD that is probed by the scanning electron beam, as drawn in **figure 3.7**. By fitting the Z-contrast signal with sigmoid functions $f(x) = (1 + e^{-(x-x_0/\Gamma)})^{-1}$, where x_0 represents the point of inflection of the sigmoid function and Γ the characteristic length of the function increase, we estimated Γ of 2.6 ± 0.1 nm for sputter and 2.0 ± 0.1 nm for PECVD sample. These values denote that a fairly sharp interface can be assumed only for the PECVD case, while a thicker one is evidenced for the

sputter sample. Such behavior was observed for all the investigated QDs in our analysis. Given that QD diameter is about 3.5 nm for both samples, Γ is expected to be at least as large as half a diameter, for the “shape” contribution, with the exceeding portion ascribable to the interface thickness.

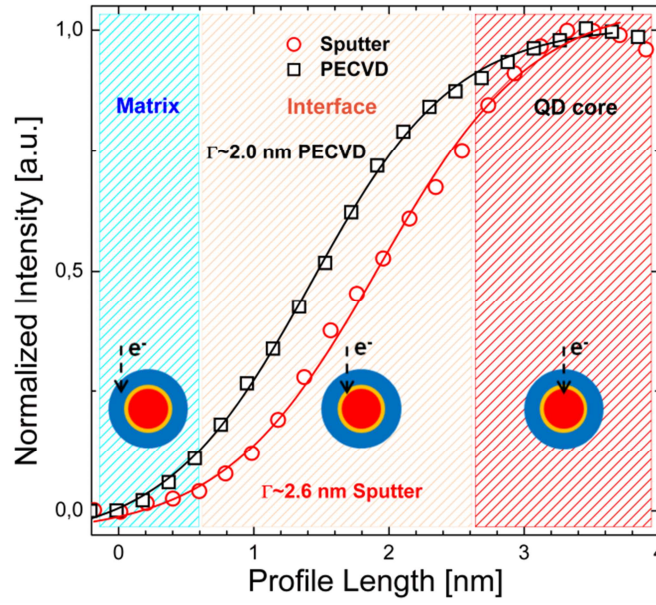


Figure 3.7: Profile length of the Z-contrast signal across the diameter of sputter and PECVD Ge QDs (c). A schematic of the different regions probed by the scanning electron beam is reported.[47]

Therefore, high resolution STEM-EELS technique demonstrates a chemical and a physical differences in the QD-matrix interfaces among sputter and PECVD films, with the first one thicker and richer in Ge-oxides than the latter one. The presence of such an interface shell and its variation with the synthesis technique, in terms of thickness and stoichiometric oxide quality,

is of paramount importance for the strength of carrier confinement occurring in nanostructures.

3.4 Interface effects on light absorption in Ge QDs

In this paragraph, we study the light absorption of Ge QDs in SiO₂ to investigate if, and to which extent, the previous observed interface differences between sputter and PECVD samples can influence the strength of QCE. To* this purpose, once measured the direct optical transmission and reflectance spectra of Ge QDs through the spectrophotometry analysis, we evaluated the experimental absorption coefficient of films by using the DPA approach (already introduced in the chapter 2). It is worth noting that the comparison among samples with different amount of Ge can be misleading as far as only the absorption coefficient α is concerned, since a different α can be trivially related to a different amount of absorbing centers. This problem can be overcome using the absorption cross section σ , defined as the absorption coefficient α normalized to the Ge atomic density, D , involved in the photon absorption process ($\sigma = \alpha \cdot d / D$) [92]-[93]. Thus, the absorption cross section σ represents the photon absorption probability per each Ge atom. **Figure 3.8** shows the spectra of absorption cross sections for sputter and PECVD films with different sizes of Ge QDs. Errors on the σ values (coming from indetermination on α , L and D) are comparable with the symbol size. A clear size-dependent shift of the absorption edge due to QCE is observed for both sets of samples. However, a different size-dependent shift of the absorption edge also appears, with PECVD QDs exhibiting a larger blue-shift than sputter QDs. In particular, QDs grown by sputtering or PECVD and having a similar size show a different edge of the absorption

cross section, as shown in **figure 3.8**. Moreover, also a different shift of the absorption edge with size appears. In fact, when the size of PECVD QDs shrinks from 4 to 3 nm, a consistent blue-shift of the absorption edge of about 0.5 eV is present. On the contrary, only a reduced tuning of the absorption edge is present for QDs produced by sputtering technique with the same size shrinkage. These results indicate that the light absorption of these systems are not set by size alone and may be largely influenced by the interface. When the interface is sharp enough a stronger role of QCE is expected, as we observed.

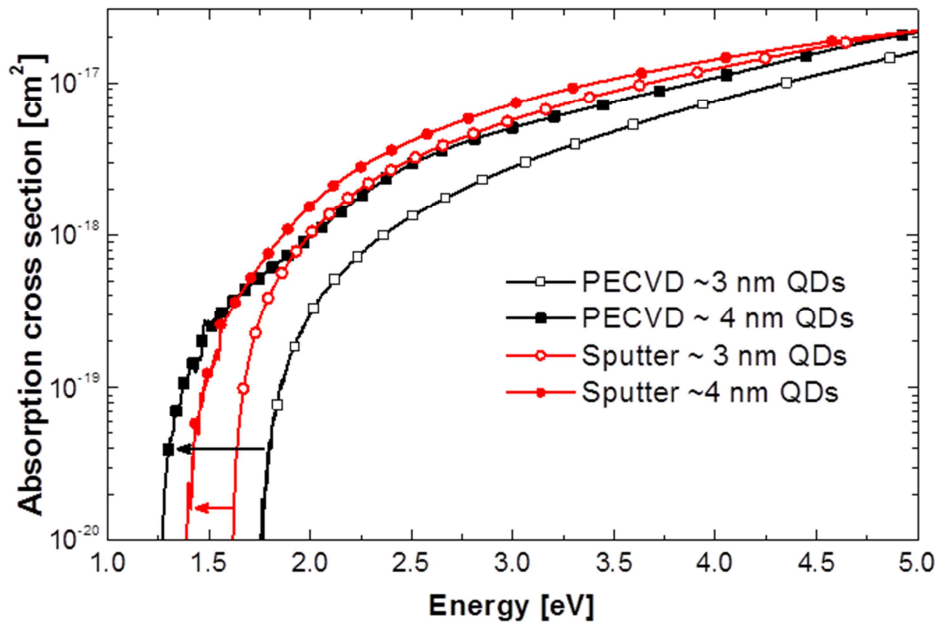


Figure 3.8: Absorption cross section spectra for sputter and PECVD films with different sizes of Ge QDs.

Indeed, the absorption cross section is intimately connected to the optical bandgap E_g and the oscillator strength O_s of k -allowed transitions in the Brillouin zone (BZ) through the formula [49]:

$$\sigma(\omega) = \frac{4\pi^2 e^2}{nc\mu_0^2 \rho \omega} \cdot |O_s|^2 \cdot \int_{BZ} \frac{2dk}{(2\pi)^3} \delta(E_c - E_v - \hbar\omega) \quad (3.2)$$

where ρ is the concentration of the absorbing centers, n is the refractive index of the material, μ_0 the exciton effective mass (EM) while the integral represents the joint density of states (JDOS) in valence and conduction bands involved in the absorption of a photon with energy $\hbar\omega = E_c - E_v = E_g$. As observed in chapter 1, according to the Tauc formalism, under the hypothesis of parabolic band edges and optical inter-band transitions between quasi localized states eq. (3.2) can be rewritten as

$$\sigma = \frac{B^*}{\hbar\omega} (\hbar\omega - E_g)^2. \quad (3.3)$$

The Tauc coefficient B^* is directly proportional to the oscillator strength of the optical transition, O_s , and thus represents an estimation of the efficiency of light absorption [63]. Then, it is possible to reliably determine E_g and O_s of nanostructures directly from their absorption cross section σ , as extensively discussed in chapter 1. So, we employed the modified Tauc plot (expressed by equation (3.3)) to experimentally measure E_g and O_s of our Ge QDs. Two examples of modified Tauc plot and corresponding linear fits for 4 nm sputter and PECVD Ge QDs are reported in **figure 3.9**.

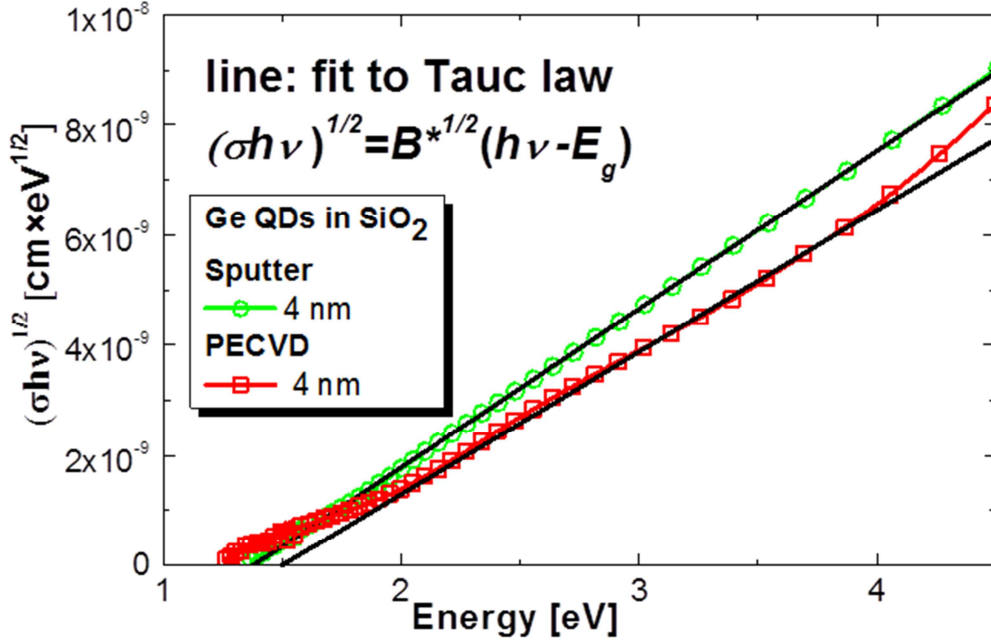


Figure 3.9: Selected Tauc plot (symbols) and corresponding linear fits (lines) for 4 nm Ge QDs produced by PECVD and sputter techniques.

The experimental values of E_g for Ge QDs, extracted by linear fit of Tauc plot and reported in **figure 3.10a**, reveal a different behavior between the two sets of samples. In fact, PECVD QDs shows a larger tuning of E_g with QD size, while a reduced energy dispersion appears for sputtered QDs. Moreover, the experimental tuning of E_g is not in good agreement with standard EMA model ($E_g(D) = E_g^{\text{bulk}} + A/D^2$, where A is the confinement parameter ($A = \pi\hbar^2/2\mu_0 = 7.88 \text{ eV} \times \text{nm}^2$) [48]), which actually does not fit any of the two data series [red line in **figure 3.10a**]. This result is a direct consequence of the different interfaces observed by EELS analysis between the two types of QDs. In fact, EMA model is usually used to describe carrier confinement in sharp and square-like potential barriers systems, considering

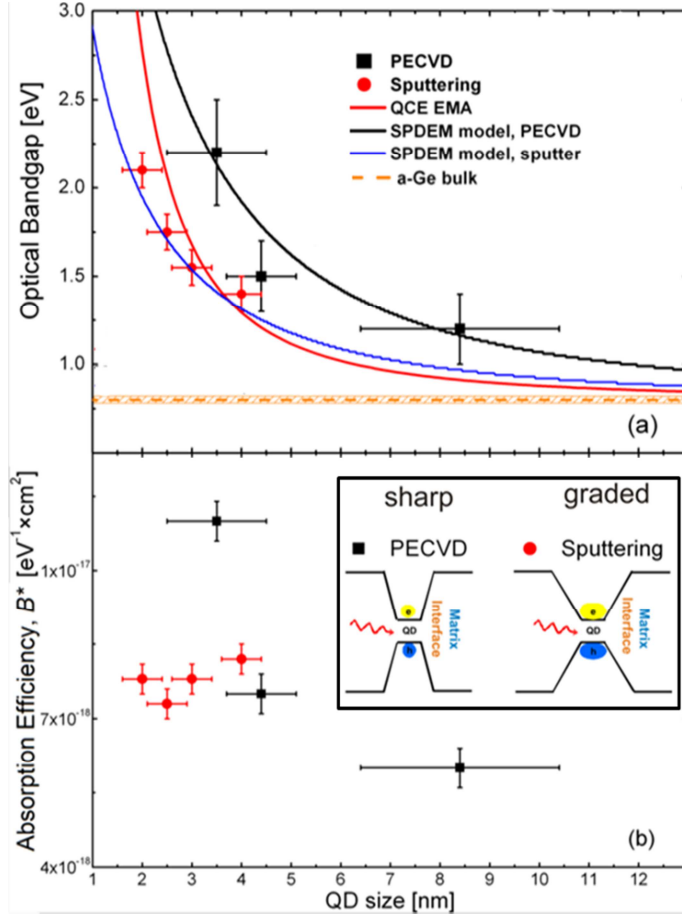


Figure 3.10: Size variation of the optical bandgap (a) and oscillator strength (b) of Ge QDs in SiO₂ synthesized by sputtering and PECVD technique. In (a) the red curve represents the standard EMA model of E_g for Ge QDs in SiO₂ [32] while the black and blue solid lines represent the theoretical trend of E_g considering the correction of the SPDEM into the EMA model [48]. The different (sharp or graded) interface confining potentials is drawn in the inset.

bulk values of EM and neglecting any effect caused by a spatially-graded confinement potential $V_c(x)$, typical in the case of an interface shell between QD and matrix. In order to describe the effect of the interface, a correction to the EMA model was developed through a spatially dependent effective mass (SPDEM) formalism [45]-[46].

As already discussed in the chapter 1, the SPDEM model is directly related to the potential $V_c(x)$ for confined carriers and describes the effect of V_c on the EM, through the dispersion relationship:

$$E_g(D) = E_g^{bulk} + \frac{3\hbar}{\mu(D)\sqrt{2} \cdot D} \left[\sqrt{\frac{V_{c,e}}{m_{c,e}^*}} + \sqrt{\frac{V_{c,h}}{m_{c,h}^*}} \right] \quad (3.4)$$

where $\mu(D)$ is the renormalized SPDEM of excitons, $V_{c,e}$, $V_{c,h}$, $m_{c,h}^*$ and $m_{c,e}^*$ are the confinement potential and effective mass for electron and hole [45]-[48]. The inclusion of the SPDEM into EMA model gives better agreement between theory and experiment, as shown in **figure 3.10a** (black and blue lines). In particular, $V_{c,e}$ and $V_{c,h}$ were determined as fitting parameters in ref. [48], assuming QD interfaces mostly composed by GeO₂ and GeO in the case of PECVD and sputter QDs, respectively. We found a larger interface potential for PECVD QD ($V_{c,e}^{PECVD} \sim 1.1$ eV, $V_{c,h}^{PECVD} \sim 3.3$ eV, **figure 3.11b**) with respect to sputtered ones ($V_{c,e}^{sputter} \sim 0.9$ eV, $V_{c,h}^{sputter} \sim 2.8$ eV, **figure 3.11c**). Moreover, it should be noticed that the potential offset extracted from the fit of PECVD QDs are close to the energy offset between Ge/GeO₂ ($V_{0,e}=1.2$ eV and $V_{0,h}=3.6$ eV, **figure 3.11a**), as depicted in **figure 3.11** [94], confirming the higher quality of Ge-oxide, as already indicated by EELS analysis. Moreover, a sharp interface potential is correlated with a larger reduction in the EM, which gives rise to an increased energy dispersion through Eq. (3.4).

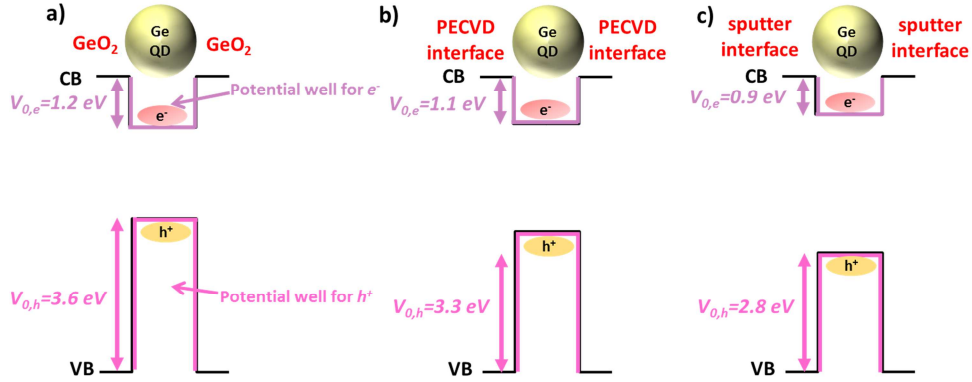


Figure 3.11: Schematic representation of confinement potentials of electrons ($V_{c,e}$) and holes ($V_{c,h}$) for different Ge QD interfaces: Ge QD/GeO₂ (a) [KobayashiJAP2009], Ge QD/PECVD interface (b), Ge QD/sputter interface (c). $V_{c,e}$ and $V_{c,h}$ in PECVD and sputter samples were determined as fitting parameters of equation (3.4) in ref. [48].

Therefore, by considering our Ge QDs as composed of a core region and an interface shell (as depicted in **figure 3.12**), we can conclude saying that PECVD QDs are closer to an ideal-like system, with a very sharp interface mostly composed by a GeO₂ shell between Ge QD and SiO₂ matrix. On the other hand, sputter QDs suffer from a thicker interface with a more complex contribution of sub-stoichiometric Ge-oxide states that give rise to a graded interface, as schematically drawn in the inset of **Figure 3.10**.

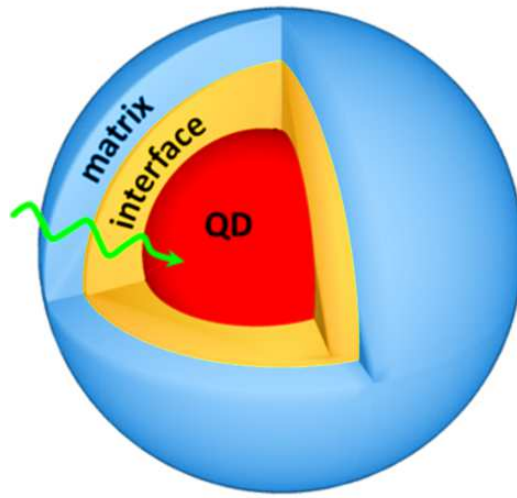


Figure 3.12: A schematic illustration of a Ge QDs embedded in a surrounding matrix (blue region) and composed of core region (red region) and interface shell (yellow region).

While a sharp interface allows a large tuning of E_g through an effective exciton confinement and EM reduction, a spatially-graded interface gives rise to a weaker confinement effect. These evidences point out the paramount role of the interface in modifying the carriers confinement in nanostructures. Finally, the effect of the interface on the quantum confinement of Ge QD is visible also in the trend of the Tauc coefficient B^* .

This quantity is directly proportional to the oscillator strength O_s of light absorption through eq. (3.2) [95]. In particular, O_s is strictly connected to the confinement of excitons through the exciton envelope function, $G_{nm}(k)$, and the optical matrix element, $P_{nm}(k)$, according to the formula [96]-[97]:

$$O_s = \frac{2}{\mu \cdot E_g} \cdot \left| \sum_k G_{nm}(k) \hat{x} \cdot P_{nm}(k) \right|^2 \quad (3.5)$$

The increase of the oscillator strength is usually observed, both experimentally and theoretically, in highly confined systems having a dimension smaller than the exciton Bohr radius [80]-[96]-[97]. This effect is often explained only as a consequence of the increased electron-hole overlap G_{nm} when the spatial dimension of the system is reduced. Our comparison between sputter and PECVD Ge QDs illustrates two systems whose size variation is on the same range of 2 – 10 nm. Thus, we should expect quite a similar G_{nm} factor for both types of QDs and, consequently, a similar trend for the variation of O_s . However, this is clearly not the case. **Figure 3.10b** shows the size-dependent variation of B^* for PECVD and sputtered QDs. While PECVD QDs show an increased absorption efficiency for very strong spatial confinement, a fairly constant B^* appears in sputtered samples over the same size range. The different behavior observed for our systems suggests that other factors must be considered. Indeed, the variation of the reduced EM (μ) on the spatial dependence of O_s has also to be considered. The better Ge-oxide quality and higher interface confinement potential in PECVD QDs yield a larger reduction in the reduced EM, which gives rise to an enhanced O_s , according to Eq. 3.2, and therefore to the increased B^*

observed in **Figure 3.10b**. On the contrary, the different behavior found for sputter QDs is a consequence of their interface quality. As thicker and poorer the Ge-oxide quality at the interface, the weaker the exciton confinement is. This effect gives rise not only to a reduced confinement for what concern the energy dispersion relationship, but also to an anomalous size-independent oscillator strength. Therefore, the role of the interface is a key-factor in the optical behavior of nanostructures. This is fundamental not only for a full understanding of the QCE in nanostructures, but also for exploiting their optical properties through both the control of size and interface engineering.

3.5 Conclusions

In this chapter, we have reported an exhaustive investigation on the role of interface with respect to the quantum confinement effects occurring in Ge QDs. To this purpose a closely packed arrays of 3 – 9 nm diameter amorphous Ge QDs in SiO₂ were produced by PECVD techniques to be compared to Ge QD in SiO₂ grown by sputtering and previously investigated by our group. The structural quality and chemical composition of PECVD QD interface was compared, by extensive EELS analysis, with that of some sputter samples which show similar structural characteristic in term of QD size and density. The EELS analysis reveals a different interface in the two samples. In particular, we found a sharper and better quality interface for PECVD QDs, while sputtered QDs are characterized by a thicker interface shell containing twice the contribution of Ge-oxide states with respect to PECVD. Such chemical and structural difference in the interface is strongly related to the different optical behaviour exhibited by Ge QDs. In fact, while a large size-dependent tuning of both bandgap and optical oscillator strength

is found for PECVD QDs, on the contrary, sputter QDs exhibit a size-independent oscillator strength and a moderate tuning of the bandgap. These differences, were successfully explained by using a spatially dependent effective mass model, which accounts for the effect of the interface potential on exciton confinement. In particular, a sharp interface potential, as that occurring in PECVD samples, is correlated with a larger reduction in the EM, which gives rise to an increased energy dispersion and an increase of absorption efficiency. These results provide new understanding of the role of interfaces on the quantum confinement effects in nanostructures. Moreover, our results indicate a further direction for an optimized exploitation of confinement effects in future nanostructures-based devices: not only by exploiting size effects, but also taking advantage of proper interface engineering.

Chapter 4

Enhancement of light absorption in Ge QDs orderly distributed in SiO₂

In this chapter, we present an experimental investigation of light absorption in small Ge QDs (2-3 nm in diameter) grown by PECVD in a multilayer configuration (3-6 nm thick film with Ge QDs, separated by 20 nm thick SiO₂ barriers) and annealed at 800 °C. The multilayer approach allows a narrower size distribution in comparison to a single layer of QDs (where no SiO₂ barrier layers are involved). During the discussion, we compare the structural properties of multilayer samples with single layer ones. To do this, transmission electron microscopy (TEM) analyses were performed in order to evaluate the size and size distribution of the Ge QD ensemble for both configurations. After that, by a detailed electron energy loss spectroscopy (EELS) analysis we characterized the structural and chemical properties of Ge QD in ML samples. Finally, by combining UV-Vis-NIR spectrometry and Tauc analysis of the absorption spectra, the optical bandgap and the absorption efficiency of Ge QDs were extracted. A very high absorption efficiency, 15 times larger than in bulk, has been observed for these systems. A comparison with Ge QDs in single thick layer is also performed, utilizing also the optical fitting. These results add new insights into the role of QD packaging on confined systems, and open the route for reliable exploitation of QC effects.

4.1 Introduction

Up to now, some theoretical and experimental studies indicate that the QDs spacing and arrangement can play an important role in the optical properties of these systems. For example, in a recent paper, Guerra et al, calculated the electronic structure of Si nanocrystals (NCs) and the role of the strain induced by a surrounding SiO₂ matrix or induced by lowering the distance in between the NC [98]. According to their calculations, the strain produced at the QD/matrix interface produces a red shift of the absorption spectra. In particular, they found that for nanocrystals smaller than 2 nm the proportion of atoms at the Si/SiO₂ interface becomes relevant, surface-related states occur that affect the quantum confinement and produce states in the band gap, thus changing the optical response of the system [99]. When a NC-NC separation is lower than 0.5 nm the strain-induced forces mutually acting on the NCs emerge, playing a relevant role over any other interaction mechanisms between NC.. Such calculations are also in substantial agreement with the results reported by Hapala et al., which observed a systematic blue-shift (~200 meV) of the bandgap for free-standing oxide-passivated Si nanocrystals compared to the matrix-embedded ones having the same size [100]. Furthermore, Uhrenfeldt et al. recently observed how the absorption of large and closely packed Ge NCs in SiO₂ ordered in multilayers exceeds that for similar concentration of NCs randomly distributed in the film [92]. They found indications that the order distribution and packaging of Ge NCs play an important role on the optical response of these systems and can prevail on the effects due to quantum confinement., determining a reduction or an increase of light absorption capacity of samples containing semiconductor QDs.

Another recent study was focused on the variation of joint local density of states (JLDOS) as function of distance between PbSe colloidal QDs [57]. In this work, Logar et al observed an increase of JLDOS in the region between QDs with the reduction of the distance between them (by changing the kind of ligand on surface of QDs). In particular, they found that this reduction of QDs spacing determine a growing electronic coupling between the latter which translates into an increase of EELS signal in the region between two QDs [57]. This strong electronic coupling between QDs could lead to increased optical absorption of the system, since the absorption coefficient is proportional to JLDOS (equation 1.16 in the chapter 1).

In order to clarify if and to what extent QD-QD interactions can modify the light absorption process, we will present, in the following paragraphs, an experimental effort designed to study the influence of packaging and spacing of QDs on the light absorption process. To do this, we will use the multilayer approach (ML) and we will compare the structural and optical properties of latter with those of a reference single layer sample where Ge QDs are randomly distributed in a thick film. A clear evidence of a light absorption enhancement by decreasing the QD-QD distance along the film growth direction is presented and discussed. In particular, an unprecedented high light absorption efficiency (about 15 times higher with respect to single layer (SL) sample and bulk samples) has been observed for the ML structure. This enhancement is independent on the number of layers, SiGeO film and SiO₂ barrier thickness, showing the primary role of spacing QDs along the film growth direction.

4.2 Synthesis and structural properties of multilayer of Ge QDs

In this experiment, Ge QDs embedded in SiO₂ were synthesized by depositing a SiGeO layer (30% Si, 10% Ge, 60% O) and annealing it at 800°C to induce the precipitation of the excess Ge nanoclusters, as already observed in the chapter 3. In order to have a better control of the nanoclusters synthesis, a multilayer (ML) approach (composed by barrier/SiGeO film/barrier structure) is used [101]. In order to compare the structural and optical characteristic of Ge QDs arranged in ML and single layer (SL) approach, a reference SL sample was also deposited. Both SL and ML samples were deposited by plasma enhanced chemical vapor deposition (PECVD) on quartz substrate kept at 250°C using GeH₄, SiH₄ and N₂O precursors. In particular, after a SiO₂ buffer layer (20 nm), thin films of SiGeO alloys in SL and ML configuration were deposited. The SL sample is 330 nm thick with a Ge concentration of about 10%, while ML samples have a thickness in the range 200-400 nm. Each ML sample was obtained alternating N times a basic bi-layer made of a thin (t_f) SiGeO film and a thin (t_b) SiO₂ barrier (table 1). In order to maintain the Ge concentration around 10% in each SiGeO films of the ML samples during the depositions the GeH₄ flux was kept constant for all ML samples. In this chapter, the name of samples refers to the typology (ML or SL), and reports the t_f - t_b thickness for ML samples. One additional ML sample were also fabricated with $t_f=4$ nm/ $t_b=3$ nm (ML4-3) in order to investigate the role of barrier on the light absorption.

The multilayer structure and thickness, as well as the presence of Ge QDs

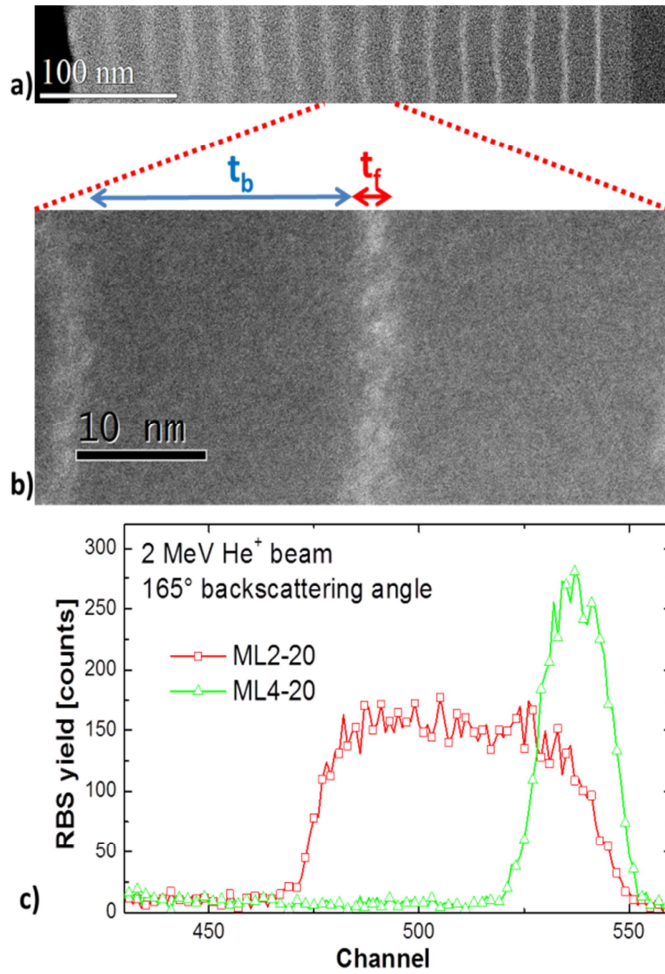


Figure 4.1: a)-b) Cross sectional transmission TEM images of Ge QDs multilayered samples at low and high magnifications. c) RBS spectra performed on Ge QDs with different thickness of SiGeO film and number of layer.

were evaluated by cross sectional Transmission Electron Microscopy analysis, through a sub-Ångström ARM200F microscope operating in scanning mode (STEM) at 60 kV. Low energy of the electron beam (60 keV) is used to reduce the damage in the samples due to the passage of the electron beam. In fact, for higher energy (~200 keV) of the electron beam, we observed a large amount of damage to the sample, leading to the complete destruction of the sample. In order to perform the TEM analysis, the SiGeO films were thinned by a standard cross-sectional technique and mechanical polishing followed by Ar⁺

ion milling at 2.5 keV (Gatan PIPS). In **figure (4.1a)**, the lower magnification TEM image shows the multilayer structure of the films with

SiO₂ barriers (darker layers) and very thin films containing Ge QDs embedded in SiO₂ matrix (brighter layers). To better evidence the presence of Ge QDs in each film, in **figure 4.1b** the TEM image at higher magnification of tightest multilayer sample (ML2-20) is reported. The image confirm the presence of very small (2r~2nm) and densely packed Ge QDs with a narrow size. The TEM analysis confirm also the amorphous phase of Ge aggregates. This limited crystallization can be accounted for by the smaller size of QDs with respect to required critical radius for crystallization of Ge aggregates in SiO₂ [35]. As reported in table 1, the QD size does not vary significantly in all ML samples, regardless of SiGeO film thickness. As far as the SL sample, Ge QDs size is slightly larger (2.9 nm), suggesting that in confined SiGeO layer a stronger Ge out diffusion (towards top and bottom barrier layer) probably occurs leading to a smaller Ge QDs.

Samples	t _f [nm]	t _b [nm]	N	Ge dose [10 ¹⁵ at/cm ²]	S ₂ S [nm]
ML2-20	2	20	15	22	1.2
ML4-20	4	20	4	11	1.0
ML4-3	4	3	8	16	1.3
SL	330	-	4	220	3.0

Table 4.1: Structural characteristics of ML samples and a reference SL sample.

In **figure 4.1(c)** we report the RBS spectra of He⁺ backscattered from Ge atoms for two representative multilayer samples (ML2-20 and ML4-20). The Rutherford backscattering spectrometry (RBS) analysis were

performed by using a 2.0 MeV He⁺ beam in random configuration and with a backscattered angle of 165°. Although the film/barrier multilayer structure cannot be resolved with this technique, the Ge distribution in the three samples appears more concentrated, as expected, with increasing the number of layers (from 4 to 15) or by reducing the thickness of the SiO₂ barrier (from 20 nm to the 3 nm). Each RBS spectrum was simulated by using SIMNRA software to determine the Ge content in each film. In particular, the so-extracted Ge dose shows a decrease from 22x10¹⁵ at/cm² to 11x10¹⁵ at/cm² with decreasing the layers number N. This is clearly related to an increase of overall SiGeO film thickness (defined as L_S=N*t_f) in each ML sample. Despite the Ge dose differences between various ML samples, the Ge concentration in each single SiGeO layer ($C_{Ge}^{SL} = \frac{D_{Ge}}{Nxt_f}$) is about of 7% (from 5 x10²¹ at/cm³ to 7x10²¹ at/cm³) for all ML samples, as we wanted to achieve.

Once the QD mean size and the Ge dose in the SiGeO film were estimated, by assuming that after thermal annealing all Ge excess in the alloy is fully involved in the QD nucleation and growth, it is possible to roughly estimate the average QD concentration ($C_{QD} = \frac{D_{Ge}}{\frac{4}{3}\pi r^3 \rho N t_f}$ where ρ is atomic density of Ge) and also the surface to surface QD separation ($S_2S = (1 / \sqrt[3]{C_{QD}}) - 2r$). In the light of small thickness in ML samples, the SiGeO films can be considered as two dimensional layers and thus the extracted S₂S value is relative to QD-QD distance along a surface-parallel direction of SiGeO film. Along this direction, the ML samples allow the formation of a large amount of QDs after thermal annealing, with typical concentrations of the order of 10²⁰ QD per cm³. This value corresponds to a typical mean distance of about

1.2 nm between the surfaces of two adjacent QDs. Clearly, the distance between QDs along growth direction of SiGeO films is fixed at 20nm or 3 nm due to the presence of SiO₂ barrier. On the contrary, in the single layer sample, the SiGeO film is thick enough (~300 nm) give a 3D distribution of QDs, so that the calculated S₂S results to be ~3nm, whatever the directions is. Summarizing in comparison with the SL one the ML approach provides a higher density of smaller Ge QDs. This can be related to the different QDs nucleation/growth balance due to the barrier presence in ML structure which restricts the growth process.

In order to investigate the local chemical composition of the Ge QDs, we performed a detailed investigation by low-loss (5 – 70 eV region) EELS technique. moving from the matrix to the core region of single QDs (**Figure 4.2**). Given the larger density of Ge QDs in ML, one key question is to characterize the chemical composition of the Ge QD core and of its matrix (i.e. of material in between QDs). Moreover, in order to compare the SiO₂ status in the matrix and in the barrier region, a EELS measurement was also performed in SiO₂ barrier region (**figure 4.2c**). As already observed in the chapter 2 (where the EELS analysis were performed on randomly distributed single layer Ge QDs), the overall EELS spectrum contains several contributions such as the plasmonic excitation of Ge (at ~ 16-17 eV), the surrounding SiO₂ matrix (at ~ 23-25 eV) and the Ge oxides states (at ~ 36 eV) [89].

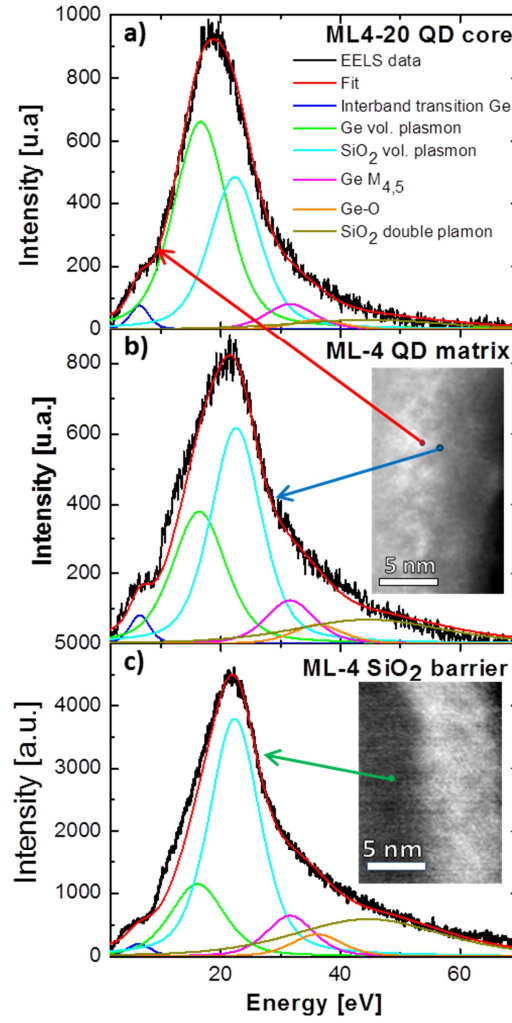


Figure 4.2: Low-loss EELS spectra of multilayered Ge QD in SiO₂ measured in the core (a), matrix(b) and barrier region (c). The STEM images in the insets reveal the probed area in the three cases. The different components of EELS spectra are fitted using the Voigt function and are reported in all three panels.

The different components of the spectra were de-convoluted through Voigt fitting (color lines in **figure 4.2**). For the deconvolution of EELS spectra, we

have chosen to fix the values of peak and FWHM of the different contributions, in accordance with the values reported in literature. In this way, the only free fitting parameter was the area of the Voigt function. As shown in **figures 4.2a** and **4.2b**, moving from SiO₂ matrix to the QD core region (inset **figure 4.2b**) a clear modification of the EELS spectra can be observed. As already observed in chapter 3 for single layer Ge QDs, this modification is related to the different chemical contributions that are probed by the electron beam. In particular, a clear decrease of the contribution related to Ge volume plasmon together with an increase of the contribution due to volume plasmon of SiO₂ are observed moving from inside toward outside of QD. This effect can be easily observed by the decrease of G parameter, defined as the ratio between contribution area of Ge volume plasmon and the area of SiO₂ volume plasmon contribution. In fact, the G value decreases, going from 1.45 to 0.65, by moving from QD core to SiO₂ matrix. Moreover, the value of such G ratio, calculated in the QD core, is very similar to the value found for PECVD Ge QDs embedded in SiO₂ and distributed in a SL sample ($G_{SL} \sim 1.5$) [47], further confirming the presence of Ge aggregates in the ML samples. Furthermore, by comparing EELS spectra of matrix (**figure 4.2b**) and SiO₂ barrier (**figure 4.2c**), we observe as they are very close each other with a lower (but not null) contribution of the Ge volume plasmon in the latter. EELS analysis confirmed the formation of Ge QDs embedded in SiO₂ matrix in ML samples. Both in the matrix region and in the barrier region EELS spectra suggest presence of Ge, as the presence of Ge QD edge contribution at about 29 eV confirms. Such presence can be related to Ge diffusion or to technique artifacts.

4.3 Light absorption in Ge QDs multilayer structure

Once the formation and growth of Ge QDs in ML configuration has been evaluated and compared with results obtained for SL samples, the optical absorption properties were investigated to determine if the different configuration of QDs have an influence on the photon absorption mechanisms. To do this, the light absorption analysis were performed on samples deposited onto fused silica substrates. In particular, normal transmittance (T) and the 20° reflectance (R) spectra in the 200 to 2000 nm wavelength range were acquired using a Varian Cary 500 double-beam scanning UV/visible/NIR spectrophotometer. In order to compare the light absorption of Ge QDs arranged in the ML and SL configuration, we used the atomic absorption cross section (σ) extracted as follows:

$$\sigma = \frac{\alpha \cdot L_S}{D_{Ge}} \quad (4.1)$$

where α is the absorption coefficient spectrum and L_S is the overall SiGeO films thickness in each samples. The use of σ is required because of the different amount of Ge present in the various samples. In fact, the σ represents the photon absorption probability normalized to the Ge atomic content present in each sample and therefore it does not depend on number of absorbing centers. In figure 4.3, we report the σ spectra of ML2-20, ML4-20 and ML4-3 samples (red, green and blue symbols, respectively) and of SL sample (black symbols) extracted by using the double pass approximation (introduced in chapter 2). Errors on the σ values (coming from indetermination on α , L and D) are comparable with the symbol size.

In all ML samples and in SL samples, the energy onset is clearly much higher with respect to Ge bulk. This is clearly related to quantum confinement effect. It is worthy of note that, despite all ML samples show a similar energy onset compared to reference SL sample (~2 eV), the magnitude of σ spectra in ML samples is about ten times higher than that found in single layer case and Ge bulk. This suggests that a significant enhancement of light absorption process occurs on the ML samples. Moreover, as can be noted in **figure 4.3** by comparing the σ spectra of ML samples with each other, the light absorption enhancement is clearly independent of SiGeO layer thickness (t_f), number of layers (N) and SiO₂ barrier thickness (t_b).). As σ represents the photon absorption probability per each atom, the increase of σ in ML samples in comparison to SL sample can be related to the ordered configuration (QDs are located in parallel planes) or to the shorter S₂S value. It should be noted that the absorption enhancement in ML samples is not attributable to interference effects which should be modulated by t_f and t_b variation. The overlapping of σ in ML samples demonstrates that the higher density of very small Ge QDs there obtained is the key actor in this unexpected increase of light absorption. At the same time, the comparison between spectra of ML4-20 and ML4-3 samples evidences how the different thickness of SiO₂ (20 nm or 3nm) does not involve a significant change of σ spectra, suggesting a minor role of SiO₂ barrier on absorption process.

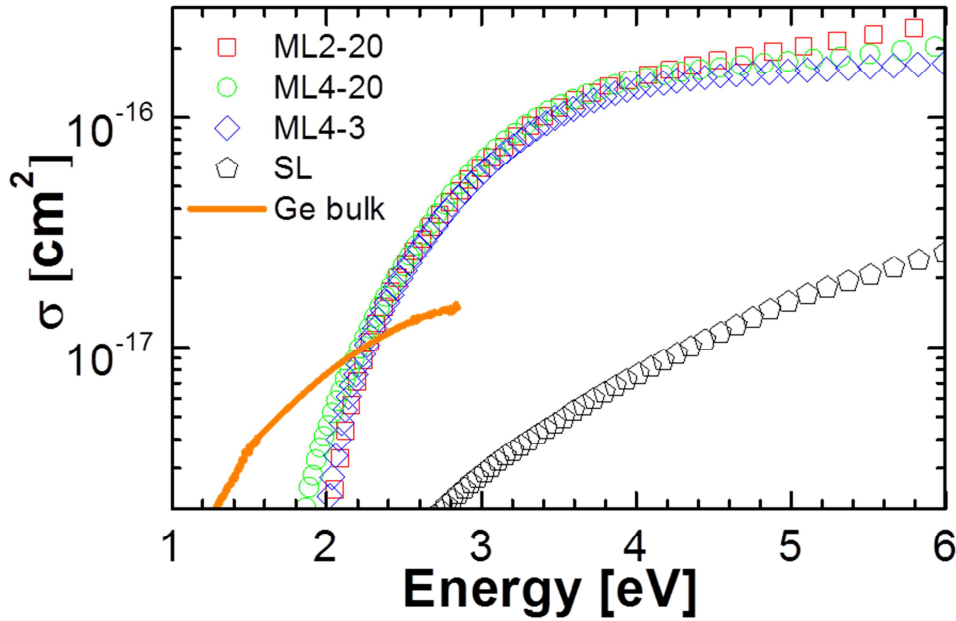


Figure 4.3: Absorption cross section of Ge QDs multilayers (ML2-20, ML4-20 and ML4-3). As reference, the spectrum of a SL sample is reported together with that of bulk Ge.

Other factors that can strongly influence the light absorption are the scattering effects at various SiGeO/SiO₂ interfaces in the ML structure which could determine a significant increase of light absorption. In fact, such effects usually determine an increase of the optical path of light in the sample, increasing the light absorption probability in the latter. To assess the real contribution of scattering effects on optical properties of ML samples, in **figure 4.4** we report the absorption cross section of a ML sample extracted by using the R and T spectra measured with or without the use of an integrating sphere, respectively. As reported in **figure 4.4**, the two σ spectra show no significant differences, demonstrating that the scattering effects do

not play a key role on optical absorption enhancement observed in ML samples.

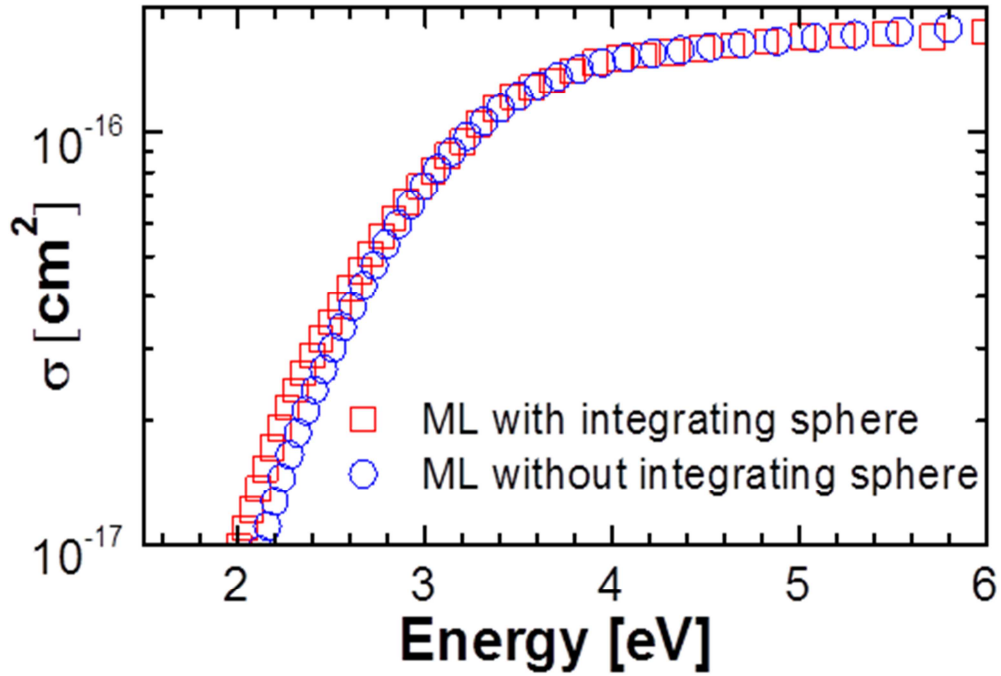


Figure 4.4: Absorption cross section spectra of a relative ML sample measured with or without use of integrating sphere.

With the aim to better investigate the light absorption enhancement observed in ML samples, we involved the Tauc model to describe light absorption process. In chapter 1, we have already observed how, under the assumption of parabolic band edges and optical transitions between extended states from valence band toward conduction band, the absorption coefficient of amorphous semiconductors is modelled by the Tauc's law [52]-[53]:

$$\alpha = \frac{B}{h\nu} (h\nu - E_g)^2 \quad (4.2)$$

where $h\nu$ is the incoming photons energy, E_g is the optical band gap, and B is the Tauc coefficient describing the efficiency in light absorption. Since the absorption cross section is related to the absorption coefficient through equation 4.1, the Tauc relation (expressed by equation (4.2)) can be rewritten as follows:

$$\sigma = \frac{B^*}{h\nu} (h\nu - E_g)^2 \quad (4.3)$$

where B^* is a modified Tauc coefficient, having the same meaning of B , only scaled to the Ge density. In **figure 4.5**, the modified Tauc plots (symbols) of ML samples and SL-330 sample together with the relative linear fit are reported. The linear fits in the modified Tauc plots were performed in the energy range for which $\alpha > 10^4 \text{ cm}^{-1}$ [52] which translates in $\sigma > 10^{-19} \text{ cm}^2$. The slope of fit is proportional to B^* , while the intercept gives the optical bandgap (E_g) of our samples. As expected because of σ spectra for ML, the linear fit of ML samples show very close intercept and slope values. If we compare ML samples to SL one, the E_g values are similar ($\sim 1.9 \text{ eV}$ for ML, 2.0 eV for SL) while the slope of linear fit in ML samples is about 10 times higher than in SL one. The application of Tauc model allows to conclude that the light absorption process in ML samples can be described in the same way as far SL sample but with a 10 times higher efficiency. Given that the E_g values does not change significantly, the increase in σ spectra can be due to an enhanced oscillator

strength in the interaction between electromagnetic field and Ge QD in ML samples.

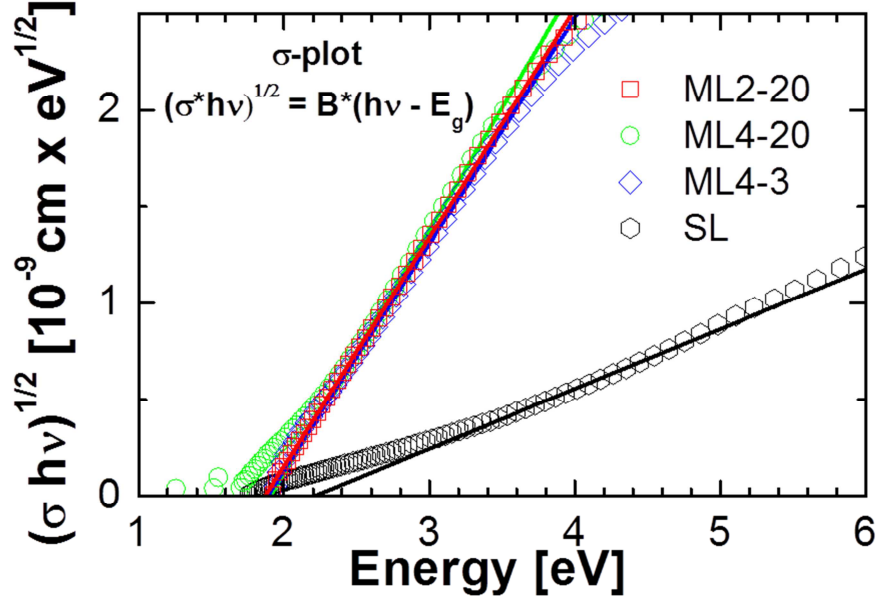


Figure 4.5: Tauc plot (symbols) and corresponding linear fits (lines) for Ge QDs arranged in ML and SL configurations.

4.4 Optical fitting

To further define the cause of this unprecedented increase in light absorption, an optical fitting model of R and T spectra is used to extract the imaginary part of refractive index ϵ_2 for ML and SL samples. The used approach for the optical fitting is based on the JTL model (described in chapter 2) further modified to account for the sub-band gap tails absorption. The model is known as JTL-GB model (Jellison Tauc Lorentz-Gaussian band model)[75] in which the sub-band gap tails absorption is modeled by making use of an

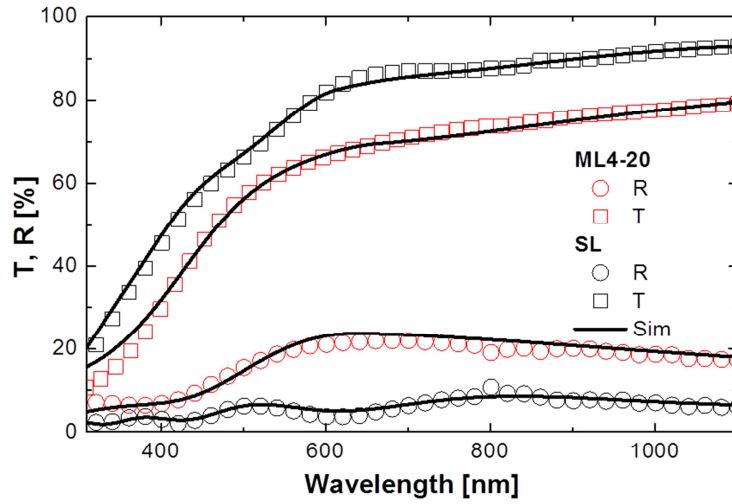
additional Gaussian band (GB), added to the imaginary part of dielectric function predicted within the JTL model (equation 2. in chapter 2). So, the imaginary part of the dielectric function (ϵ_2) is modeled by the following expression [75]:

$$\epsilon_2 = \frac{1}{E} \frac{AE_0C(E-E_g)^2}{(E^2-E_0^2)^2+C^2E^2} \theta(E-E_g) + A_T e^{-\left(\frac{E-(E_g+E_T)}{\sigma}\right)} \quad (4.4)$$

where the first term describes the JTL model (as already in chapter 2) and the second term describes the GB function. The JTL parameters are the band-gap of the material E_g , the oscillator amplitude A , the energy position of the Lorentz peak E_0 , and the broadening parameter C . The parameters of GB function are the central energy (E_T), the intensity (A_T) and the full width at half maximum (σ), describing a Gaussian distribution of a band energy levels within the energy gap. The real part ϵ_1 of dielectric function can be derived from ϵ_2 using the Kramers and Kronig relation, already introduced in the chapter 2.

In order to properly manage the eight fitting parameters, a first fitting cycle is performed using a ($E_g, E_0, A, C, \epsilon_\infty$) set able to fit R and T spectra of a bulk Ge used as standard. In this case (A_T, E_T, σ) is a null vector. When Ge QDs sample is considered, the E_g value as extracted by Tauc method is first introduced in the ($E_g, E_0, A, C, \epsilon_\infty$) set. Iterative fitting cycles based on χ^2 minimization are then used to determine the full set of parameters that supply the best fit between simulated and experimental R and T spectra. Each SiGeO layer was treated as an effective medium (EM) composed of Ge and SiO₂ materials. The (ϵ_1, ϵ_2) spectra of SiO₂ material inside the EM were set to the spectra reported in literature. Instead, for the Ge material, we

applied the optical fitting based on JTL-GB model. Therefore, the JTL-GB parameters, showed in this work, are referred to Ge material in the SiGeO film. The fitting was performed using the GTB-fit computer programme [75], which is based on the Optical code [74]. As reported in **figure 4.6**, the computed R and T spectra (black line), obtained using the optimized JTL-GB parameters, are in good agreement with the experimental R and T spectra (data points). This counterproves that no light scattering occurs in the ML samples.



Sample	E_g [eV]	E_0 [eV]	A	C [eV]	n_{inf}	A_T	E_T [eV]	σ [eV]	χ^2
ML4-20	1.87	3.1	5040	3.8	1.7	28.5	0.1	0.9	2.12
SL	2.0	2.76	212	3.8	1.3	1.9	0.3	0.7	0.94

Figure 4.6: Experimental (symbols) and computed (black lines) T and R spectra of a multilayer (ML4-20) sample and a single layer sample (SL)

In **figure 4.7** we report ϵ_2 for the Ge QDs in the ML4-20 sample and the reference SL sample. In the same graph, we report the contributions (dashed lines) to the ϵ_2 spectrum provided by the sub-band gap tail absorption for both samples. A proper converge of fit is obtained only by adding these sub-band gap tails, indicating a significant perturbation of the energy density of states in Ge QDs properly related to matrix/QDs interfaces defects, as it occur in ultrasmall Si QDs in SiC []. As clearly visible, the amplitude of ϵ_2 in ML4-20 sample is considerably larger (~25 times) than in SL case. The higher contribution of sub-band gap tails observed in ML samples (dashed green line in **figure 4.7**) than SL case (black dashed line in **figure 4.7**) is not able to justify the higher ϵ_2 values observed for ML samples in the energy range 2-6 eV. This demonstrates how the Ge atoms in the ML configuration are able to absorb much more light with respect to Ge atoms in the SL configuration.

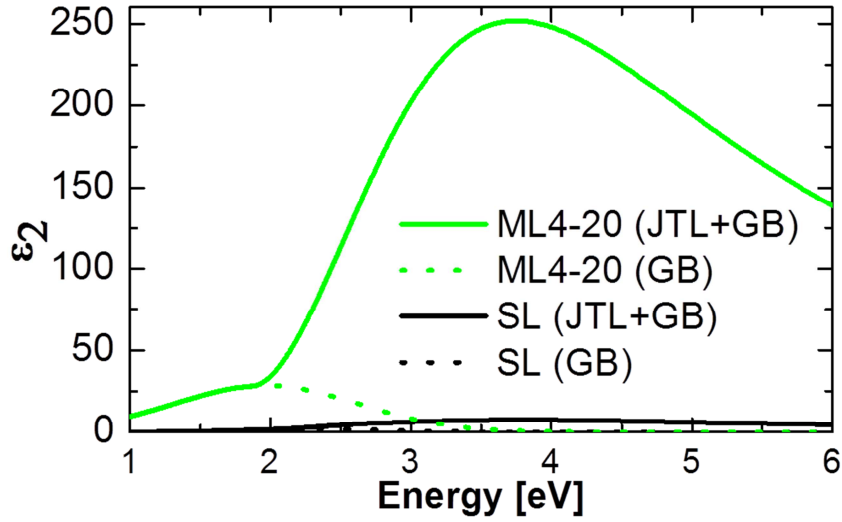


Figure 4.7: ϵ_2 spectra of ML4-20 and SL samples obtained by JTL-GB model. Table reports the eight JTL fitting parameters and the χ^2 test.

The higher contribution of sub-band gap tails observed in ML samples (dashed green line in **figure 4.7**) than SL case (black dashed line in **figure 4.7**) is not able to justify the higher ϵ_2 values observed for ML samples in the energy range 2-6 eV. This demonstrates how the Ge atoms in the ML configuration are able to absorb much more light with respect to Ge atoms in the SL configuration. As shown schematically in figure 4.7, in the light of the optical results and shorter distance between QDs observed in ML samples, we may suppose the existence of cooperative effects between QDs in ML samples which may produce a strong increase of photon absorption probability by single Ge atom present in QD.

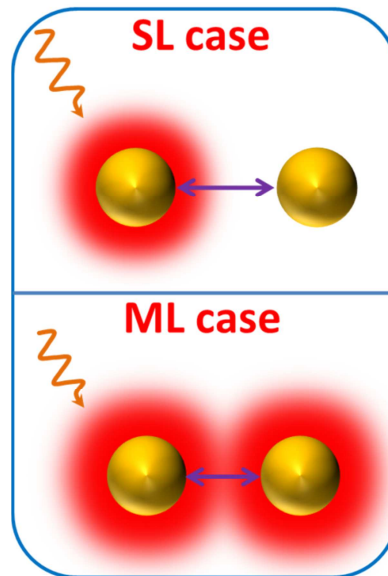


Figure 4.7: Schematic representation of the different strength interaction with light for SL and ML samples. The shorter distance between QDs observed in ML samples is responsible for light absorption enhancement.

4.5 Conclusions

In this chapter, we presented a large investigation on the structural analysis and light absorption of Ge QDs embedded in SiO₂ stacked in the multilayer configuration. Ge QDs in ML sample show a small average size (~2nm). The mean size of QDs is independent of the structural characteristic of samples (SiGeO film thickness and number of layers), proving that the nucleation process plays a dominant role in the growth process of Ge QDs. The EELS analysis, performed on our samples, confirm the presence of Ge QDs in the samples. and show how the SiO₂ status in matrix is very similar to that found in the barrier region. Moreover, the S₂S values, calculated by combining RBS and TEM data, evidence how the QDs in ML samples are more densely packed in each SiGeO film with respect to SL samples. The optical absorption of ML samples, performed by UV-Vis/NIR spectrophotometry, show a significant increase of light absorption capability in ML samples compared to SL case and Ge bulk. This light absorption enhancement in ML is confirmed by the optical fitting performed on ML and SL samples. The optical fitting (based on JTL-GB model) performed in the UV-Vis region evidence an extremely high ϵ_2 values in ML samples, about 15 times higher with respect to that of SL sample. Such absorption enhancement can be related to the different arrangement and the shorter distance between QDs along the SiGeO film direction observed in ML samples.

Conclusions

Some interesting advantages offered by the nanotechnology are related to the very small dimensions of objects and devices that can be manipulated and fabricated. This is certainly of extreme importance in many applications, but one of the most appealing consequences of nanoscience is that, below certain critical dimensions (the Bohr exciton radius), physical systems enter into the quantum physics word, exhibiting new properties called “*quantum confinement effects*”(QCE). In particular, QCE can be really effective in modifying the photon absorption process in semiconductor nanostructures (NS), opening new chances to increase the light absorption efficiency in photodiodes or photovoltaics devices. In this thesis, the main focus are QCE in Ge NS and how some conditions can hinder or modify such effects. To do this, we need to correctly extract the optical absorption coefficient, optical bandgap and refractive index spectrum of these structures. For this reason we have conducted a thorough study about the methodologies used to investigate and extract these optical parameters, especially the optical band-gap. In the literature several methods are used to determine the absorption coefficient spectra (starting from the experimental R and T spectra) and consequently to extract the optical bandgap. Recently, Liu et al [1], demonstrating the inefficiency of single pass approximation (SPA) for ultra-thin Ge QW, proposed a more reliable and complete method to determine the absorption coefficient spectra from R and T experimental spectra. This model, known as multiple reflection model (MRI), uses analytical equations containing Fresnel coefficients and numerical solutions using the transfer matrix method. For the extraction of optical band-gap, we have presented a

large comparison between Tauc and Cody models. On the choice among Tauc or Cody plots many papers are in the literature [1]-[2]-[3] and most of them focus on the light absorption in a-Si and a-Si:H, debating on the effect and magnitudes of tails states in the band gap and on the validity of Tauc [2] or Cody [3] model. Recently, the two models have been compared in sputtered Ge QWs showing that Cody plot can provide a more unambiguous determination of optical bandgap compared to Tauc plot [1]. Actually, since the models use different approximations and the linear fit to extract E_g have been done in energy ranges with a large variety of amplitudes (from 0.3 to 2 eV), special care must be taken to compare literature results. In particular, we consolidate the results extracted by Tauc model thanks to a systematic comparison with those derived with a more accurate parametrization fitting method. This shows that, despite its approximation, Tauc model gives reliable and precise results, providing advantages in terms of computational efforts and understanding of QCE.

However, the optical properties of Ge NS depend not only on the size through quantum confinement effects, since many other parameters can concur in controlling their optical behavior, especially for what concerns the optical bandgap. In particular, for a 3-dimensional confinement, as in an ensemble of quantum dots (QDs), the effects of quantum confinement can be hidden or weakened by other parameters, such as: QD spacing and distribution, type and quality of the hosting matrix and abundance of defects related to the synthesis technique. In particular, a real understanding of the possible role of the matrix/QD interfaces was often under-rated or ignored. Very recently, investigations on this topic appeared on several journals, which tried to disentangle the QCE in nanostructures from the effects of the surrounding interface and matrix. In particular, Eljarrat et al., investigated Si

quantum dots (QDs) embedded in oxide and nitride matrices by electron energy loss spectroscopy (EELS) analysis, trying to discern their electronic properties at the nanoscale and calculating a reduced exciton effective mass in confined systems [4]. Still, Mariotti et al. highlighted the aspects related to the interplay between quantum confinement and surface effects in Si nanocrystals. They concluded: “*major gaps between theoretical results and experimental evidence still need to be overcome in order to provide a coherent understanding of Si-nc behaviour and properties*” [5]. For these reasons, we have presented an original investigation on the QCE occurring in Ge QDs and the interplay with interface effects. In particular, we elucidated the connection between the structural composition at the interface of Ge QDs in SiO₂ and the confinement effects observed in the light absorption process. We demonstrate how a different interface shell can dramatically modify the size-dependent tuning of bandgap and oscillator strength. In order to describe the effect of the interface, we took advantage of a correction to the EMA model through a spatially dependent effective mass formalism. We explain our results as a consequence of the different confinement practiced by the interface potential, which gives rise to a difference in the reduction of the exciton effective mass and to the different size-dependent dispersions of the optical properties observed for Ge QDs. Our results provide a fundamental understanding about the role of interfaces on the optical behaviour of semiconductor nanostructures, which can be successfully exploited for future nanostructure-based devices.

Finally, we reported an experimental investigation of light absorption in small Ge QDs grown in a multilayer configuration. In this study we have investigated how the QDs arrangement strongly influences the absorption efficiency of Ge QDs. The ordered configuration (multilayer, ML) provides

a higher density of smaller QDs in comparison with the random configuration, caused by a different QDs nucleation/growth balance in the two systems. Moreover, the optical results obtained for Ge QDs in ML structures show an unprecedented high light absorption efficiency which results to be 15 times higher than that extracted for random configuration. In a recent work, Logar [6] et al reports a significant increase of joint local density of states (JLDOS) in the region between two adjacent QDs with decreasing the distance between them. Given that the absorption coefficient is proportional to JLDOS, an increase of the latter quantity can result in a significant increase of absorption efficiency by the QD ensemble. This means that, playing with packaging and distance, is possible to induce an enhancement of absorption efficiency by films containing semiconductor QDs. opening a new fascinating route toward the development of super-lattice semiconductor QDs for ultra-efficient light harvesting applications. In conclusion, the results reported in this thesis represent a step ahead for the full understanding of QCE in semiconductor nanostructures, for light harvesting applications. Many further aspects, in addition to those already examined in this discussion, still need to be clarified before the technological transfer of these materials to commercial light harvesting devices but the results obtained so far are extremely encouraging and promise that quantum effects will be part of our daily life in a near future.

- [1] P. Liu et al., *Journ. Appl. Phys.* **119**, 014304 (2016).
- [2] S. Knief, W. von Niessen et al, *Phys. Rev. B.* **59**, 12940 (1999).
- [3] T. M. Mok and S. K. O’Leary, *Jour. Appl. Phys.* **102**, 113525 (2007).
- [4] A. Eljarrat et al., *Nanoscale*, **6**, 14971 (2014).
- [5] D. Mariotti et al., *Nanoscale*, **5**, 1385 (2013).
- [6] M. Logar et al., *Nano Lett.* **15**, 1855 (2015).

Appendix 1

Ge advantages

Although today, the Si is considered the main element for the microelectronic applications, the Ge can be certainly considered the “father” of microelectronic. In fact, in the night of the Christmas Eve of 1947, W. Shockley J. Bardeen and W. Brattain invented the first transistor which was made of Ge crystal [102]. This invention created a breakthrough and signed the beginning of new era: “The microelectronic era”. Till the late ‘50s, germanium was considered the main material for the development of devices in the microelectronic field. Nevertheless, in the following years the subsequent fast and huge development of microelectronics and integrated circuits was based on silicon (Si). One of the most important historical reason is related to the poor quality and high instability of GeO_2 with respect to SiO_2 that limited the usage of germanium in complementary-metal-oxide semiconductor (CMOS) in favor of silicon. In addition, another reason why Si dominates the microelectronics industry is due to its abundance in Earth’s crust . In fact, the silicon is the second most abundant element in Earth’s surface (27%), only after oxygen (O). On the contrary the germanium is quite rare and widely dispersed. Obviously, the difficulty in finding the germanium leads to its high cost. For all these reasons, the use of Ge for microelectronic applications suffered a sudden stop. Recently, there is a renewed interest toward the use of Ge for microelectronic and optoelectronic applications. The revival of Ge is certainly due to the interesting electrical

and optical properties that it shows. One of the most important characteristics that makes Ge an attractive material to improve micro and optoelectronic devices is its high compatibility with the current Si-technology. This characteristic stems from the similarities of these two semiconductors that makes it possible to use for Ge the same production steps already used for Si technology. It is well known, indeed, that both Si and Ge belong to the same group in the periodic table (IV group) and thus they have the same crystalline structure: diamond structure. As shown in **figure A1.1a**, this kind of structure consists of two interpenetrated face centered (FCC) lattice in which the lattice parameter is indicated with the symbol a . The same crystalline structure and small lattice mismatch (4%) between Si and Ge allows a full miscibility of these two elements and thus it is possible to find Si and Ge within the same device (e.g.:SiGe alloys). These alloys show different optical properties as function of concentration of Ge in Si. In particular, it is possible to tune the optical band gap of the alloy by varying the Ge concentration in Si. This can be exploited for the optoelectronic and photovoltaic applications. **Figure A1.1b** shows the band structure obtained with the $\mathbf{k}\cdot\mathbf{p}$ method for relaxed crystalline Ge bulk. It can be noted that there is an indirect band-gap of 0.67 eV at the L valley and a direct band-gap at 0.8 eV at the Γ valley. ($k=0$).

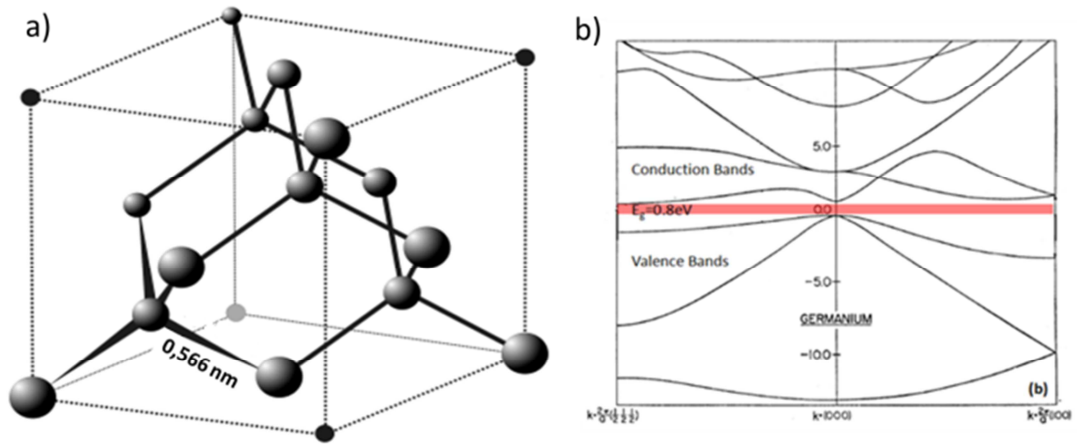


Figura A1.1: a) Primitive cell relative to the diamond lattice characteristic of Ge crystals. b) Representation of the band structure(E-K diagram) Ge calculated by the $k \cdot p$ method. [8].

Because of the presence of quasi-direct bandgap, Ge is able to absorb much more light with respect to Si. This feature is showed in **figure A1.2** where the absorption coefficient of crystalline and amorphous Ge, together with of c-Si are reported. In the c-Ge spectrum, two broad shoulder are visible at 2.2 eV and 4 eV which are associated to the direct E_1 and E_2 transitions occurring in bulk Ge. For what concerns the amorphous phase, the absorption spectrum show a featureless shape. The most important feature that we can observe in **figure A1.2** is that, up to 3 eV, the absorption coefficient both a-Ge and c-Ge are one order of intensity larger than c-Si. This evidence is due to the lower value and the quasi direct nature of Ge band gap with respect to Si. Therefore, combining the ability to absorb light in the NIR range with its high carrier mobility, Ge becomes a promising candidate for the development of IR photodetectors, optical modulators and multi-junction solar cells.

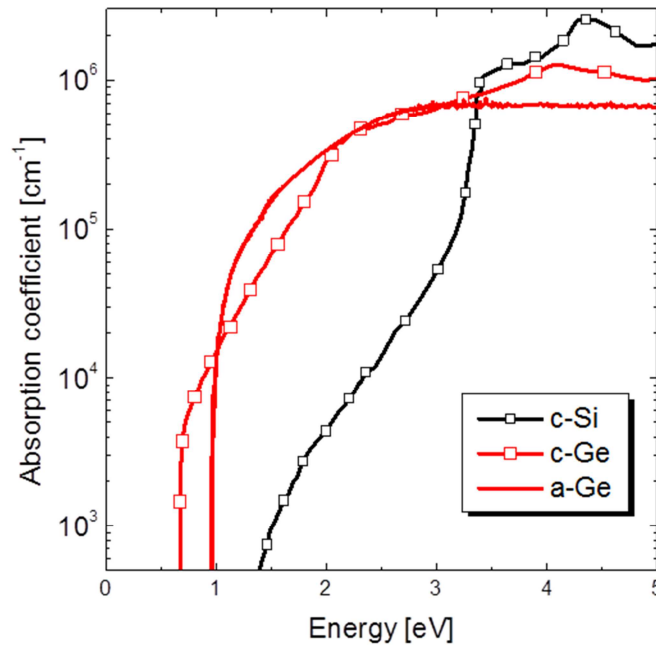


Figura A1.2: Absorption coefficient of crystalline Si and crystalline and amorphous Ge [95].

Unfortunately, in spite of important electrical and optical features found in Ge, the high cost of this latter has severely limited its use. As said before, the high cost of Ge is related to poor quantity in the Earth's surface. In this regard, the use of Ge NS could meet the scarcity issue of this element, allowing also to exploit the QCE occurring in confined systems. Moreover, Ge exhibits an exciton Bohr radius quite larger than that observed in Si (~4.5 nm in Si and 24 nm in Ge [30]-[103]. Thanks to this feature, it is possible to easily tune the absorption edge of Ge NS from NIR to UV range without shrinking too much the size of NS. This characteristic become interesting for the photovoltaic applications. As reported in **figure A1.3**, combining the tuning of bandgap occurring in nanostructured systems with the larger size

range for QCE observed in Ge, it should be possible to match better the solar spectrum with respect to the use of Si NS. In this way a larger part of solar spectrum can be absorbed, potentially increasing the efficiency of novel solar cells.

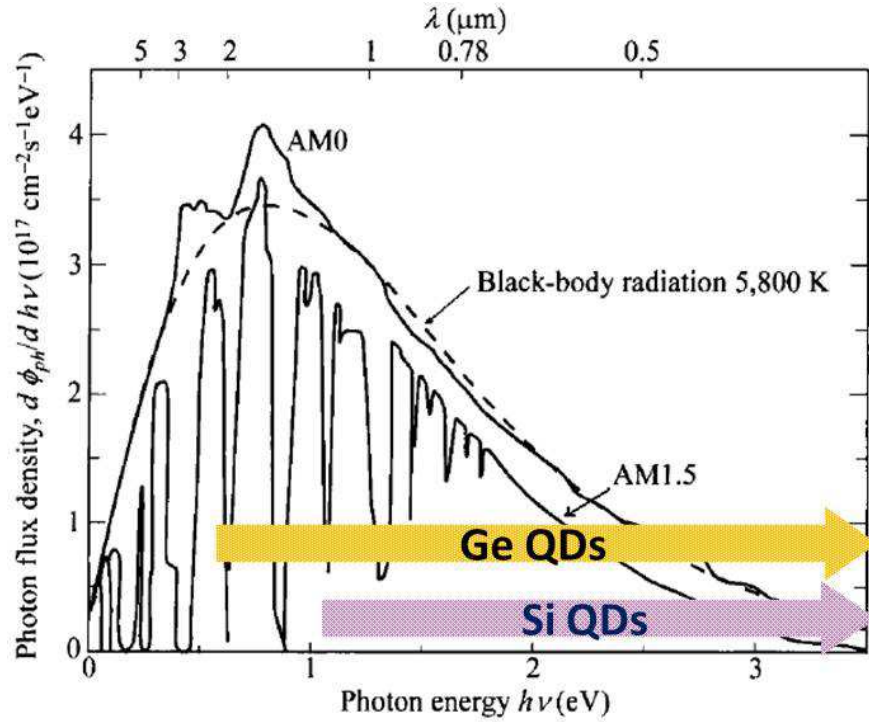


Figure A1.3: Solar spectrum in photon flux density per photon energy and absorption energy range for Si and Ge QDs generated by varying the size of QD Adapted [8].

This opportunity, together with the larger absorption capability and the quasi direct bandgap of Ge, makes Ge NS very attractive for several applications, especially for energy-tunable light. In order to boost the performance of these devices, a detailed investigation on the light absorption process in Ge NS is of essential importance. For this reason, the goal of this work is

focused on detailed examination of the optical properties occurring in Ge confined systems, spanning from Ge quantum well to Ge quantum dots. In this way, a deeper knowledge and control of the fundamental physical processes occurring in the confined systems, such as QCE and more, can be achieved.

Appendix 2

Double pass approximation: determination of α

For the determination of the absorption spectra from the transmittance and reflectance ones through the double pass method, we have to take into account that our samples are made of an SiGeO film deposited on a quartz substrate (**figure A2.1**). First of all, we can consider the situation in **fig.A2.1(a)**, where a radiation beam (I_0) hits a quartz substrate (thickness = d_Q).

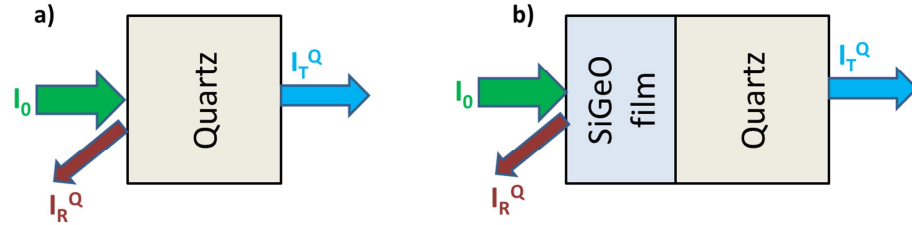


Figura A2.1: Schematic representation of transmitted (I_T^Q) and reflected (I_R^Q) beams from quartz substrate (a) and SiGeO film (b). I_0 represents the incoming beam, incident on sample

Let define R_{0Q} the reflectance at the interface air-quartz. The reflected beam intensity is $I_0 R_{0Q}$, while the remaining part which gets into the sample is $I_0(1 - R_{0Q})$. Consequently, after the crossover of the sample, at the interface quartz-air we have an intensity $I_0(1 - R_{0Q})e^{-\alpha_Q d_Q}$, where α_Q is the quartz absorption coefficient. At this second interface the beam is further transmitted and reflected. Therefore, the transmitted beam intensity is:

$$I_T^Q = I_0(1 - R_{0Q})e^{-\alpha_Q d_Q}(1 - R_{0Q}) \quad (\text{A2.1})$$

where the last term represents the fraction of light which is not reflected back by the interface quartz-air. Similarly we obtain the reflected beam intensity:

$$I_R^Q = I_0 R_{0Q} + I_0 (1 - R_{0Q}) e^{-\alpha_Q d_Q} R_{Q0} e^{-\alpha_Q d_Q} (1 - R_{Q0}) \quad (\text{A2.2})$$

where the first term represents the reflected beam intensity at the interface air-quartz, while the second term describes the reflected beam intensity at the interface quartz-air after being overcrossed two times the quartz. We neglect the multiple reflections.

Now we can consider the **fig. A2.1(b)**. Define d_F the film thickness. As we have done before, we can write transmitted and reflected beam intensity as:

$$I_T^F = I_0 (1 - R_{0F}) e^{-\alpha_F d_F} (1 - R_{FQ}) e^{-\alpha_Q d_Q} (1 - R_{Q0}) \quad (\text{A2.3})$$

and

$$\begin{aligned} I_R^F = & I_0 R_{0F} + I_0 (1 - R_{0F}) e^{-\alpha_F d_F} R_{FQ} e^{-\alpha_F d_F} (1 - R_{F0}) + \\ & I_0 (1 - R_{0F}) e^{-\alpha_F d_F} (1 - R_{FQ}) e^{-2\alpha_Q d_Q} R_{Q0} (1 - R_{FQ}) e^{-\alpha_F d_F} (1 - \\ & R_{F0}) \cong I_0 R_{0F} \end{aligned} \quad (\text{A2.4})$$

where R_{FQ} is the reflectance at the interface film-quartz, α_F is the absorption coefficient of the SiGeO film. The approximation in eq is justified by the fact that the film is absorbing, therefore the term $e^{-2\alpha_F d_F}$, which is present in the second and in the third term of eq., is very little.

Now, considering (A2.1) and (A2.3), the transmitted radiation intensity of the sample is:

$$I_T^F = (1 - R_{0F}) e^{-\alpha_F d_F} I_T^Q \frac{(1 - R_{FQ})}{(1 - R_{0Q})} \cong I_T^Q e^{-\alpha_F d_F} (1 - R_{0F}) \quad (\text{A2.5})$$

Where we have used the approximation $(1 - R_{FQ}) = (1 - R_{0Q})$ committing a maximum error of 3%. In fact, considering the expression $R_{FQ} =$

$\frac{(n_{SiGeO}-n_Q)^2}{2}$ and $R_{0Q} = \frac{(n_Q-n_0)^2}{(n_Q+n_0)^2}$, where n is the refractive index, and taking

$$(n_{SiGeO}+n_Q)$$

into account that $1.45 \leq n_Q \leq 1.65$ while $n_{SiGeO} \sim 2.30$, we obtained that

$$\frac{(1-R_{FQ})}{(1-R_{0Q})} \approx 1 \pm 0.03.$$

From (A2.5) and (A2.4) we obtain:

$$\alpha_F = \frac{1}{d_F} \ln \left(\frac{I_T^Q (1-R_{0F})}{I_T^F} \right) \quad (A2.5)$$

Therefore, from measurements of quartz and sample transmittances ($T_Q = I_T^Q/I_0$ and $T_F = I_T^F/I_0$) and of sample reflectance ($R_{0F} = I_R^F/I_0$), it is possible to determine the absorption coefficient as a function of energy through the relationship (A2.5).

References

1. 2015 Key world energy statistics - International Energy Agency, available at www.iea.org/statistics/.
2. V. Balzani and N. Armaroli, “*Energy for a Sustainable World: From the Oil Age to a Sun-Powered Future*”, John Wiley & Sons (2010).
3. BP Statistical Review of World Energy, June 2016, available at www.bp.com .
4. D. S. Ginley, D. Cahen, “*Fundamentals of Materials for Energy and Environmental Sustainability*”, Cambridge University press (2012).
5. R. Perez, K. Zweibel, T. E..Hoff, *Energy Policy* **39**, 7290 (2011).
6. https://commons.wikimedia.org/wiki/File:Global_energy_potential_and_consumption.svg .
7. www.fondriest.com/environmental/measurements/parameters/weather/photosynthetically-active-radiation/.
8. <http://large.stanford.edu/courses/2010/ph240/weisse2/>
9. Simon M. Sze (1981) “*Physics of semiconductor devices*”, 2nd Ed., (John Wiley & Sons, New York, NY).
10. W. Shockley and H. J. Queisser, *J. Appl. Phys.* **32**, 510 (1961).
11. Figure available at National Renewable Energy Laboratory website: <http://www.nrel.gov/ncpv/> .
12. N. M. Jeon, J. H. Noh, W. S. Yang, Y. C. Kim, S. Ryu, J. Seo and S. II Seokl, *Nature*, **517**, 476 (2015).

13. H. J. Snaith, *J. Chem. Lett.* **4**, 3623 (2013).
14. C. H. Henry, *J. Appl. Phys.* **51**, 4490 (1908).
15. F. Dimroth, M. Grave, P. Beutel, U. Fiedeler, C. Karcher, T. N. D. Tibbits, E. Oliva, G. Siefer, M. Schachtner, A. Wekkeli, A. W. Bett, R. Krause, M. Piccin, N. Blanc, C. Drazek, E. Guiot, B. Ghyselen, T. Salvetat, A. Tauzin, T. Signamarcheix, A. Dobrich, T. Hannappel, K. Schwarzburg, *Progress in Photovoltaics* **22**, 277 (2014).
16. A. Luque, A. Martí, N. López, E. Antolín, E. Cánovas, C. Stanley, C. Farmer, L. J. Caballero, L. Cuadra and J. L. Balenzategui, *Appl. Phys. Lett.* **87**, 083505 (2005).
17. A. Luque, A. Marti and C. Stanley, *Nature Photonics* **6**, 146 (2012).
18. A. J. Nozik and J. Miller, *Chem. Rev.* **110**, 6443 (2010).
19. M. C. Beard, K. P. Knutsen, P. Yu, J. M. Luther, Q. Song, W. K. Metzger, R. J. Ellingson, and A. J. Nozik, *Nano Lett.* **7(8)**, 2506 (2007).
20. R. D. Schaller, M. Sykora, J. M. Pietryga, and V. I. Klimov, *Nano Lett.*, **6 (3)**, 424 (2006).
21. Xudong Wang, C. J. Summers, and Z. L. Wang, *Nano Lett.* **4 (3)**, 423 (2004).
22. M. Sarikaya, C. Tamerler, A. K. -Y. Jen, K. Schulten and F. Baney, *Nature Materials* **2**, 577 (2003).
23. C. Sanchez, B. Julián, P. Belleville and M. Popall, *J. Mat. Chem.* **15**, 3559 (2005).
24. M. C. McAlpine, H. Ahmad, D. Wang and J. R. Heath, *Nature Materials* **6**, 379 (2007).
25. A. McCluskey, C. I. Holdsworth and M. C. Bowyer, *Org. Biomol. Chem.*, **5**, 3233 (2007).

26. S. M. Moghimi, C. Hunter, and J. C. Murray, *FASEB Journal* **19**, 311 (2005).
27. L. Zhang , F. X. Gu, J. M. Chan, A. Z. Wang, R.S. Langer, O. C. Farokhzad, *Clin. Pharmacol Ther.* **83** (5), 761 (2007).
28. P. V. Kamat, *J. Phys. Chem. C* **112** (48), 18737 (2008).
29. T. Takagahara and K. Takeda, *Phys. Rev. B* **46**, 15578 (1992).
30. H. Zhao and S. Mazumdar, *Phys. Rev. Lett.* **93**, 157402 (2004).
31. Y. M. Niquet, G. Allan, C. Delerue, M. Lannoo, *Appl. Phys. Lett.* **77**, 1182 (2000).
32. E. G. Barbagiovanni, D.J. Lockwood, P.J. Simpson, L.V. Goncharova, *J. Appl. Phys.* **111**, 034307 (2012).
33. G. Conibeer, M. Green, E. Cho, D. Konig, Y. Cho, T. Fangsuwannarak, G. Scardera, E. Pink, Y. Huang, T. Puzzer, S. Huang, D. Song, C. Flynn, S. Park, X. Hao, and D. Mansfield, *Thin Solid Films* **516**, 6748 (2008).
34. S. Mirabella, S. Cosentino, A. Gentile, G. Nicotra, N. Piluso, L. V. Mercaldo, F. Simone, C. Spinella, and A. Terrasi, *Appl. Phys. Lett.* **101**, 011911 (2012).
35. S. Cosentino, E. Sungur Ozen, R. Raciti, A. M. Mio, G. Nicotra, F. Simone, R. Turan, A. Terrasi, A. Aydinli, S. Mirabella, *J. Appl. Phys.* **115**, 043103 (2014).
36. M. A. Green, *Physica E*, **14**, 11 (2002).
37. Man-Fai Ng and R.Q. Zhang, *J. Phys. Chem. B* **110**, 21528 (2006).

38. S. Mirabella, R. Agosta, G. Franzò, I. Crupi, M. Miritello, R. Lo Savio, M. A. Di Stefano, S. Di Marco, F. Simone, and A. Terrasi, *J. Appl. Phys.* **106**, 103505 (2009).
39. R. Guerra, M. Marsili, O. Pulci, S. Ossicini, *Phys. Rev. B* **84**, 075342 (2011).
40. P. B. Sorokin P. V. Avramov, L. A. Chernozatonskii, D. G. Fedorov and S. G. Ovchinnikov, *J. Phys. Chem. A* **112**, 9955 (2008).
41. G. Franzò, M. Miritello, S. Boninelli, R. Lo Salvio, M. G. Grimaldi, F. Priolo, F. Iacona, C. Spinella, and S. Coffa, *J. Appl. Phys.* **104**, 094306 (2008).
42. M. Zacharias, P. M. Fauchet, *Appl. Phys. Lett.* **71**, 380 (1997).
43. D. Mariotti, S. Mitra and V. Svrcek, *Nanoscale* **5**, 1385 (2013).
44. R. Ghosh, P. K. Giri, K. Imakita and Minoru Fuji, *Nanotechnology* **25**, 045703 (2014).
45. E. G. Barbagiovanni, David J. Lockwood, Peter J. Simpson, and Lyudmila V. Goncharova, *Appl. Phys. Rev.* **1**, 011302 (2014).
46. E. G. Barbagiovanni, R.N.Costa Filho, *Physica E* **63**, 14–20 (2014)
47. S. Cosentino, A. M. Mio, E. G. Barbagiovanni, R. Raciti, R. Bahariqushchi, M. Miritello, G. Nicotra, A. Aydinli, C. Spinella, A. Terrasi and S. Mirabella, *Nanoscale* **7**, 11401 (2015).
48. E. G. Barbagiovanni, S. Cosentino, A. Terrasi, S. Mirabella, D.J. Lockwood and R. N. Costa Filho, *J. Appl. Phys.* 2015, **117**, 154304

49. F. Bassani, and G. Pastori Parravicini (1975) “*Electronic States and Optical Transitions in Solids*”, Ed. R.A. Ballinger, (Pergamon Press, Oxford).
50. B. Sapoval and C. Hermann (1988) “*Physics of semiconductors*”, Ed by Ellipses, Paris, (Springer)
51. J. Bardeen, F. J. Blatt, and L. H. Hall, *Photoconductivity Conference, Atlantic City (November, 1954)*, New York (1956).
52. J. Tauc, “*Amorphous and liquid semiconductors*”, Ed. J. Tauc.
53. J. Tauc, T. Grigorovivi and A. Vancu, *Phys. Stat. Sol.* **15**, 627 (1966).
54. S. Knief, W. von Niessen, *Phys. Rev. B.* **59**, 12940-12946 (1999).
55. G. D. Cody, B. G. Brooks and B. Abeles, *Solar Energy Materials* **8**, 231 (1982).
56. Y.H. Kuo and Y.S. Li, *Phys. Rev. B* **79**, 245328 (2009).
57. M. Logar, S. Xu, S. Acharya and F. B. Prinz; *Nano Lett.* **15**, 1855 (2015).
58. B. G. Lee, J. W. Luo, N. R. Neale, M. C. Beard, D. M. Zacharias, P. Stradins, and A. Zunger, *Nano Lett.* **16 (3)**, 1583 (2016).
59. I. Vasiliev, j. R. Chelikowsky and R. M. Martin, *Phys. Rev. B* **65**, 121302 (2002).
60. A. B. Talochkin, I. B. Chistokhin and V. I. Mashanov, *Jour. Appl. Phys.* 119, 134302 (2016).
61. B. Rafferty and L. M. Brown, *Phys. Rev. B* **58**, 10326 (1998).
62. H. J. Jung, N. P. Dasgupta, P. B. Van Stockum; A. L. Koh; R. Sinclair; F. B. Prinz, *Nano Lett.* 13, 716 (2013).

63. S. Cosentino, M. Miritello, I. Crupi, G. Nicotra, F. Simone, C. Spinella, A. Terrasi and S. Mirabella, *Nanoscale Res. Lett.* **8**, 128 (2013).
64. P. Liu, P. Longo, A. Zaslavsky and D. Pacifici, *Journ. Appl. Phys.* **119**, 014304 (2016).
65. P. Hapala, K. Kusova, I. Pelant, and Pavel Jelinek, *Phys. Rev. B* **87**, 195420 (2013).
66. M. Mayer: *SIMNRA user's guide, report IPP 9/113 Garching*: Max Planck Institut für Plasmaphysik;1997
67. A. R. Fohouri and I. Bloomer, *Phys. Rev. B* **34**, 7018 (1986).
68. D. V. Likhachev, N. Malkova, L. Poslavsky, *Thin Solid Film* **589**, 844 (2015).
69. Y. F. Chen, C. M. Kwei, C. J. Tung, *Phys Rev. B* **48**, 4373 (1993).
70. D. Poelman and P. F. Smet, *J. Phys D: Appl. Phys* **36**, 1850 (2003).
71. Y. Liu, J. H. Hsieh, S. K. Tung, *Thin solid films* **510**, 32 (2006).
72. G. E. Jellison Jr. and F.A. Modine, *Appl. Phys. Lett.* **69**, 371 (1996).
73. G. E. Jellison Jr. and F.A. Modine, Erratum *Appl. Phys. Lett.* **69**, 371 (1996).
G. E. Jellison Jr. and F.A. Modine, "Erratum", *Appl. Phys. Lett.* **69**, 2137 (1996).
74. E. Centurioni, *Appl. Opt.* **44**, 7532 (2005) (see also <http://www.bo.imm.cnr.it/users/centurioni/optical.html>).
75. A. Allegrezza, F. Gaspari, M. Canino, M. Bellettato, A. Desalvo, C. Summonte, *Thin solid films* **556**, 105 (2014).
A. Allegrezza, F. Gaspari, M. Canino, M. Bellettato, A. Desalvo, C. Summonte, "Erratum" *Thin solid films* **564**, 426 (2014).

76. , E. D. E. Palik *Handbook of Optical Constants of Solids.*, Academic Press, San Diego (1998)..
77. M. Palummo, G. Onida, R. Del Sole, *physica status solid (a)* **175**, 23 (1999).
78. T. M. Mok and S. K. O’Leary, *Jour. Appl. Phys.* **102**, 113525 (2007).
79. Röbbner, G. Isella, and H. von Känel, *Appl. Phys. Lett.* **82**, 754 (2003).
80. A. D. Yoffe, *Advances in Physics* **51**, 799 (2002).
81. L. A. Nesbit, *Appl. Phys. Lett.* **46**, 38 (1985).
82. J. J. Skov, T. P. Leervad Ledersen, R. Pereira, J. Chevallier, H. J. Lundsgaard, B. Bech Nielsen, L. A. Nylandsted., *Appl. Phys. A* **83**, 41 (2006).
83. H. G. Chew, W. K. Choi, Y. L. Foo, F. Zheng, W. K. Chim, Z. J. Voon, K. C. Seow, E. A. Fitzgerald, and D. M. Y. Lai, *Nanotechnology* **17**, 1964–1968 (2006).
84. A. La Magna, G. Nicotra, C. Bongiorno, C. Spinella, M. G. Grimaldi E. Rimini, L. Caristia and S. Coffa, *Appl. Phys. Lett*, **90**, 183101 (2007).
85. W. K. Choi, V. Ng, S. P. Ng, H. H. Thio, Z. X. Shen, and W. S. Li, *J. Appl. Phys.* **86**, 1398 (1999).
86. D. Bermejo and M. Cardona, *J. Non-Cryst. Solids*, **32**, 405 (1979).
87. S. Cosentino, S. Knebel, S. Mirabella, M. Miritello, S. Gibilisco, F. Simone, A. Terrasi, H. Bracht and G. Wilde, *Appl. Phys. A: Solid Surf.* **116**, 233 (2014).

88. P. Cuony, D. T. L. Alexander, I. Perez-Wurfl, M. Despeisse, G. Bugnon, M. Boccard, T. Soderstrom, A. Hessler-Wyser, C. Hebert and C. Ballif, *Adv. Mater.* **24**, 1182 (2012).
89. P. D. Nguyen D. M. Kepaptsoglou, R. Erni, Q. M. Ramasse, and A. Olsen, *Phys. Rev. B* **86**, 245316 (2012).
90. K. Sasaki, S. Tsukimoto, M. Konno, T. Kamino and H. Saka, *Journal of Microscopy* **203**, 12 (2001).
91. N. Jiang, Jianrong Qiu and J. C. H. Spence, *Appl. Phys. Lett.* **86**, 143112 (2005).
92. S Mirabella, S Cosentino, M Failla, M Miritello, G Nicotra, F Simone, C Spinella, G Franzò, A Terrasi, *Appl. Phys. Lett.* **102** (19), 193105 (2013).
93. C. Uhrenfeldt, J. Chevallier, A. N. Larsen, and B. B. Nielsen, *J. Appl. Phys.*, **109** 094314 (2011).
94. M. Kobayashi, G. Thareja, M. Ishibashi, Y. Sun, P. Griffin, J. McVittie, P. Pianetta, K. Saraswat, and Y. Nishi, *J. Appl. Phys.* **106**, 104117 (2009).
95. Peter Y. Yu and Manuel Cardona, “*Fundamentals of Semiconductors*”, 4th Ed. Springer.
96. W. T. Masselink, P. J. Pearah, J. Klem, C. K. Peng, H. Morkoc, G. D. Sanders and Y. Chang, *Phys. Rev. B* **32**, 8027 (1985).
97. G. W. Bryant, *Phys. Rev B* **37**, 8763 (1988).
98. R. Guerra and S. Ossicini, *Phys. Rev. B* **87**, 165441 (2013).

- 99. R. Guerra, I. Marri, R. Magri, L. Martin-Samos, O. Pulci, E. Degoli and S. Ossicini, *Phys. Rev. B* **79**, 155320 (2009).
- 100. K. Kusova, L. Ondic, E. Klimesova, K. Herynkova, I. Pelant, S. Danis, J. Valenta, M. Gallart, M. Ziegler, B. Honerlage and P. Gilliot, *Appl. Phys. Lett.* **101**, 143101 (2012).
- 101. Zacharias, M.; Heitmann, J.; Scholz, R.; Kahler, U.; Schmidt, M & Bläsing, J. *Appl. Phys. Lett.*, **80**, 661 (2002).
- 102. J. Bardeen and W. H. Brattain, *Phys. Rev.* **75**, 1208 (1949).
- 103. A. G. Cullis, L. T. Canham and P. D. J. Calcott, *J. Appl. Phys.* **82** 909 (1997).

Curriculum vitae

Rosario Raciti was born in Catania, Italy, in February 2nd, 1989

1 Education

- Working, since February 2017 at the Department of Physics and Astronomy of University of Catania with a research contract.
- Physics Ph.D Student at the University of Catania and CNR-IMM, from January 2014 to October 2016.
- Master Degree in Physics, obtained on April 27th, 2013 with full marks (110/110 cum laude) with a dissertation entitled “**FOTOASSORBIMENTO IN NANOSTRUTTURE DI Ge: EFFETTO DELLA MATRICE IN OSSIDO E NITRURO DI SILICIO**”(tutor: Prof. Antonio Terrasi, supervisor: Prof. Salvo Mirabella).
- Bachelor Degree in Physics obtained on 29th, 2011 with full marks (110/110) with a dissertation entitled “**NANOGUSCI METALLICI: SINTESI, PROPRIETA' ED APPLICAZIONI**”(supervisor: Prof. Francesco Priolo).

2 Collaboration

- Dipartimento di Fisica e Astronomia, University of Catania.
- CNR-IMM, Catania, Italy.
- CNR-IMM Bologna, Italy.
- Department of Physics, Bilkent University, Ankara, Turkey.
- Department of Physics, Middle East Technical University, Ankara, Turkey

3 Conferences, international schools, workshops participation

Materials 2016, Acicastello (Italia), 12 -16 December 2016 – 1 poster presentation entitled “*Enhanced light absorption in Ge quantum dot multilayers*”.

-Nanosea 2016, Giardini Naxos (Italia), 3 – 8 July 2016- 1 oral presentation entitled “*Enhanced light absorption in Ge quantum dot multilayers*”.

-FisMat, Palermo (Italia), 28 September 2015 al 02 October 2015 – 1 oral presentation entitled “*Multilayered Ge quantum dots embedded in SiO₂: structural and optical analysis*”.

-E-MRS Spring Meeting 2015, Lille (Francia), 11 - 15 May 2015 1 poster presentation entitled “*Multilayered Ge quantum dots embedded in SiO₂: structural and optical analysis*”.

-IEEE Nanotechnology Materials and Devices Conference, Acicastello (Italia), 12 - 15 October 2014 – 1 oral presentation entitled “*Ge quantum dots in SiO₂ or Si₃N₄ matrix for efficient light absorption*”.

-International summer school of Materials For Renewable Energy 2014, Ettore Majorana Foundation And Centre For Scientific Culture, Erice (IT), 11 - 19 July 2014 –1 poster presentation entitled “*Ge quantum dots in SiO₂ or Si₃N₄ matrix for efficient light absorption*”.

-II edition of workshop Carbomat 2011 “**Carbon-based low-dimensional Materials**”, Museo Diocesano Catania, 5-7 December 2011.

List of Publications

- Salvatore Cosentino, Emel Sungur Ozen, **Rosario Raciti**, Antonio M. Mio, Giuseppe Nicotra, Francesca Simone, Rasit Turan, Antonio Terrasi, Atilla Aydinli, Salvo Mirabella, “*Light harvesting with Ge quantum dots embedded in SiO₂ or Si₃N₄*” , Jour.Appl. Phys., **115**, 043103 (2014).
- Salvatore Cosentino, Antonio M. Mio, Eric G. Barbagiovanni, **Rosario Raciti**, R. Bahariqushchi, Maria Miritello, Giuseppe Nicotra, Atilla Aydinli, Corrado Spinella, Antonio Terrasi and Salvatore Mirabella, *Nanoscale* **7**, 11401 (2015).
- Salvatore Cosentino, Giacomo Torrisi, **Rosario Raciti**, Massimo Zimbone, Isodiana Crupi, Salvatore Mirabella, Antonio Terrasi, *RSC Advances* **6** (44), 38454 (2016).

Ringraziamenti

Non è mai facile riuscire a ringraziare, in poche righe tutte le persone che nel corso di questi tre anni hanno contribuito, chi con una collaborazione, chi con un supporto morale o materiale e chi con consigli e parole di incoraggiamento, alla nascita e allo sviluppo di questa tesi di dottorato.

I primi ringraziamenti vanno certamente al prof. Antonio Terrasi per la fiducia e la pazienza (molta fidatevi!!!) mostrata durante tutti i tre anni. Al di là delle professionalità dimostrata, gli sono grato per la grande umanità mostratami in ogni momento e per la capacità di ascoltare e di aiutarmi sempre con il solito entusiasmo che lo contraddistingue.

Un grandissimo ringraziamento va al Prof. Salvo Mirabella, mio supervisore in questa tesi, per avermi sempre spronato ad andare sempre più a fondo nella comprensione fisica di quello che studiavo.

Ringrazio il dott. Salvo Cosentino che è stato fondamentale per la mia crescita con i suoi continui consigli e la sua enorme disponibilità durante l'intero periodo di dottorato.

In questi anni ho avuto l'opportunità di lavorare in un ambiente stimolante. In questo contesto, ho avuto l'opportunità di lavorare con diverse persone che mi hanno lasciato qualcosa di importante. Per tale motivo desidero ringraziare il dott. Vittorio Privitera, il prof. Francesco Priolo e la prof.ssa Maria Grazia Grimaldi per avermi dato l'opportunità di lavorare all'interno di questo splendido gruppo. Ringrazio inoltre tutte quelle persone che mi hanno accompagnato durante il mio percorso di dottorato: Dr. Isodiana Crupi, Dr. Giuliana Impellizzeri, Dr. Giorgia Franzò, Dr. Elena Bruno, Dr. Maria Miritello, Dr. Sabrina Carroccio e Dr. Simona Boninelli sempre pronti a dispensare consigli. Ringrazio infine tutti i tecnici (Giuseppe Pantè, Salvo Tati e Carmelo Percolla) e gli amministrativi (Alessandra La Greca, Primo

Furno e Patrizia Pappalardo) per il loro supporto e la professionalità dimostratami.

Ringrazio Giovanna , Massimo e Maria Antonietta che in questi tre anni hanno dispensato consigli e condiviso con me la propria conoscenza scientifica.

Un ringraziamento speciale va ai compagni di stanza che si sono alternati in questi 3 anni (Giacomo, Vale, Alessandro, Maria Censabella, Antonella, Stefano, Paolo e Salvo Cosentino) con cui ho condiviso tanti momenti di serenità e divertimento. Non dimenticherò mai i momenti goliardici e le discussioni durante le pause caffè e “sigaretta”. Vi voglio bene ragazzi!!!!

Ringrazio tutti i ragazzi della “stanza dottorandi” e del “lab sputter” (Maria Cantarella, VickyJ, Enrica, Martina, Adriana, Mario e Peppe Cacciato) con cui non ho solo condiviso numerose pause pranzo ma anche dei bei momenti di serenità. Non dimenticherò mai il supporto che mi avete dimostrato nei periodi più pesanti.

Un ringraziamento va al gruppo a tutti i colleghi “pagghiazzi” (Davide, Salvo, Walter, Guido e Ciccio). Nonostante la distanza sono riusciti sempre a rendere meno pesante e stressante questo percorso grazie al nostro immenso gruppo Whatsapp.

Un ringraziamento speciale va a tutti i miei amici specialmente ai “roccalumerini” (Daniele, Miky, Giulia, Enrico, Claudia, Salvo, Santi, Kevin; Andrea, Luigi, Gianluca, Gianluca T ecc..) ed ad Angelo con cui ho trascorso tanti momenti di allegria e spensieratezza.

Ringrazio inoltre Maria Josè, Maria Cantarella e Marta con cui ho condiviso dal primo all’ultimo giorno questi tre bellissimi anni. (Ci siamo riusciti ragazzi!!!!)

Ringrazio mia zia Eva che mi ha sempre trattato come un figlio e supportato durante tutto il mio percorso di vita.

Un affettuoso ringraziamento va alle persone più importanti della mia vita mio padre e mia madre che mi hanno sostenuto con enormi sacrifici e rinunce. Non ci sono parole per descrivere quello che loro fanno per me, perché quello che sono lo devo soprattutto alla loro educazione e

alla presenza costante nella quotidianità.

Un immenso ringraziamento va inoltre al mio fratellone e secondo padre Ciccio sempre pronto ad aiutarmi e supportarmi (anche a distanza) in qualsiasi circostanza e difficoltà. Un grosso pezzo dei miei traguardi personali è certamente merito suo.

Infine, un ricordo e un ringraziamento va infine a mio zio Santo, alle mie due nonne Maria e mio nonno Saro che da lassù, son sicuro, mi hanno aiutato a raggiungere questo importante obiettivo.